Fault Geometry and Distributions in the Princess Elisabeth Zone, Belgian Continental Shelf

Report

Clay Tectonics Project, Deliverable 2.1

Harisma Andikagumi and Marc De Batist

Renard Centre of Marine Geology, Department of Geology, Ghent University
Ghent 9000, Belgium

Summary

This report investigates the geological conditions and subsurface fault structures of the Princess Elisabeth Zone (PEZ), an offshore site for the future wind farm development on the Belgian Continental Shelf. The study focuses on faulting within the Kortrijk clay formation, aiming to provide a detailed analysis of the spatial extent, distribution, and orientation of faults in the area, which are essential parameters for guiding site planning and reducing operational risks. Data were collected during ultra-high-resolution seismic surveys conducted from November 2022 to May 2024. Four focused study areas (Blocks A, B, C, and D) were analysed by means of parametric sub-bottom profiler and Sparker seismic datasets. These methods enabled detailed mapping of fault geometry, spacing, and distributions.

The study identified two distinct fault groups in the PEZ. The first group, oriented ENE–WSW, is prominent in Block A and the southern part of Block D. These faults are characterized by short lengths (median ~100 m), steep dips (~64°), and fault spacing ranging from 50 to 100 m. The second group, oriented NNE–SSW, dominates Blocks B, C, and the northern part of Block D. These faults are longer (median lengths of 200–500+ m), have moderate dips (~40–55°), and penetrate deeper layers, sometimes reaching the top of Cretaceous. Fault spacing for this group is significantly broader, typically between 200 and 300 m. An abrupt transition between these two fault groups is evident in Block D, reflecting a clear partitioning of the structural styles across the study area.

The findings carry important implications for wind farm development and fault origin. Predictable fault orientations, compared to a more variable fault orientations expected in polygonal fault system, reduce geological uncertainties. The study also reveals key deviations from typical polygonal fault systems, suggesting regional tectonic influences on fault formation. Further investigations are recommended to fully understand the processes that control the faulting origin. By providing a detailed assessment of fault geometry and distributions, this report offers critical insights for minimising risks and optimising design of the offshore wind farms in the PEZ, providing framework for safer and more efficient offshore wind farm development.

Keywords: *fault distributions, fault modelling, clay formation, seismic reflection, offshore wind farm, Princess Elisabeth Zone (PEZ)*

Contents

1 Introduction

Geological investigation plays a key role, not only in the planning and development stage of a wind farm complex, but also during operation and decommissioning[1] (**Figure 1.1A**). Effective offshore wind farm development requires a thorough understanding of the geological conditions of the subsurface, as these directly impact the safety, stability, and economic feasibility of the wind farm. During the planning phase, geological investigations inform site selection, ensuring that turbines are placed in areas with suitable condition and minimal geological hazards[2]. Throughout the operation phase, ongoing geological monitoring helps managing risks like sediment mobility, scour, and structural stability[3-5]. At the decommissioning stage, understanding the site's geological conditions is important for safely dismantling structures and restoring the environment[6]. Thus, geological knowledge underpins the entire lifecycle of wind farms.

Various geological and geophysical data are used to build a model to describe the subsurface conditions of the prospective sites[1] (**Figure 1.1B**). The development of accurate subsurface models relies on integrating diverse datasets, including seismic data and sediment samples. These models provide insights into the stratigraphy, sediment composition, and structural features in the subsurface, providing specific design solutions for wind turbine foundations. For instance, seismic reflection profiles can reveal the presence of faults or other geological structures[7,8], while cone penetration tests (CPTs) offer detailed geotechnical data to assess material strength[9]. By combining these data sources, developers can create robust ground models that optimise turbine placement, reduce construction risks, and ensure long-term operational stability.

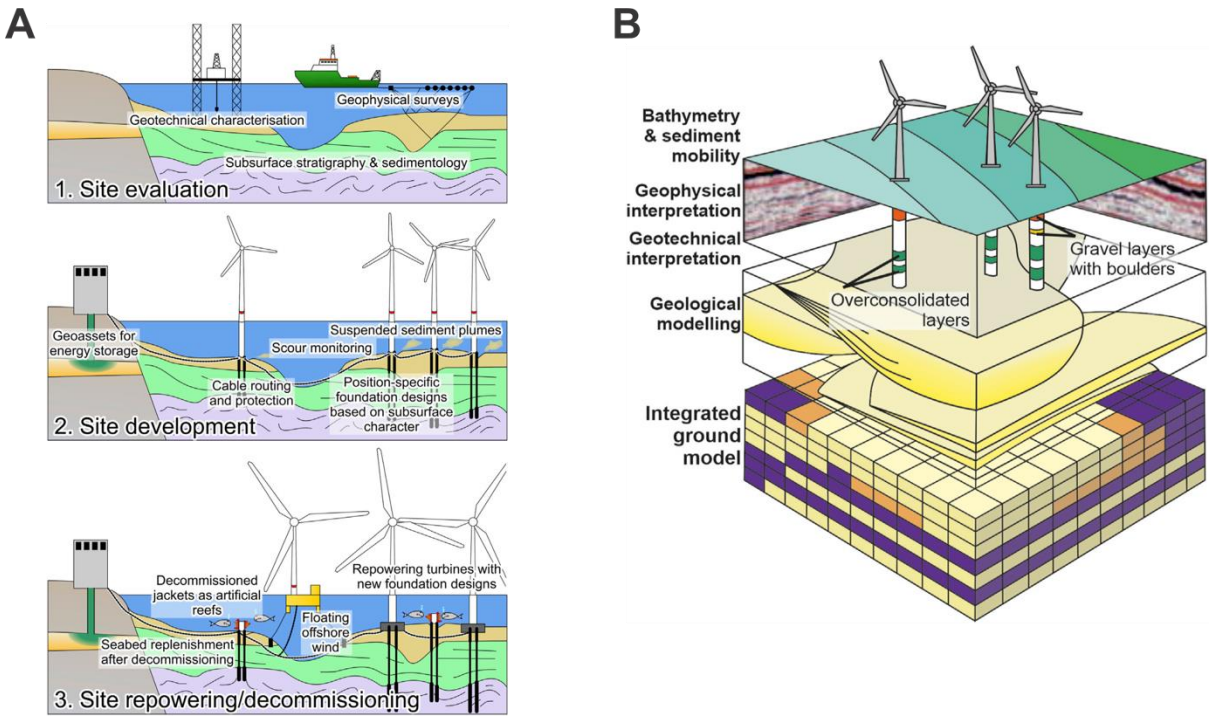

Figure 1.1. The roles of geological investigation in wind farm development[1]; (A) Contributions of geology in various stages of development: site evaluation, development, and decommissioning; (B) Various geological and geophysical dataset to construct integrated ground model for wind mill placement.

This report aims to describe the distribution and structural style of the deformations in the Kortrijk clay formation in the Princess Elisabeth Zone (PEZ), offshore Belgium, especially the fault distributions and their characteristics. This report expects to provide a comprehensive analysis of the spatial extent, distribution, and orientation of faults within the area, which are critical to guide site planning and minimise operational hazards.

1.1 Geology of the Princess Elisabeth Zone

The PEZ is mainly underlain by the Eocene-aged Kortrijk clay formation and, in the northern part, the Tielt and Gentbrugge formations (**Figure 1.2**), covered with Quaternary sand deposits[10,11]. The Kortrijk Formation, reaching substantial thickness of 150–180 m, consists predominantly of very high to extremely high-strength marine clays, interspersed with laminations and beds of silt and sand. It also contains localised features such as claystone nodules and bioturbated textures, reflecting its deposition in a deep offshore mudshelf environment[10,12]. The Kortrijk formation is a lateral equivalent of the London clay, outcropping in southwest England and also found in parts of the British sector of the North Sea[11,13,14].

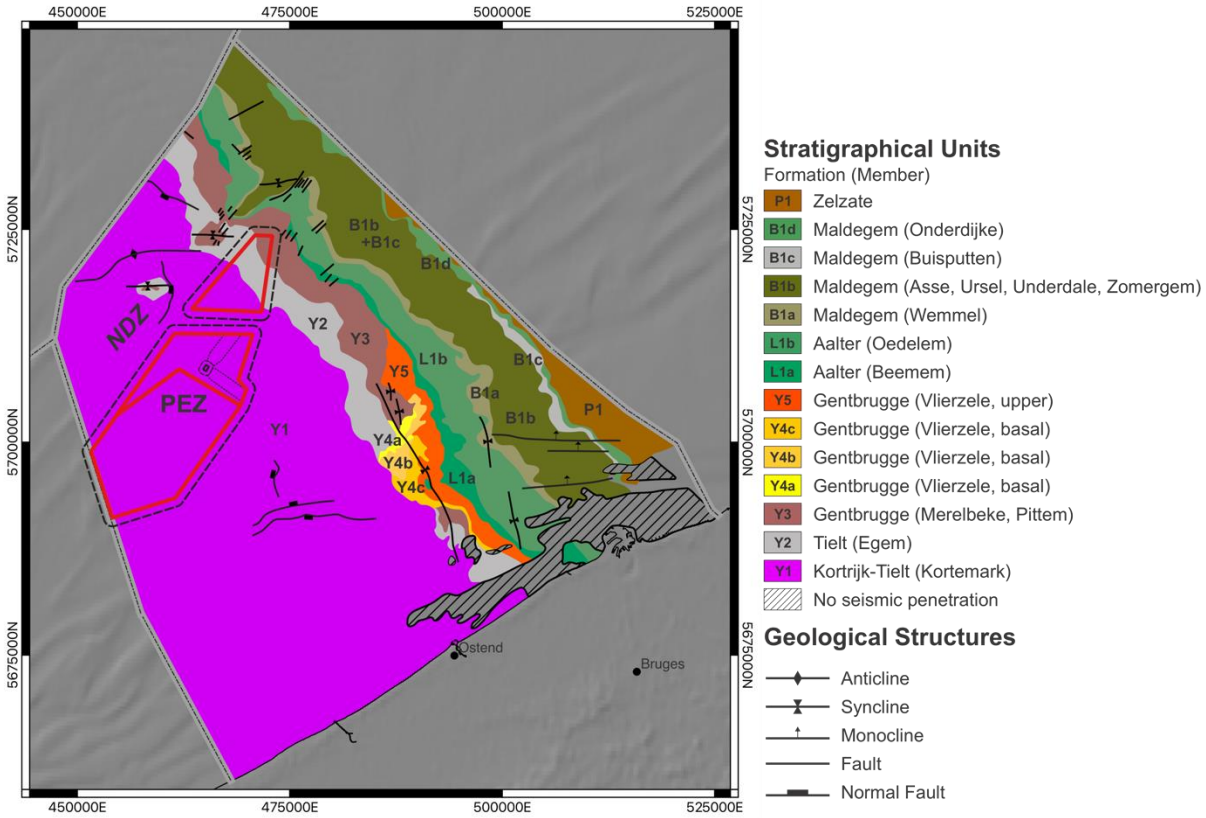

Figure 1.2. Geological Map of the Belgian Continental Shelf[10] with reference to the location Princess Elisabeth Zone (PEZ). The PEZ, indicated by red polygons, is mostly underlain by the Kortrijk clay formation (Y1) and, in the northern part, by the sand-dominated Tielt and Gentbrugge formations (Y2 and Y3).

The Tielt Formation represents an environment influenced by advancing deltaic systems, characterised by bioturbated silty clays with occasional thick sand laminations with thickness reaching 30–45 m[10]. Further north, the Gentbrugge Formation, exhibiting thicknesses of 40–60 m, comprising high-strength marine clays with frequent sand-filled burrows, indicating a more dynamic depositional environment within a shallow marine setting[10].

The PEZ is located immediately to the south of the Noordhinder Deformation Zone (NDZ) (**Figure 1.2**). This deformation zone is primarily basement-induced, a result of regional tectonic stresses that occurred during the late Eocene, leading to the development of major structural features[10,15]. These structures include normal faults and folds (synclinal and anticlinal) where fold axes arranged in an *en-echelon* pattern.

1.2 Clay Tectonics and Polygonal Fault Systems

Layer-bound faulting in a clay formation has been associated with clay tectonics and polygonal fault systems, which are widely observed in fine-grained sedimentary basins[16]. Advancement in 3D seismic surveys has allowed us to observe more polygonal faults around the world. These systems are especially prevalent in continental margin settings, including those near the Nankai Trough in Japan and the Vøring Basin off the coast of Norway. In the Nankai Trough, polygonal fault systems have been identified within Miocene-Pliocene claystones interbedded with volcanic ash layers[17]. Similarly, in the Vøring Basin, the diagenesis of biosiliceous sediments, was found to coincide with the formation of polygonal fault systems[18,19].

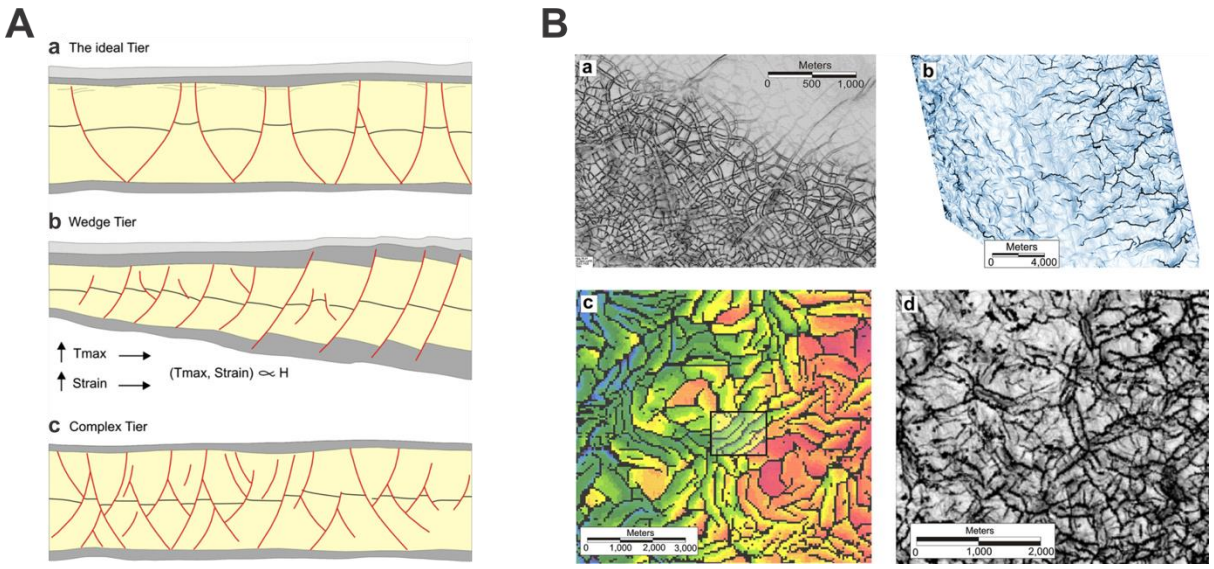

Figure 1.3. Polygonal fault system (PFS) as a typical feature of clay tectonics[16]; (A) Schematic diagram of the development of the intra-formational faulting; (B) Various examples of PFS in map view showing fault system with no preferred fault orientation.

Polygonal fault systems are characterised by intraformational faults without predominant orientation (**Figure 1.3**), forming complex polygonal geometries when viewed in planform[16]. These faults are layer-bound and typically confined to stratigraphic intervals dominated by fine-grained sediments such as claystones, chalks, or biosiliceous mudstones. The genesis of polygonal fault systems is strongly linked to diagenetic processes, including mineral dissolution, clay transformation, and volumetric contraction. These processes alter the mechanical properties of the sediment, leading to shear failure under low confining stresses. Experimental studies have shown that diagenetically-induced contraction can trigger fault nucleation, propagating to form the extensive networks observed in seismic data[20,21].

Faulting in the Kortrijk formation has been assumed to be polygonal faults as observed in other clay formations. Earlier studies in the Belgian part of the North Sea identified intraformational faults in the Ypresian marine clays (i.e., Kortrijk formation) observed offshore using 2D seismic profiles[11,22]. These faults, found entirely within the clayey sequence, were

assumed to be part of a polygonal fault system. These offshore studies were further complemented by outcrop evidence of these features in Belgian clay pits[23]. The faults found at these quarries displayed arbitrary orientations, consistent with polygonal fault systems elsewhere. Therefore, our study in the PEZ seeks to evaluate whether the faulting in the Kortrijk Formation exhibits characteristics of a polygonal fault system and to understand its potential implications for the planning and development of the future wind farm.

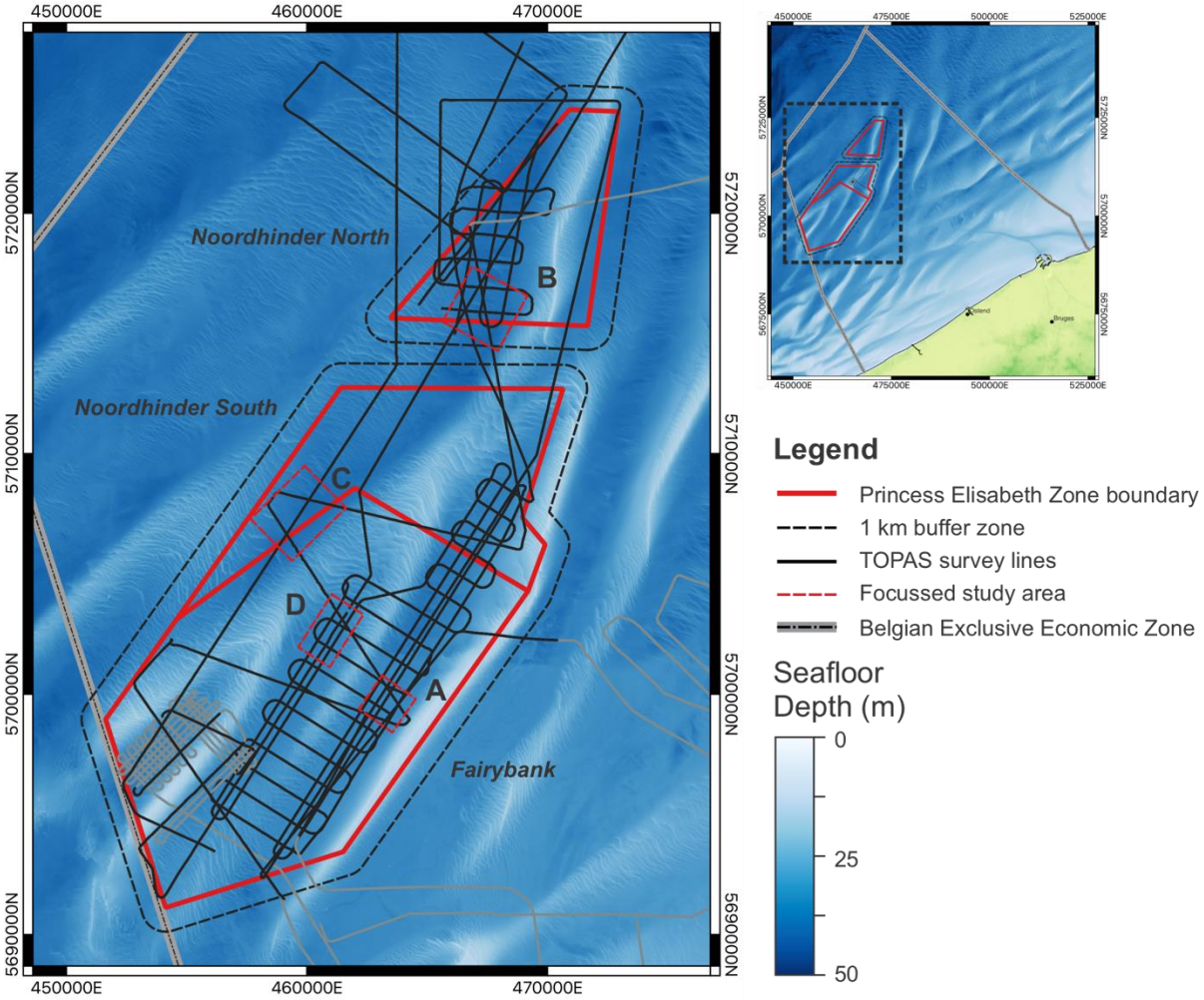

Figure 1.4. Dataset of parametric sub-bottom profiles acquired using the Topographic Parameteric Acoustic System (TOPAS) mounted on RV Belgica, from research campaigns conducted in November 2022 and November 2023. Location of detailed pseudo-3D survey is highlighted as Block A, B, C, and D[24].

2 Methods

2.1 Datasets

The datasets were collected during research cruises conducted between November 2022 and May 2024, utilising ultra-high-resolution seismic reflection systems deployed from RV Belgica and RV Simon Stevin. These included the TOPAS parametric sub-bottom profiler, the Innomar Quattro parametric sub-bottom profiler (PES), and sparker seismic systems. The TOPAS system was employed for larger scale surveys across the PEZ, providing broad coverage to observe variability in geological structures (**Figure 1.4**). The PES, operating at higher frequencies, was designed to achieve finer resolution, enabling detailed imaging of shallow subsurface

features such as sedimentary layers and near-surface structures. It was specifically utilised for dense grid surveys within our focused study areas. Meanwhile, the sparker seismic system was utilised for visualising deeper and larger geological structures, complementing the targeted investigations of the other methods.

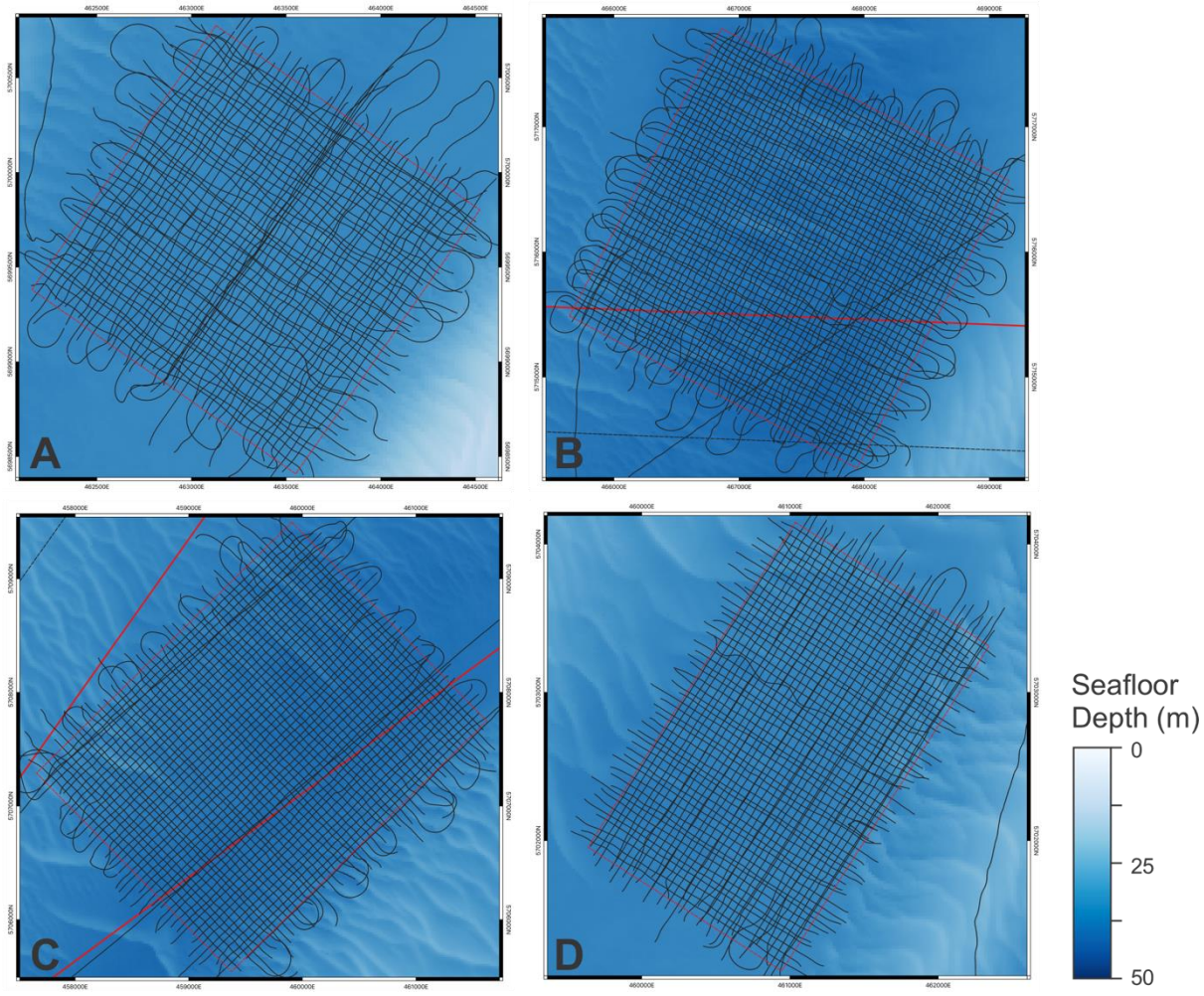

Figure 2.1. Dataset of dense grid pseudo-3D parametric sub-bottom profiler using Inomar Quatro system and Sparker profiling system in Block A, B, C, and D, from research cruise campaign on RV Simon Stevin in February 2023 and May 2024.

The PEZ consists of three main areas: Fairybank in the south, Noordhinder South in the centre, and Noordhinder North in the north. There are three main focused study blocks within these areas: Block A, B, and C, with an additional Block D added based on results from ongoing geological interpretations (**Figure 2.1**). These locations were strategically selected taking into account the constraints imposed by the sandbanks, requiring the Quaternary sand layer to be as thin as possible to effectively image the underlying Kortrijk Formation[25]. Block A, covering an area of 1.6 x 1.6 km near the southeast boundary of the PEZ in the Fairybank, is expected to have the thinnest Quaternary sand layer, making it the most favourable for imaging the targeted faults. Block B, measuring 2.5 x 2.5 km, is located to the south of the northern PEZ in Noordhinder North. Block C, with dimensions of 2.4 x 3.0 km, is situated near the northwest boundary of the PEZ, spanning areas within both Fairybank and Noordhinder South. Block D, located between Blocks A and C, covers 2.5 x 1.5 km and was added to address gaps in data interpretation and enhance the understanding of transitions between the observed structural styles in Blocks A and C. The PES survey in each block was conducted with a narrow line spacing of 40 to 60 m to build a high-

resolution pseudo-3D dataset. This narrow spacing was essential to ensure the continuity of the data, particularly for identifying the geometry of faults in the Kortrijk Formation.

Further details on the acquisition and processing of geophysical data are thoroughly discussed in the Deliverable 1.2 report by Mestdagh, et al. [24] .

2.2 Seismic Reflection Interpretation

The Kortrijk Formation is primarily composed of extremely high-strength marine clays, interspersed with silt and sand beds. In seismic reflection profiles, this formation appears to have strong reflectors within the formation which can be used as key horizons during seismic interpretation. Because the seismic profiles have limited penetration depth, especially on the TOPAS and PES profiles in which penetration reaches only the depth of the first multiple, no single profile in this project captures the entire formation's thickness, and no horizon is visible constantly across the entire area of the PEZ. To address this, we used overlapping TOPAS lines to trace the continuation of strong reflectors from the southwest to the northeast of the PEZ (**Figure 2.2**). This approach allowed us to identify key horizons for structural mapping, ranging from Horizon 3c01 (upper part of the formation, visible in the northern PEZ) to 3c15.1 (lower part of the formation, visible in the southern PEZ). Additionally, the thicknesses between horizons are relatively constant, so we use their intervals as the key indicators during interpretation. Moreover, faults are identified where discontinuities in the horizons indicate fault displacement.

Seismic interpretation was conducted using the Kingdom Suite (software by S&P Global), producing horizon depths and fault segments in two-way time (TWT; in milliseconds). Each fault segment is characterised by two termination points: a shallow tip and a deep tip. The resulting horizon and fault data were then transferred to Leapfrog Geo (software by Seequent) and QGIS (open software) for further analysis. To facilitate interpretation, the depths of both horizons and fault segments were converted from TWT to depth using a constant velocity of 1650 m/s. See **Appendix** for figures describing the results of the mapping before further analyses: **Figure A.1-3** for Block A, **Figure A.6-8** for Block B, **Figure A.11-13** for Block C, and **Figure A.16-18** for Block D.

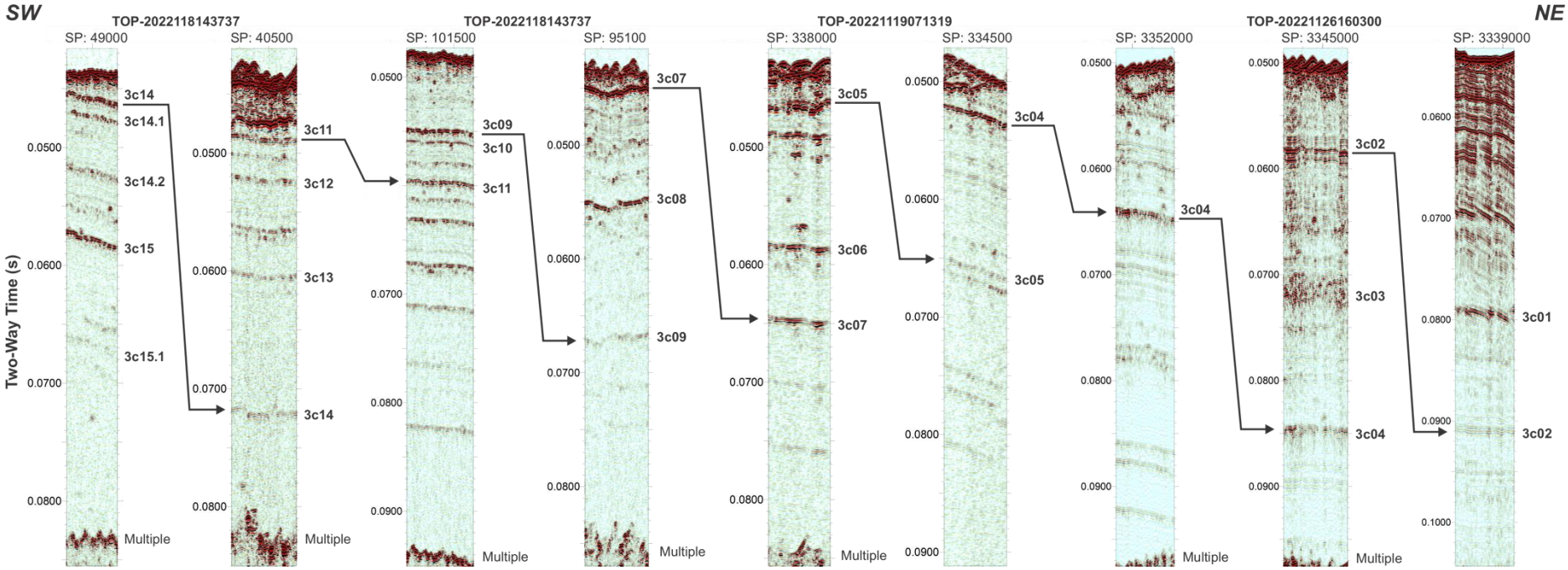

Figure 2.2. Identification of the strong reflectors on TOPAS profiles within the PEZ as the key horizon to map the structural distribution of the Kortrijk clay formation. Multiple profiles used for the identification due to the generally northeast dipping layers where reflectors terminate at the maximum penetration of the seismic profile. Strong reflectors noted from 3c01 as the shallowest to 3c15.1 as the deepest.

2.3 Fault Correlation

Fault correlation is conducted in QGIS based on specific principles to systematically assign fault segments to faults. The primary criteria include the proximity between fault segments and their dip orientations, ensuring that dips are similar or not significantly different. For instance, in **Figure 2.3**, example 1 demonstrates a simple correlation where all segments are grouped into one fault due to their proximity and alignment. Example 2 illustrates the division of segments into two faults due to their proximity but distinct dip direction. In example 3, overlapping segments with the same dip directions suggest possible fault splays, leading to their assignment as three separate faults. Example 4 involves segments with perpendicular dip directions, where one set terminates into the other; these are divided into one main fault and another separate set of faults. Lastly, example 5 shows segments that appear continuous, but their interaction with perpendicularly cutting segments leads to their assignment as four distinct faults due to unclear terminations. This structured method ensures consistency in fault correlation and avoid interpretation bias at this early stage of analysis.

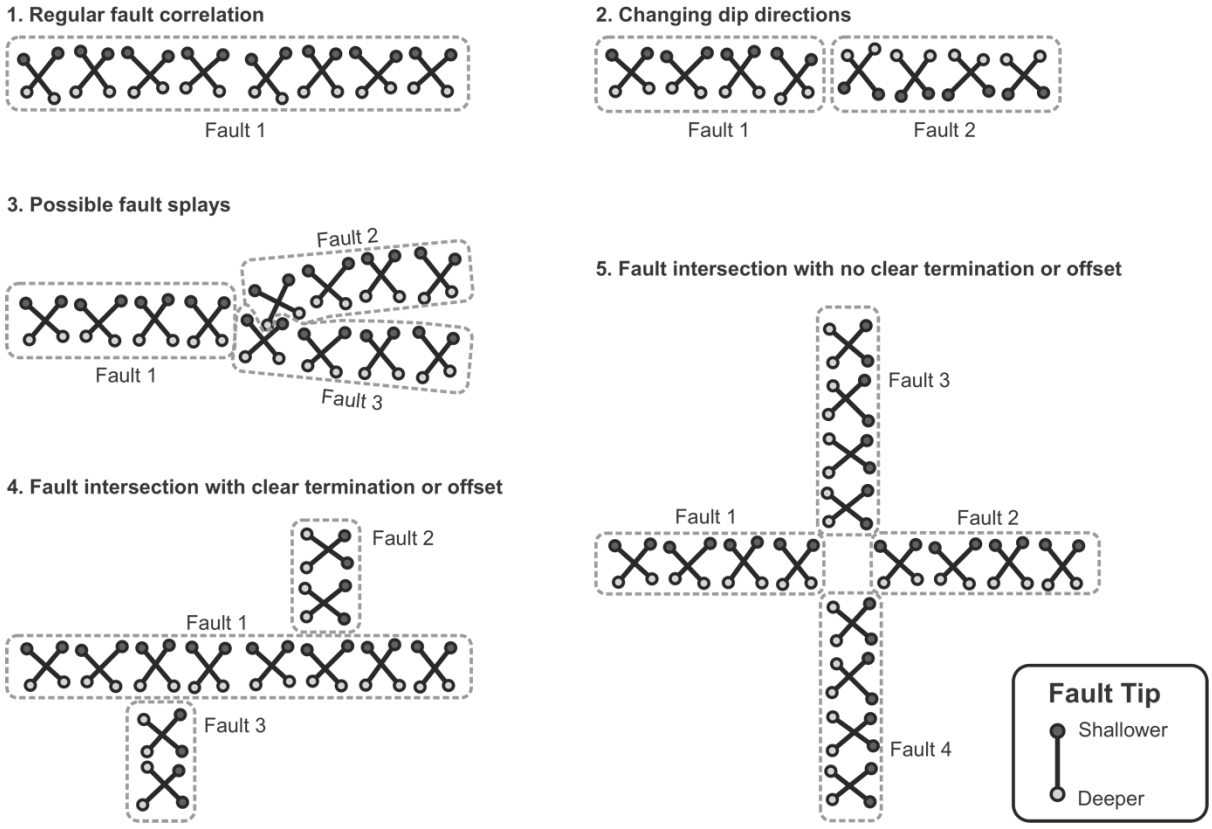

Figure 2.3. Schematic diagrams on the principle of the fault correlations based on the configuration of the fault sticks and the depth of the tips.

2.4 3D Modelling

Faults were modelled individually using Leapfrog Geo to ensure precise and realistic representation. The modelling process involved several key stages, as shown in the **Figure 2.4**. First, fault segment data were input as points with XYZ coordinates (**Figure 2.4A**). A mesh surface was then created based on these data points, with a surface resolution set to 15 m or less, depending on the density of data points available (**Figure 2.4B**). The variogram parameters were defined to use a linear interpolant, with a total sill of 2000 m^2, a nugget effect of 100 m^2, a range of 100 m, and accuracy of 1 m. After the interpolant was applied, individual faults were verified to

ensure continuity and realistic geometry (**Figure 2.4C**). Key horizon data were also gridded into mesh surfaces in Leapfrog Geo with a surface resolution of 10 m. These models, both faults and horizons, were then exported to QGIS as surface elevation models in grid file format for further analysis.

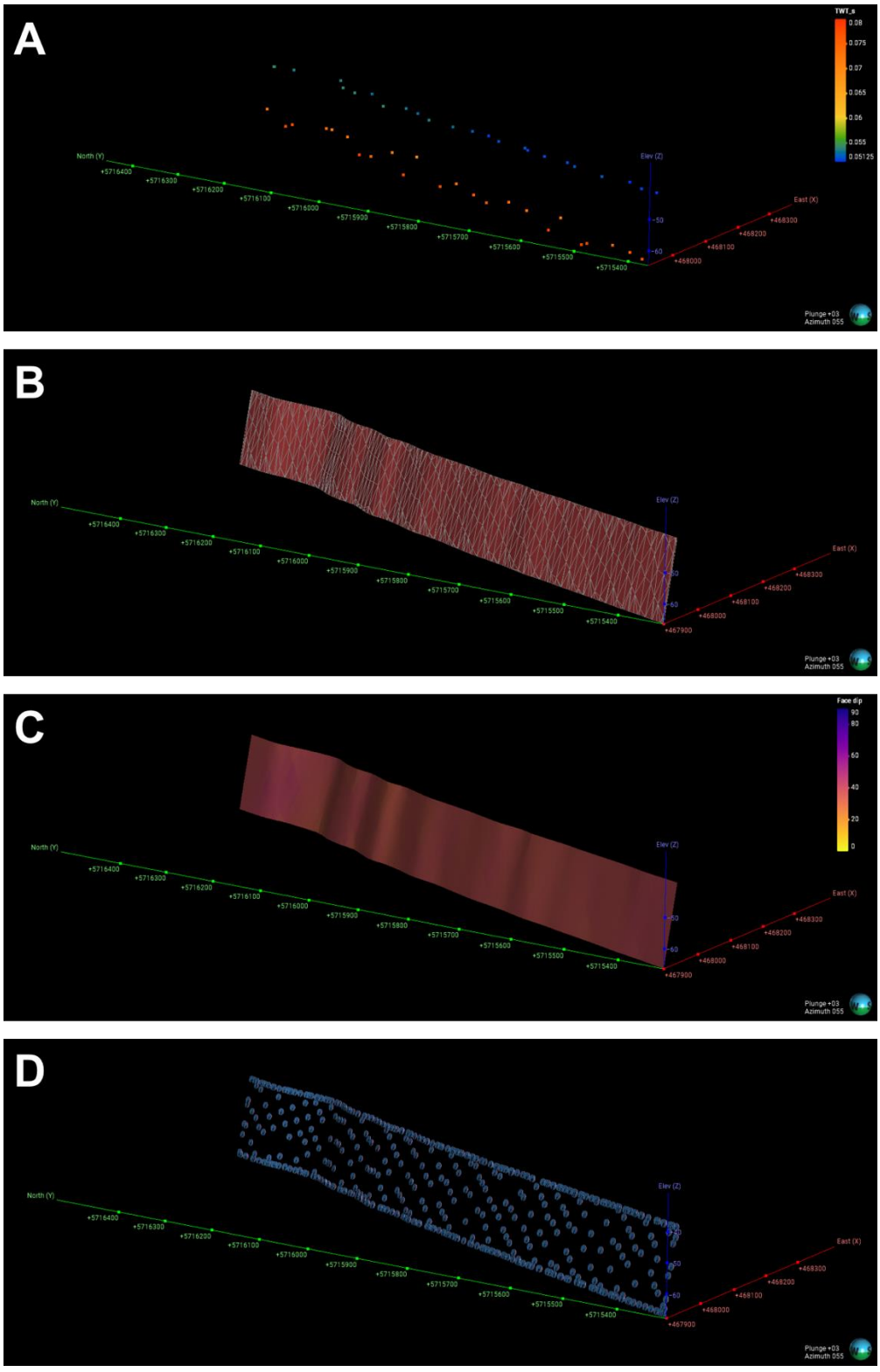

Figure 2.4. 3D fault modelling on Leapfrog Geo where fault tips used as the input (A) to generate triangulated meshes (B) as fault surface (C). The meshes then used to estimate the general geometry (strike and dip) of the fault (D).

2.5 Fault Analyses

The analyses presented in this report focuses on the geometry and spatial distribution of faults, highlighting key properties such as strike, dip, length, and spacing (**Figure 2.5**). Strike and dip values are determined through structural estimation in Leapfrog Geo, where the average orientation is calculated from the fault surface meshes. These values are further analysed using stereonet-based contour and rose diagrams to better understand the trends in fault geometry. Fault length is assessed by examining the fault elevation model exported from Leapfrog Geo into QGIS. A mid-elevation contour of the fault model is generated and measured to estimate its length.

Spacing analysis is performed using scanline methods, applying two orthogonal directions aligned with the northeast and northwest block boundaries of the study area (**Figure 2.5B**). The scanlines in each set are spaced at regular intervals of 50 m. This alignment ensures a representative spatial evaluation across the blocks. The measured spacing (dx_1, dx_2, dx_3, ..., dx_n from northeast scanlines; dl_1, dl_2, dl_3,..., dl_n from northwest scanlines) is subjected to statistical analysis to characterise fault distribution. Arbitrary scanlines perpendicular to the faults are avoided as it would prioritise data-rich zones within the block centres. The use of block-aligned scanlines enhances consistency and facilitates a comprehensive perspective of fault spacing within the block.

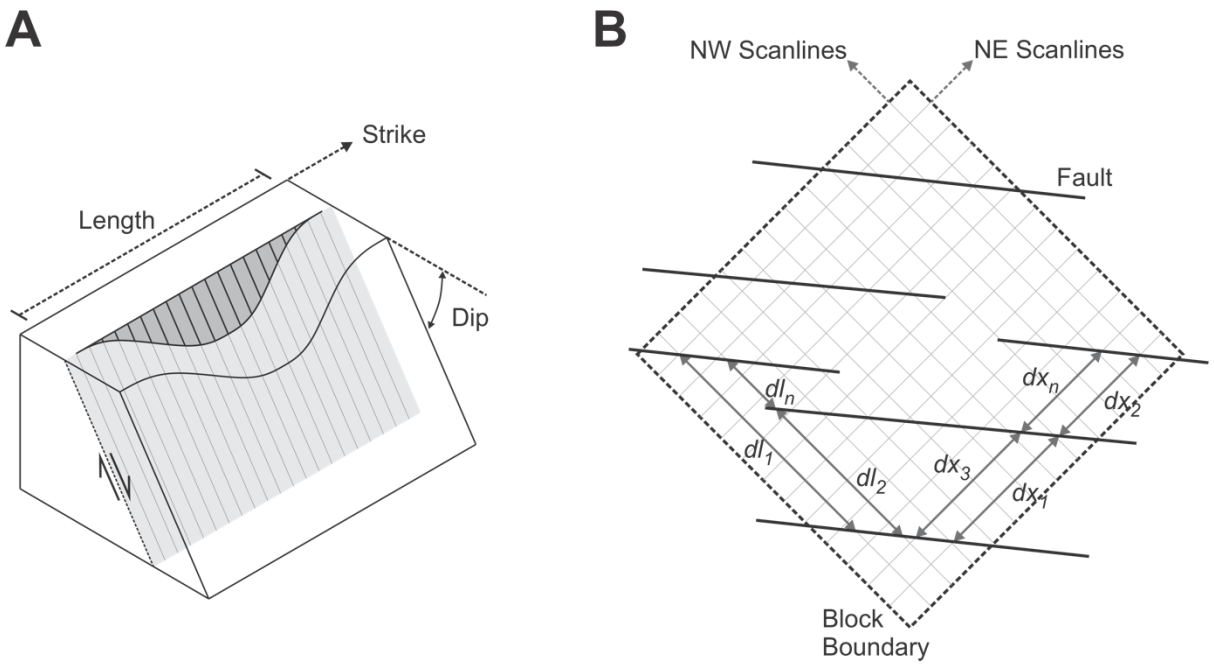

Figure 2.5. Schematic diagrams of fault properties (A; i.e., fault length, strike, and dip) and scanlines in two main directions (NE and SW) for fault spacing analysis based on the blocks' geometry (B).

3 Results

3.1 Princess Elisabeth Zone

The structural styles across the PEZ vary among Fairybank, Noordhinder South, and Noordhinder North. In Fairybank, shown on a seismic profile in **Figure 3.1**, the faulting is characterised by regularly spaced normal faults that appear like a domino-style faulting. The spacing between faults varies from 30 to 120 m, reflecting a systematic arrangement of the fault network. The horizons on hanging wall are curved toward the fault plane, suggesting the presence

of fault damage zones. The fault geometry is generally uniform, with an apparent dip measured on the profile ranging from 50° to 60°. Most faults dip toward the southwest, although a few dip to the northeast on the profile. Fault displacement is relatively uniform, ranging from 2 to 5 m, but displacement increases with depth along individual faults.

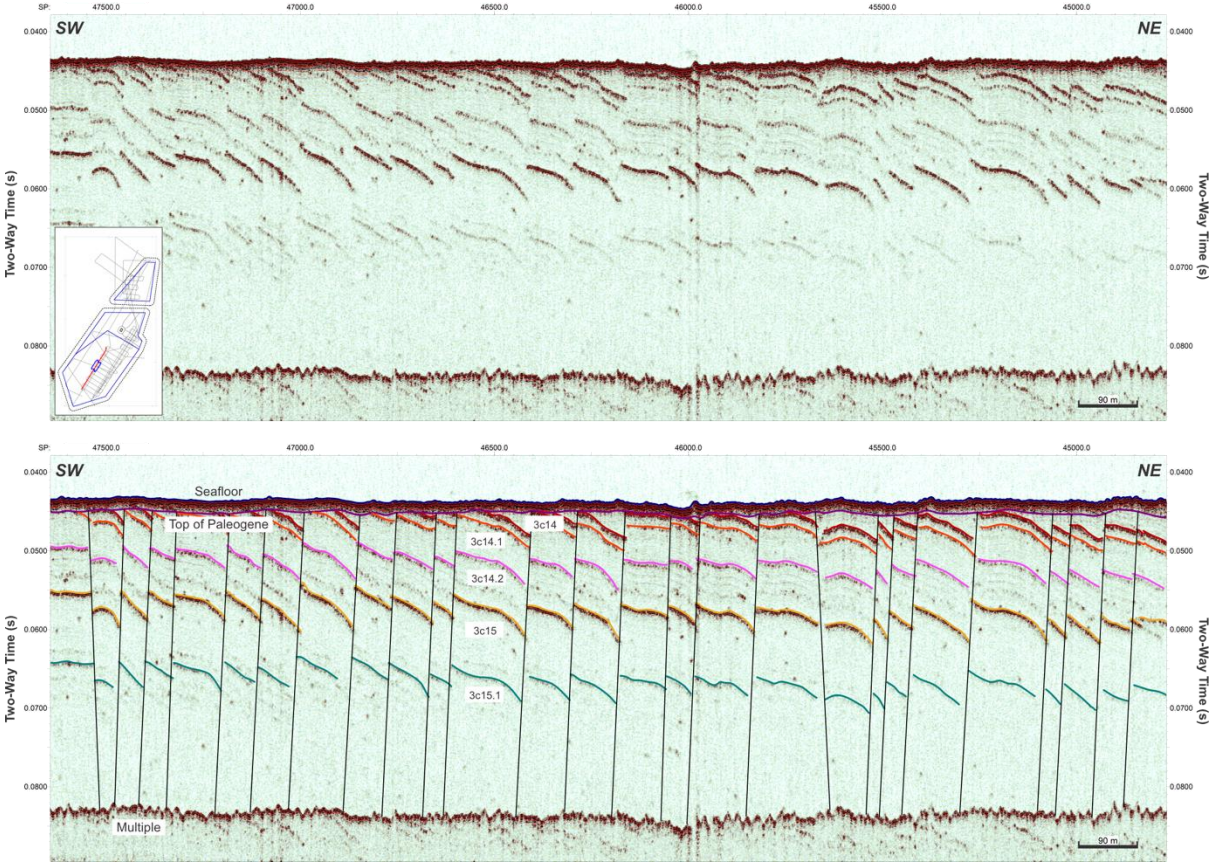

Figure 3.1. Seismic section (top) and seismic interpretation (bottom) from the Fairybank, in the southern part of the PEZ, showing dense fault spacing from about 40 to 100 m underneath thin Quaternary sand layer.

In Noordhinder South, shown on seismic profile in **Figure 3.2**, faults exhibit varying termination depths, with some faults terminating under deeper layers (e.g., 3c07 and 3c08) rather than at the unconformity (Top of Paleogene). These deeper fault terminations have influenced the overlying strata, resulting in the formation of fault-propagation fold structures. The faulting is normal as also observed in Fairybank, with most faults dipping toward the southwest and only a few dipping toward the northeast. The apparent dip of the faults ranges from 30° to 50°. Fault displacement varies from zero, where folds occur above the faults, to approximately 3 m, with displacement increasing with depth. The spacing between faults is wider than in Fairybank, ranging from 50 to 250 m. Moreover, the faults in this profile appear as clearly displaced blocks, with no apparent features of layers curving toward the fault planes as observed in Fairybank.

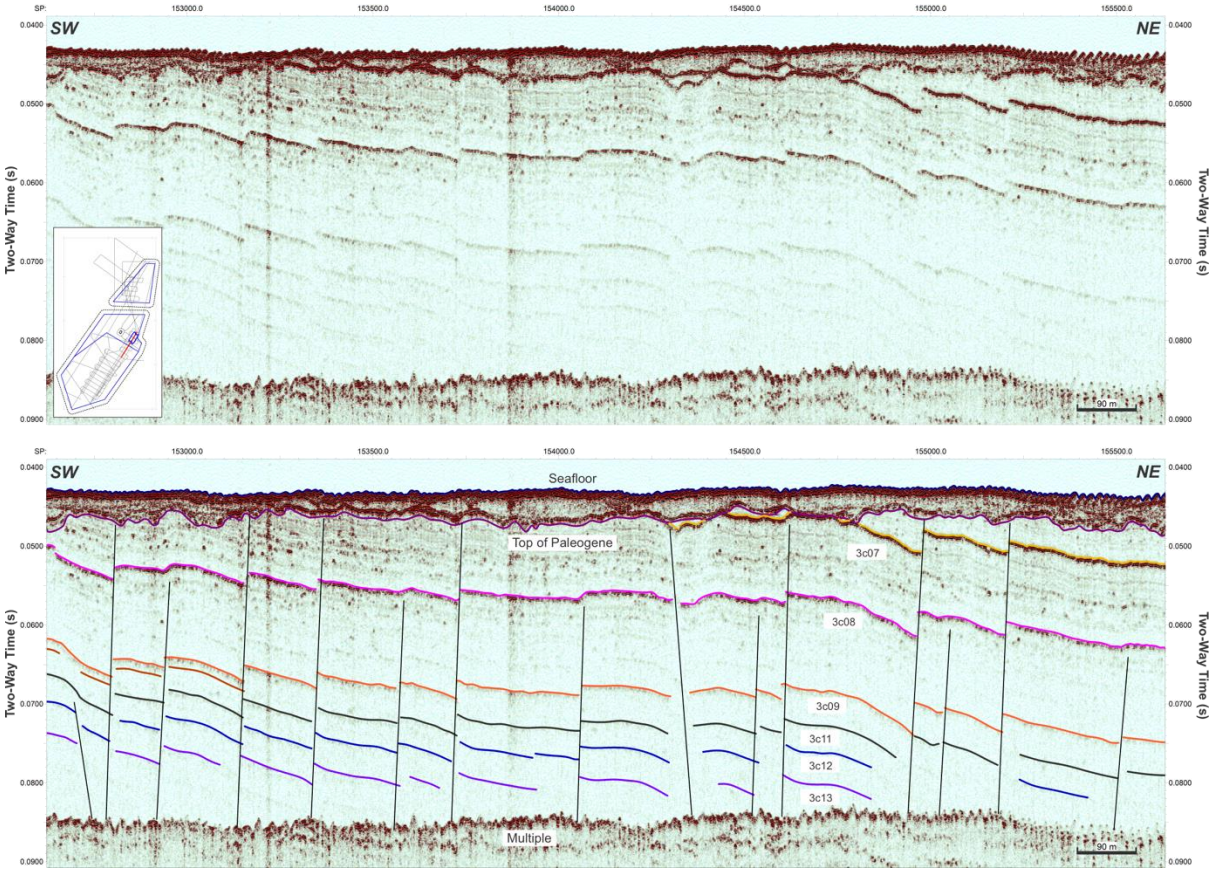

Figure 3.2. Seismic section (top) and seismic interpretation (bottom) from the Noordhinder South, in the central part of the PEZ, showing generally northeast dipping layer, wide fault spacing from around 50m to 250m, and thick Quaternary sand layer.

In Noordhinder North, shown on seismic profiles in **Figure 3.3**, only a few faults are observed, with orientations dipping toward both the southwest and northeast. The faults exhibit apparent dips ranging from 30° to 50°, similar to those in Noordhinder South. Fault spacing is notably larger, reaching up to 600 m. One fault shows displacement increasing with depth, accompanied by minor folding in the overlying strata, as observed before. The other fault displays a deeper fault tip where displacement decreases with depth, terminating above Horizon 3c06 and resulting in a monocline fold beneath it. The continuation of this fault to shallower depths is unclear due to Horizon 3c03 consisting of nodule reflectors forming a distinct layer.

Despite the variation across the PEZ, the faulting shares several similarities. All faults terminate below or at the unconformity with the overlying Quaternary sand deposits, indicating that they are neither active, propagating, nor reactivated since the Quaternary period. The faults are normal faults, consistent across the profiles. Additionally, the profiles reveal a general sedimentary layer structure, with layers dipping toward the northeast, aligning with previous geological studies of the area. Due to the limited depth of seismic penetration, constrained by the first multiple, and the northeastward dip of the layers, each horizon terminates toward the northeast on the profiles and maps. As a result, observations in the focused study area (Blocks A, B, C, and D) utilised different key horizons for interpretation: Horizon 3c13 for Blocks A and D, Horizon 3c04 for Block B, and Horizon 3c12 for Block C (**Figure 3.4**).

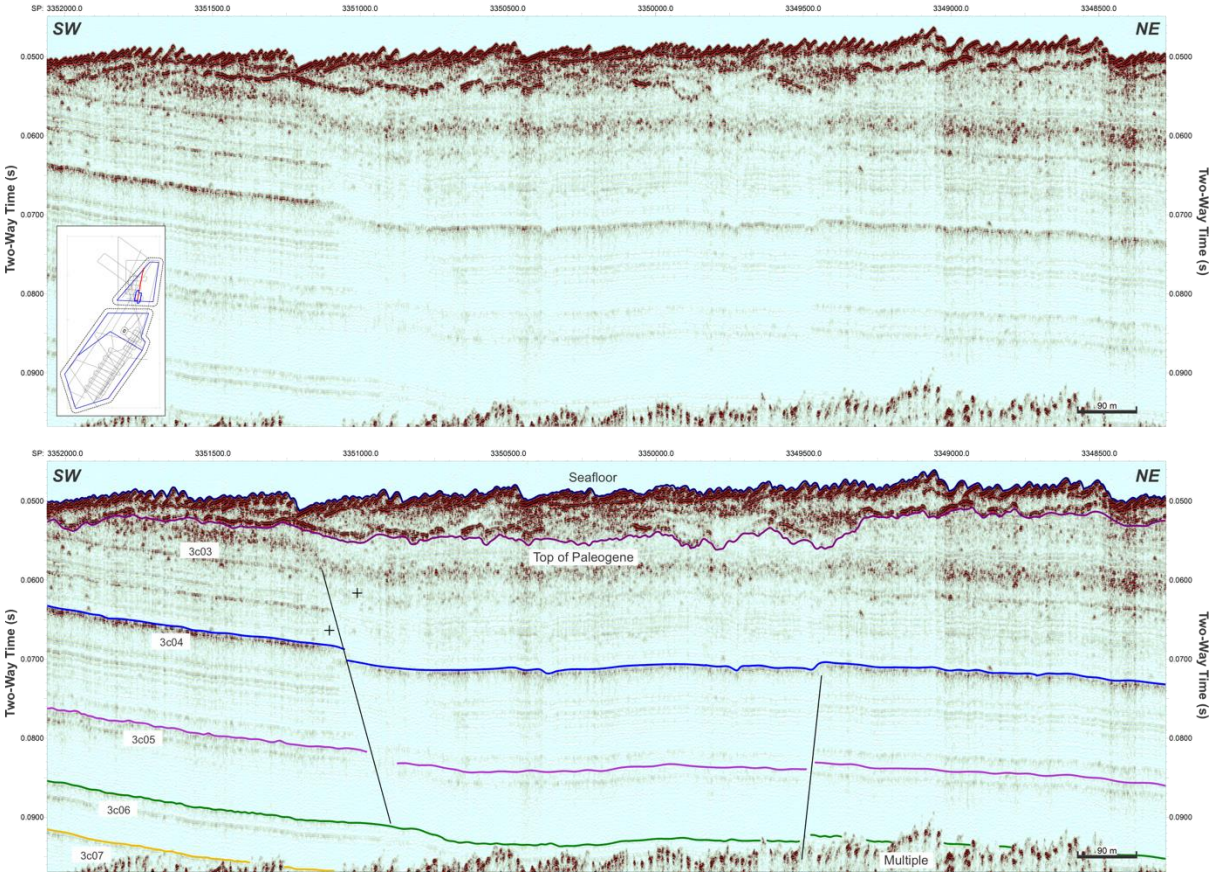

Figure 3.3. Seismic section (top) and seismic interpretation (bottom) from the Noordhinder North, in the northern part of the PEZ, showing sparse distribution of faults with spacing >500m and very thick Quaternary sand layer.

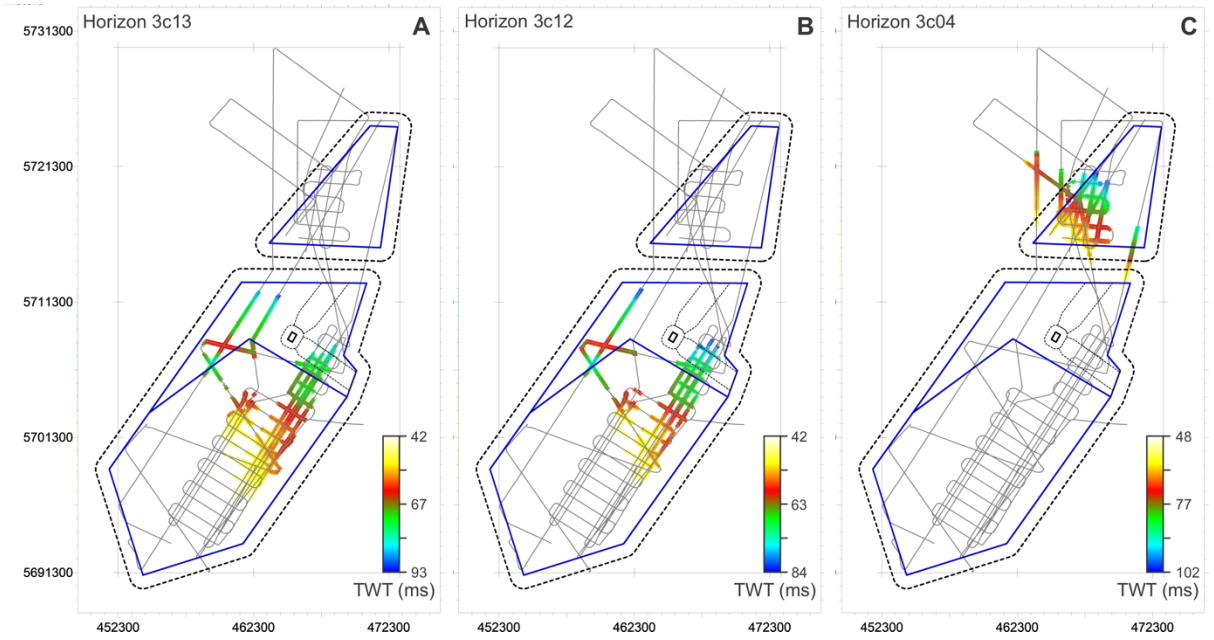

Figure 3.4. Horizon mapping of several key horizons throughout the PEZ which cover the extent of the detailed pseudo-3D blocks: (A) Horizon 3c13 for Block A and D; (B) Horizon 3c12 for Block C; (C) Horizon 3c04 for Block B;

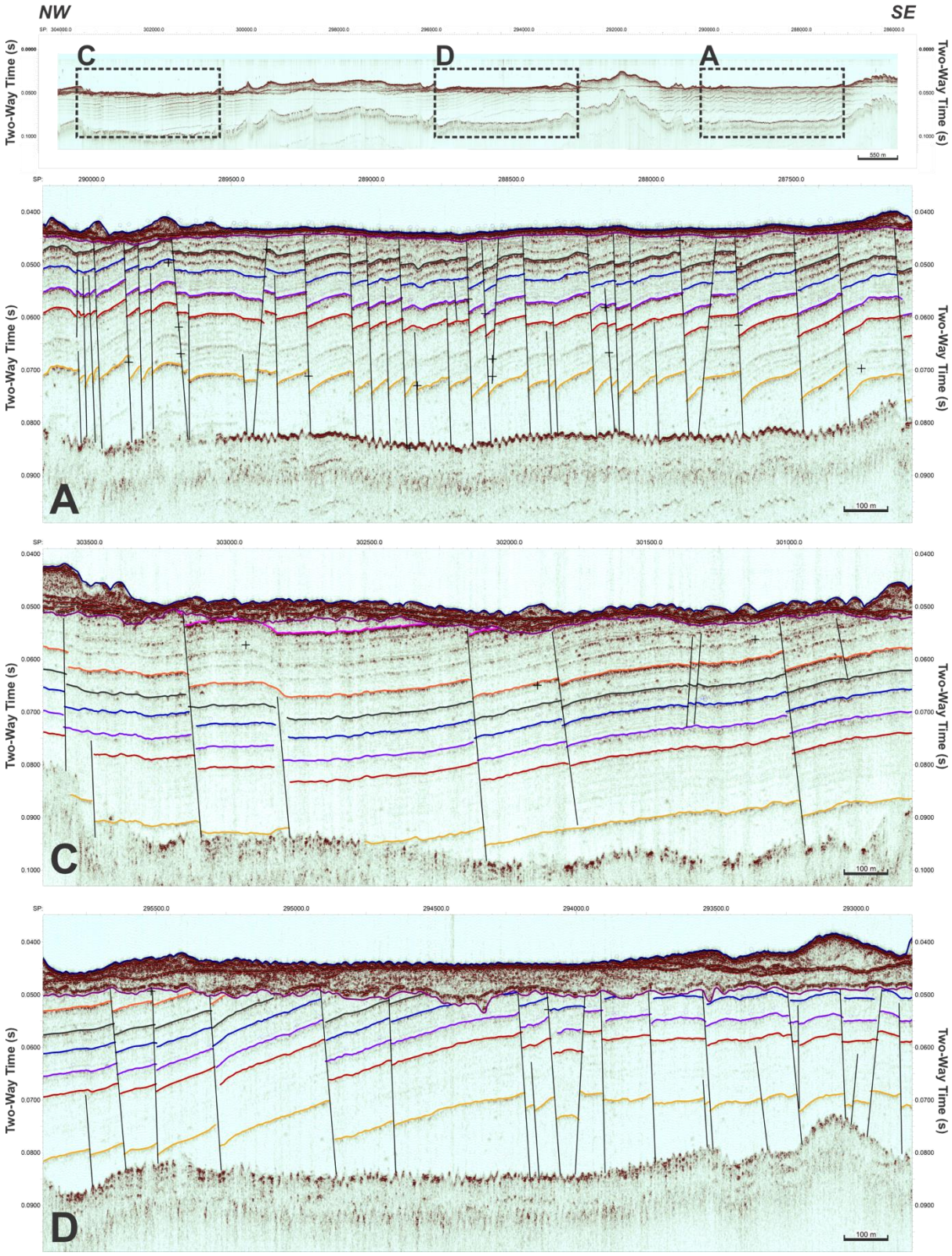

Figure 3.5. Seismic section connecting Block A, C, and D, showing changes in structural styles from a dense faulting in the southeast (A) to a relatively sparse in the northwest (C). Changes between structural styles in Block A and C is possibly located within Block D (D).

Changes in structural styles from Fairybank in the southwest to Noordhinder North in the northeast suggest that these variations may reflect changes vertically, from the deeper to the shallower parts, within the Kortrijk Formation. However, observations on a seismic profile

connecting Blocks A and C (**Figure 3.5**) reveal that structural style changes also occur laterally within a set of horizons (3c12–3c15), which has led to further investigation in Block D. In the southeastern part of the profile (**Figure 3.5A**), where Block A is located, faults are densely spaced, ranging from 50 to 100 m. In contrast, the northwestern part of the profile (**Figure 3.5C**), near Block C, shows widely spaced faults, with spacing increasing to 150–300 m. This significant change in fault spacing is inferred to occur at the centre of the profile, at Block D where a clear transition in structural styles is evident (**Figure 3.5D**).

The detailed fault characteristics of each block are discussed below.

3.2 Block A

Based on seismic profiles (**Figure 3.6**) and fault maps of Block A (**Figure 3.7** and **Figure 3.8**), faults are narrowly and regularly spaced, predominantly dipping toward the south. Distinct faulting features include fault splays, where secondary faulting terminates on the main fault plane. Most faults shown on the seismic profile exhibit vertical displacement that increases with depth, although a subset shows a contrasting behaviour where throw decreases with depth until termination at the bottom tip of the fault. Additionally, minor faulting (i.e., shorter in length) is observed, with displacement peaking at the centre of the fault. This minor faulting often coincides with folding structures occurring both above and below the faults. Fault relay structures are also present, where two closely spaced faults interact. In such instances, the bottom tip of one fault aligns near the shallow tip of the other, forming folding structures in the intervening layers.

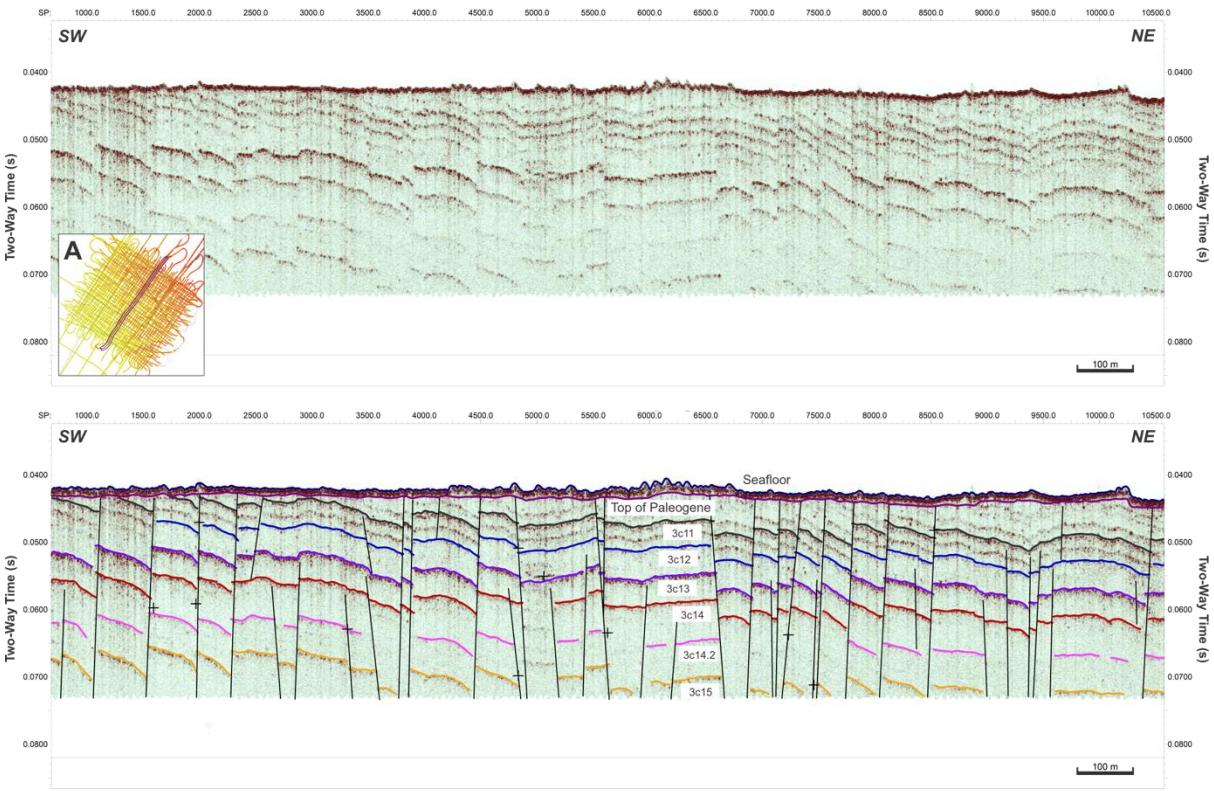

Figure 3.6. Seismic section (top) and seismic interpretation (bottom) from Block A, showing dense faulting with some minor faulting terminating within layers and fault splay feature.

The total number of faults modelled in this block is 337. Fault geometry is highly consistent, with 86% of faults concentrated at a single orientation peak (**Figure 3.9**). The majority

align along an ENE–WNW direction (median strike of N88°E, ranging between N80°E and N90°E), while minor faults (<10%) extend in a north-south orientation (N0°E–N10°E). Median fault dip is steep at 64°, ranging from 55° to 70°. Fault spacing exhibits relatively similar spacing in both scanline directions (**Figure 3.10** and **Figure 3.11**). In the northwest direction, the median spacing is 79 m, with a peak at 75 m, and most faults are spaced between 50 and 100 m. Similarly, northeast-directed spacing has a median of 65 m, a peak at 50 m, and a majority range between 50 and 100 m. Fault lengths vary widely, with a median of 119 m and a range extending from 7 to 787 m (**Figure 3.11**). However, fault lengths are generally short, peaking at 50 m, and predominantly ranging between 25 and 100 m.

Penetration of the Sparker seismic profile (**Figure 3.12**) reaches the top of the Cretaceous, showing that this remains relatively flat despite the intense faulting in the overlying layers. This corroborates earlier observations that the faulting is essentially layer-bound, i.e. bound to the Kortrijk Formation.

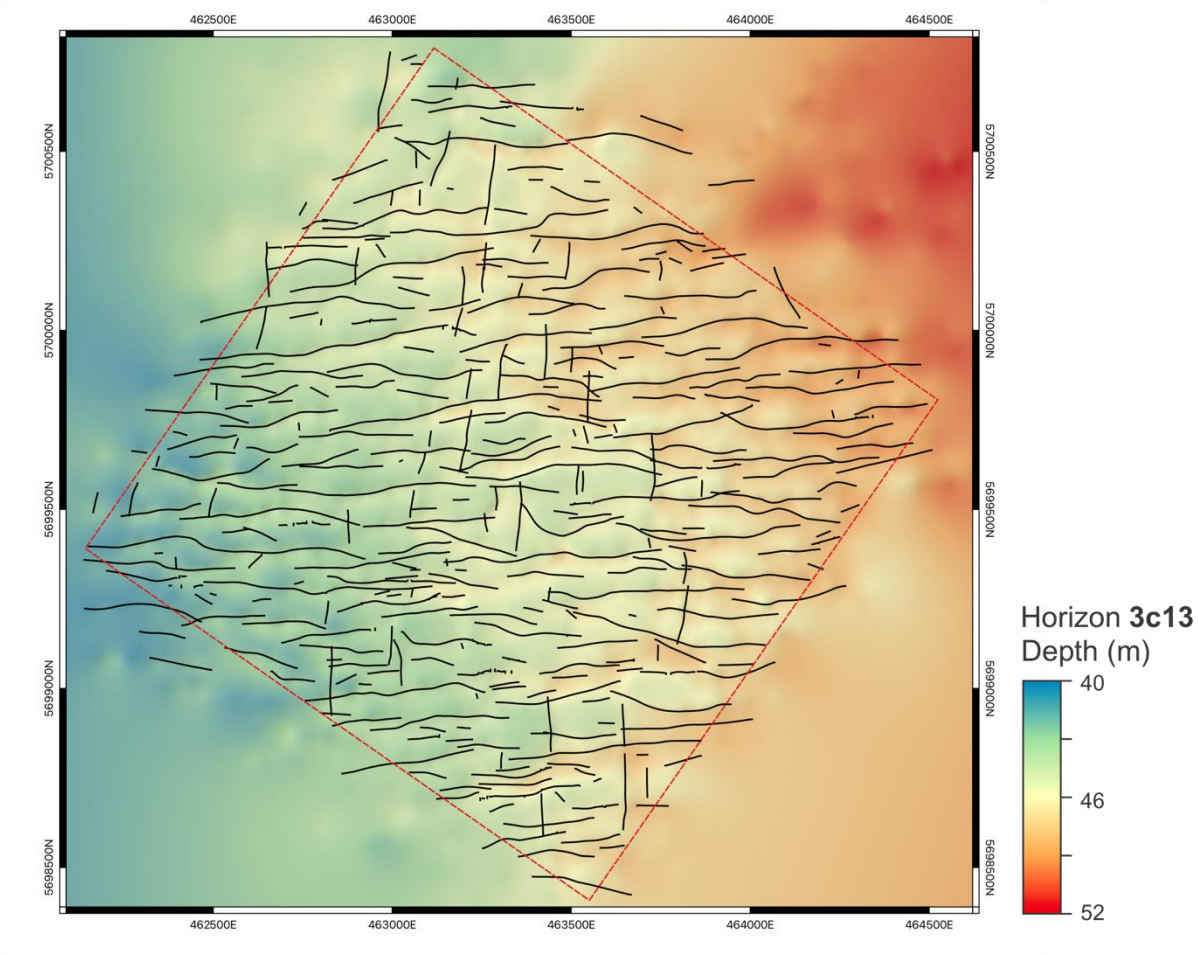

Figure 3.7. Distribution of faults in Block A, featuring the total number of 337 correlated and modelled faults within the block. Faults to appear orientated mainly in east-west direction with minor faulting in north-south direction.

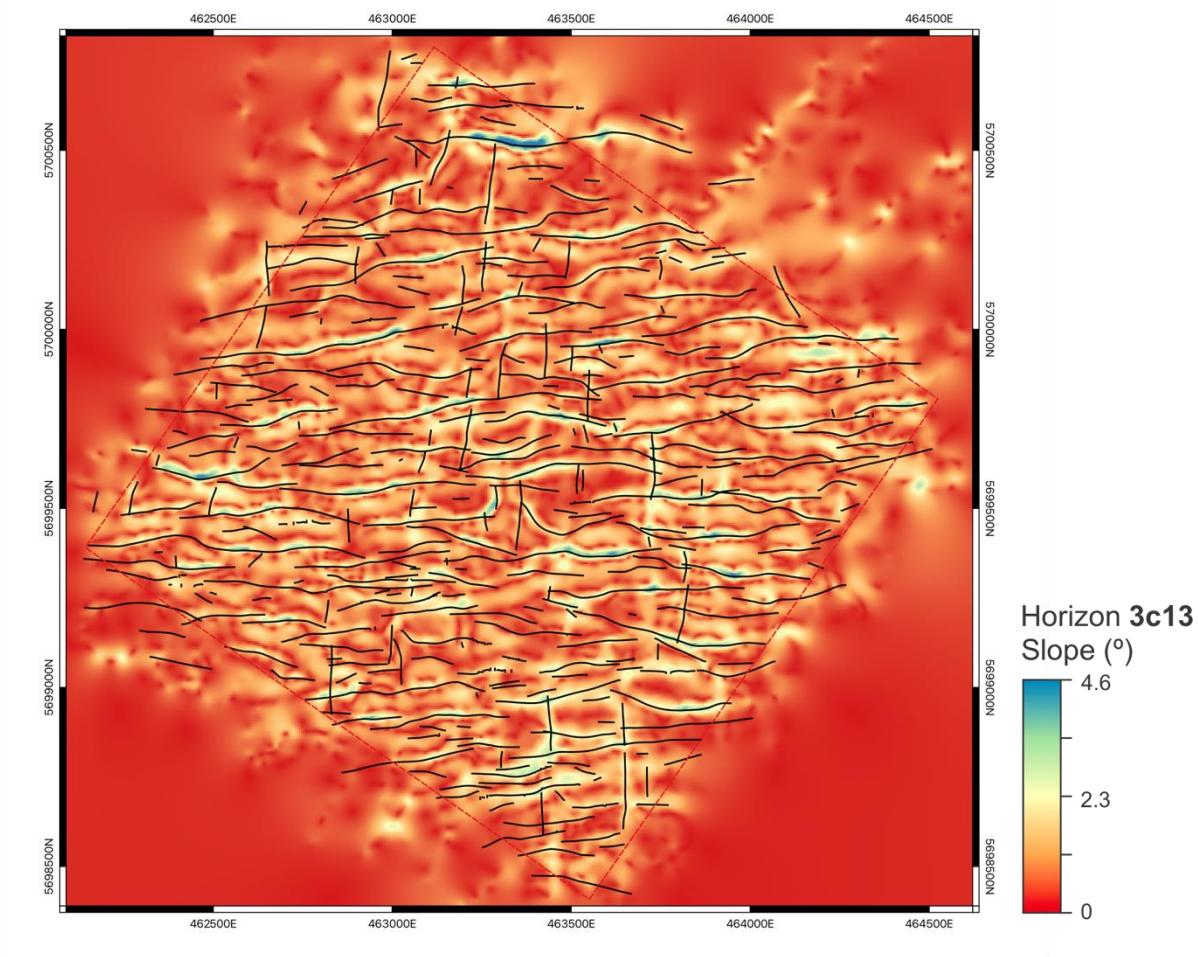

Figure 3.8. Slope map of the gridded Horizon 3c13 to confirm the location of faults in Block A.

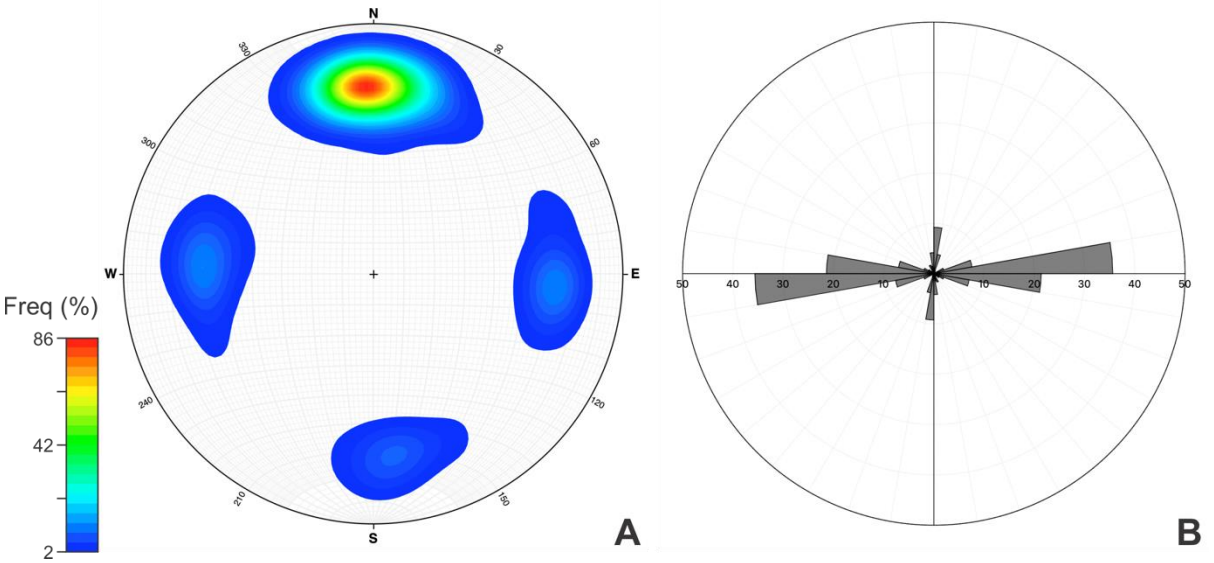

Figure 3.9. Analyses of fault geometry in Block A: (A) Contour diagram indicates that the general geometry of the fault is N88°E/64; (B) Rose diagram suggests two sets of fault orientations where the main faults orientation is in N80°E–N90°E while minor fault orientations in N0°E–N10°E.

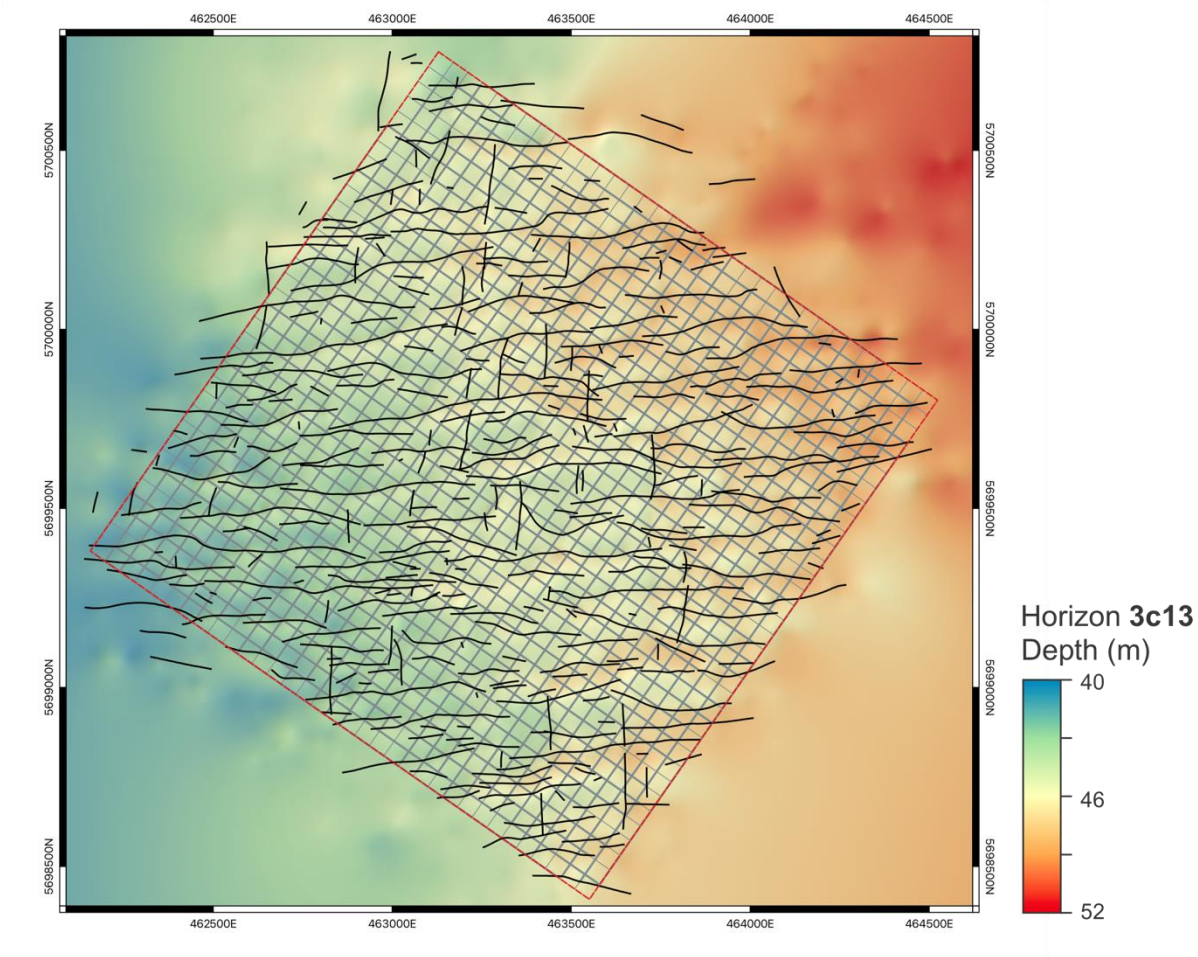

Figure 3.10. Scanlines set in Block A, with 50 m spacing parallel to block boundaries in NE and NW directions, to measure the fault spacing.

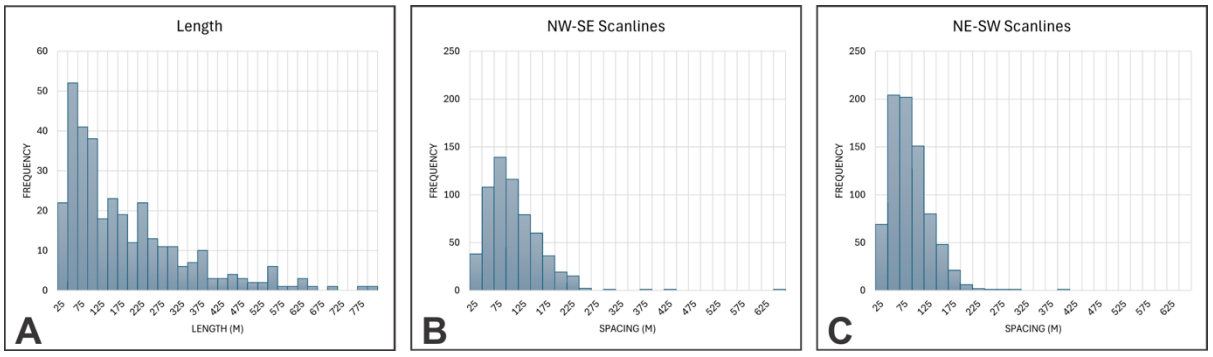

Figure 3.11. Histogram of the fault length (A) and the fault spacings in NW (B) and NE directions (C) of Block A. Most faults in Block A have length less than 100m. The fault spacings peaks between 25 to 100 m in both NW and NE directions.

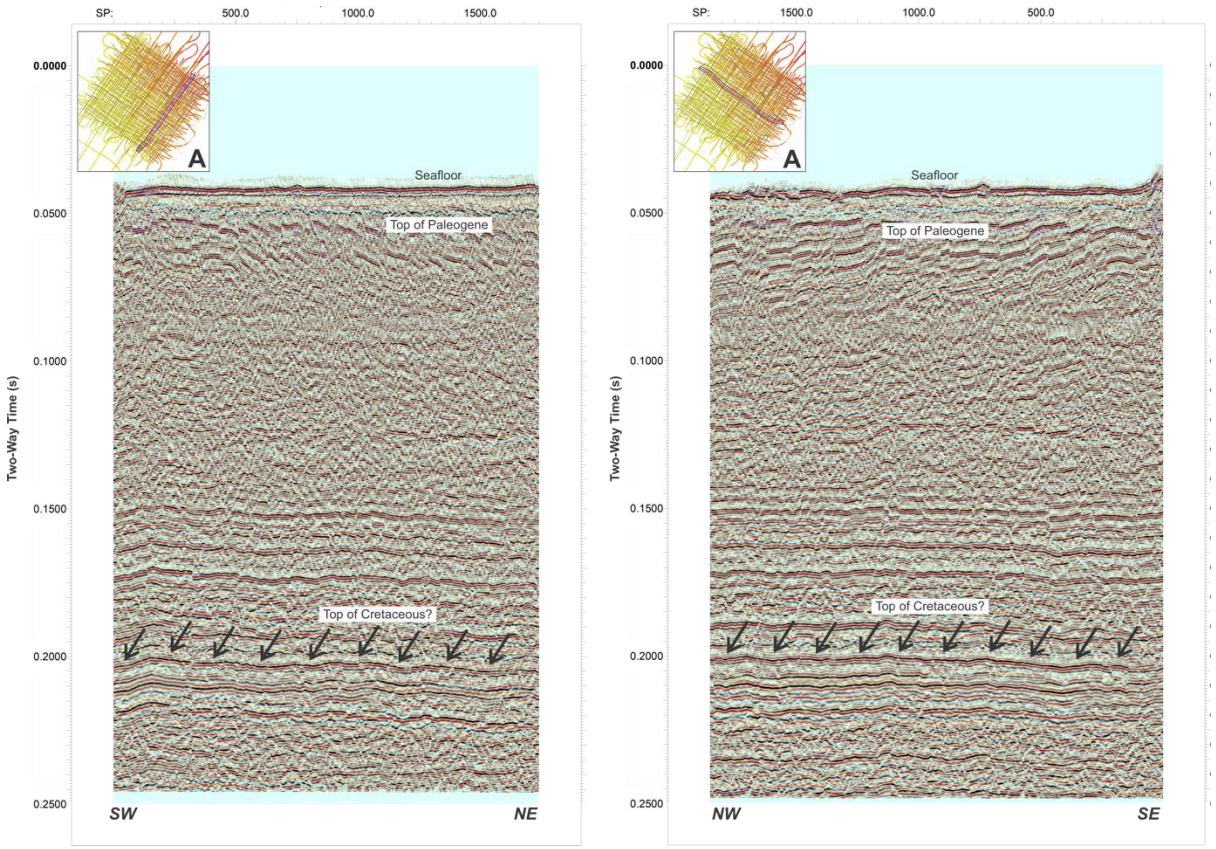

Figure 3.12. Sparker seismic section from Block A in NE-SW (A) and NW-SW (B) directions. The top of Cretaceous layer, possibly detected using this deeper sparker acquisition, appears continuous despite the faulted layers in the shallower depth.

3.3 Block B

Faulting in Block B, as observed from seismic profiles (**Figure 3.13**) and fault maps (**Figure 3.14** and **Figure 3.15**), is characterised by widely spaced faults, allowing folding structures with gentle limbs to be visible on the profile. The primary faulting orientation is in the NNE–SSW direction, with a few minor faults almost perpendicular to this trend, terminating on the main faults. Meanwhile, fold axes are parallel with the main orientation of the faults. Most faults in this block dip toward the west, although some dip toward the east, creating graben-like structures. Unlike sharply defined fault planes, the faults in Block B exhibit wider horizontal displacement, forming fault zones where fault thickness appears wider.

A total of 38 faults have been modelled in Block B. Statistical analysis in contour diagram shows two primary peaks in fault geometry, comprising 46% and 36% of the total faults (**Figure 3.16**). A rose diagram indicates that the faults at these peaks share a similar orientation (N10°E–N20°E and N190°E and N200°E) but exhibit opposing dip directions. A small number of faults are oriented perpendicular to this trend. For the first peak, the fault strike has a median orientation of N11°E, ranging between N10°E and N20°E, with a median dip of 38° and a range between 35° and 45°. For the second peak, the fault strike has a median orientation of N197°E, ranging between N190°E and N200°E, and a median dip of 40°, similarly ranging between 35° and 45°.

Fault spacing also differs depending on direction (**Figure 3.17** and **Figure 3.18**). In the northwest direction, almost normal to fault orientations, the median spacing is 301 m, ranging up to 726 m, with a peak spacing of 325 m, and with most faults spaced between 250 and 450 m. Spacing in the northeast direction has a much wider median of 515 m, ranging up to 1718 m,

though this scanline runs nearly parallel to the fault orientation and can be disregarded for meaningful spacing analysis. Fault lengths are considerably larger, with a median of 525 m, ranging from 54 to 1755 m. The length distribution peaks between 75 and 400 m (**Figure 3.18**).

Sparker profiles, particularly those perpendicular to fault orientation, indicate that the faults in Block B extend to deeper layers, potentially reaching the top of the Cretaceous (**Figure 3.19**). This faulting to the deeper layers suggests a faulting process at a larger scale in Block B, compared to Block A.

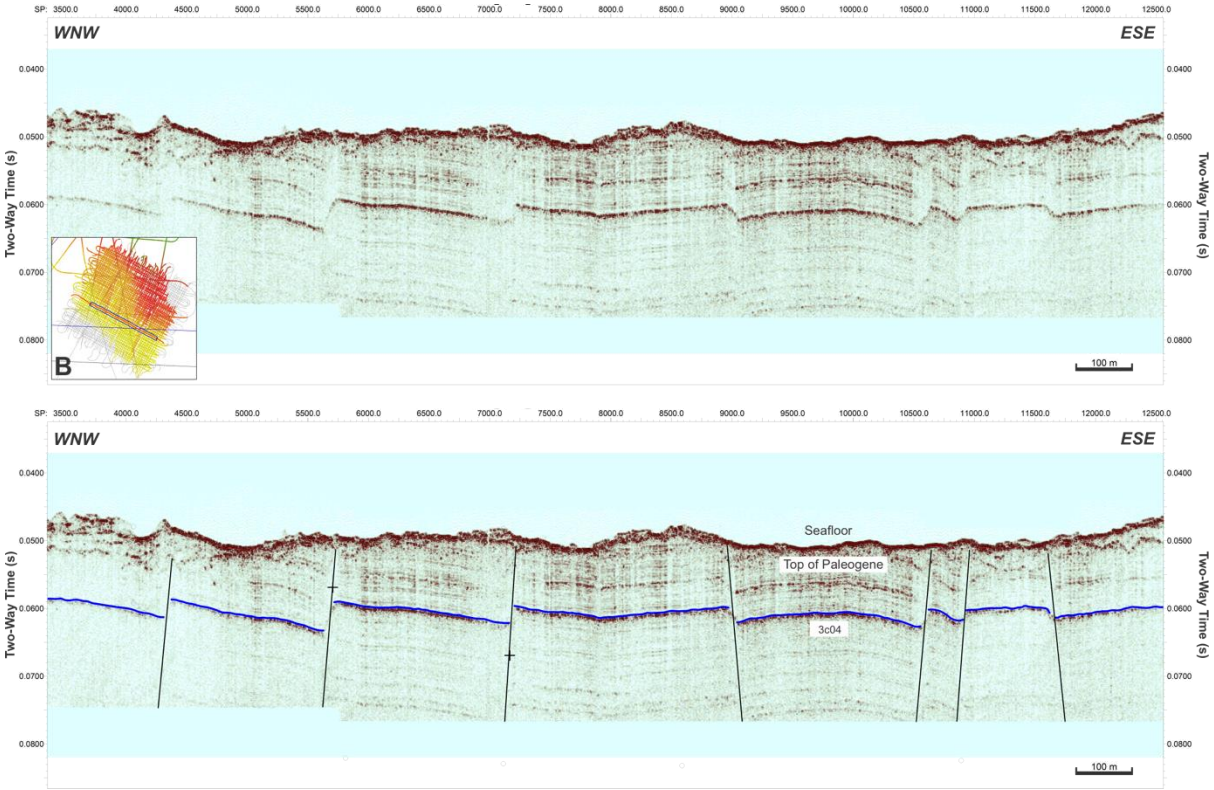

Figure 3.13. Seismic section (top) and seismic interpretation (bottom) from Block B, showing widely spaced faulting and folding structures within the block.

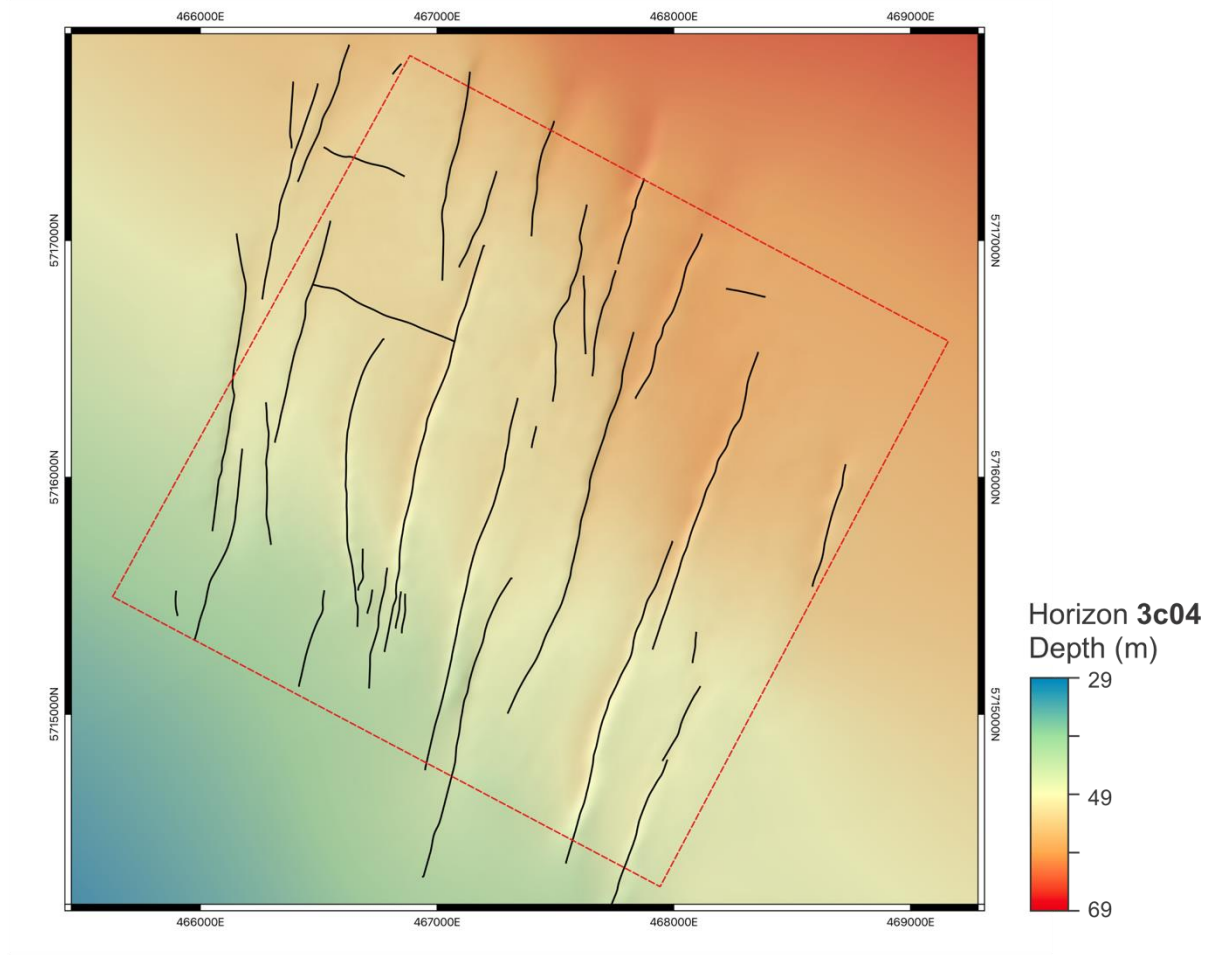

Figure 3.14. Distribution of faults in Block B, featuring the total number of 38 correlated and modelled faults within the block. Faults oriented mainly in NNE-SSW directions with various length up to 1.7 km.

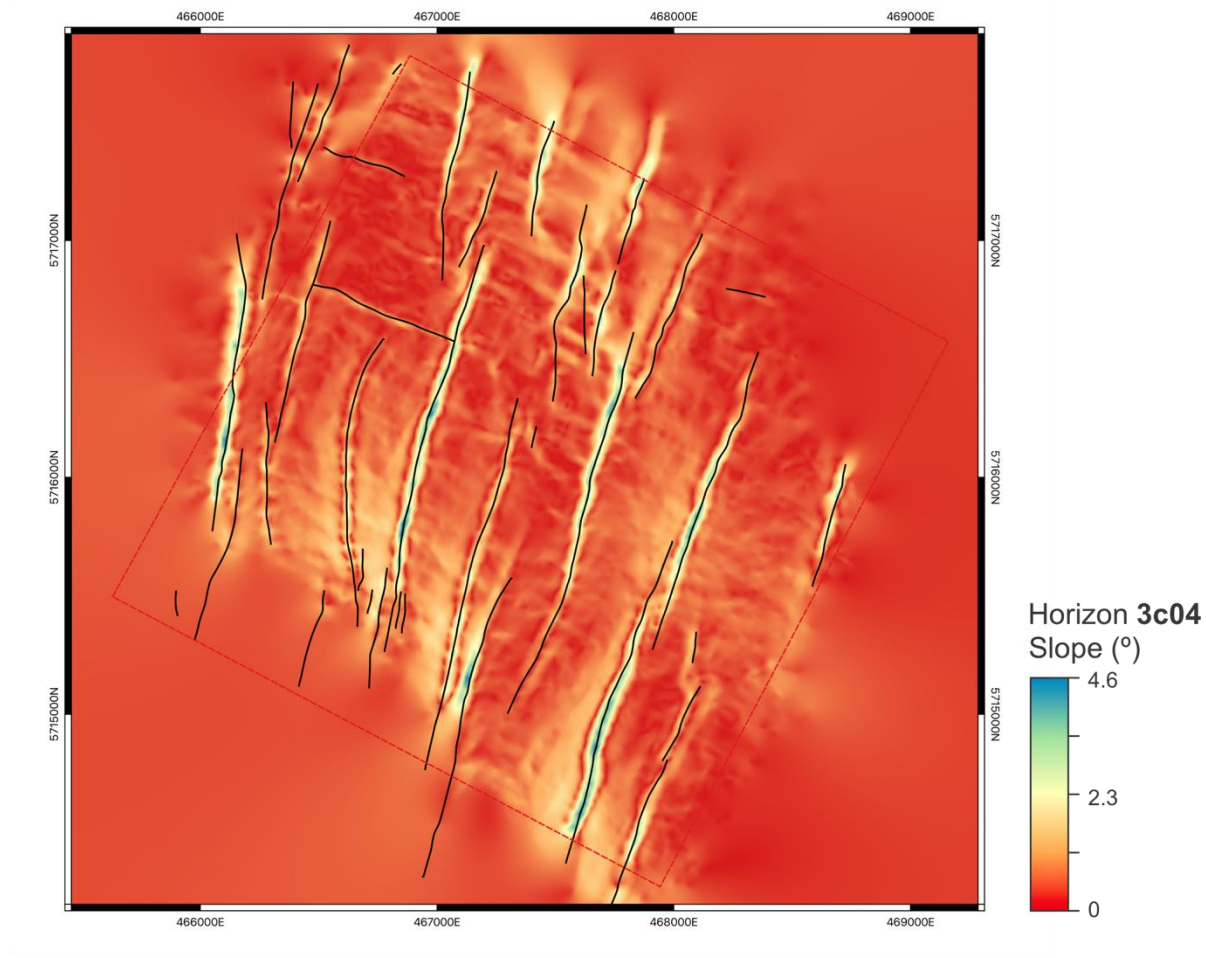

Figure 3.15. Slope map of the gridded Horizon 3c04 to confirm the location of faults in Block B.

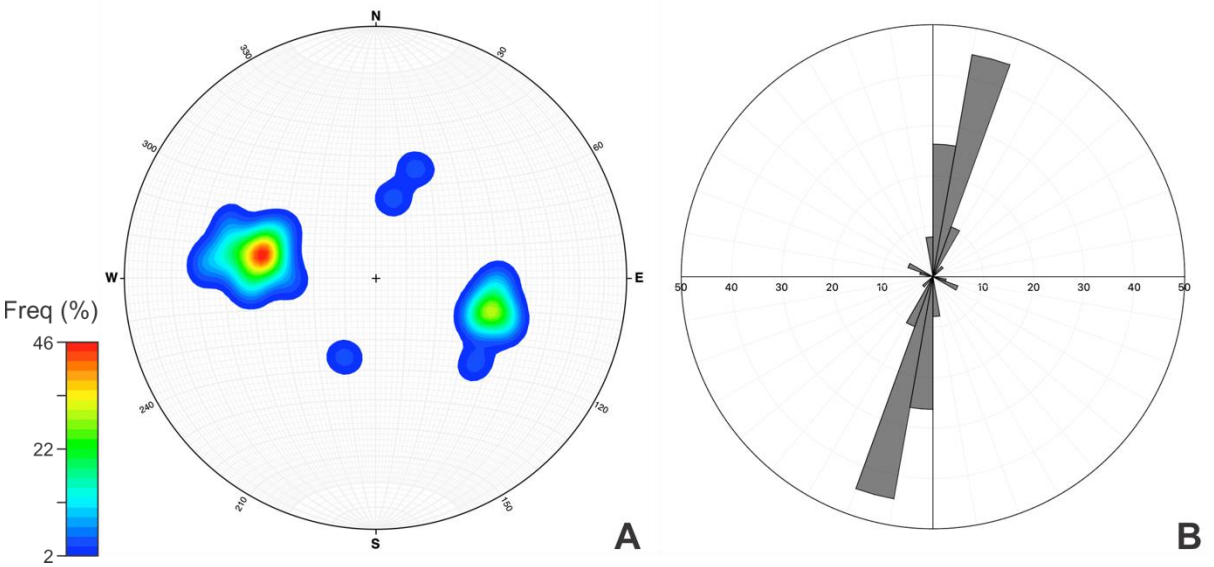

Figure 3.16. Analyses of fault geometry in Block B: (A) Contour diagram suggests that most faults oriented in similar direction but with opposing dip directions (N11°E/38° and N197°E/40°); (B) Rose diagram suggests the main orientations of faults in Block B is within N10°E–N20°E.

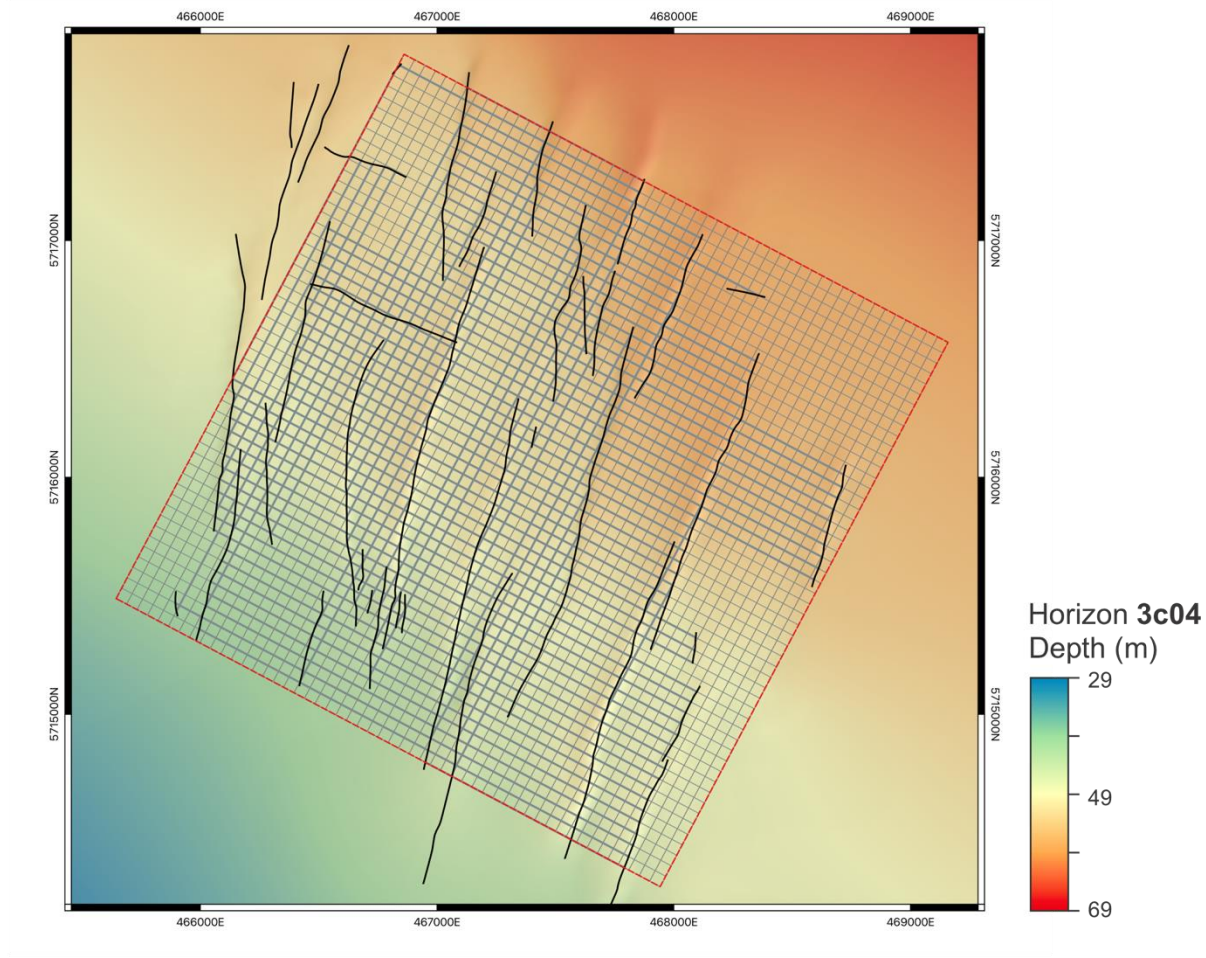

Figure 3.17. Scanlines set in Block B, with 50 m spacing parallel to block boundaries in NE and NW directions, to measure the fault spacing.

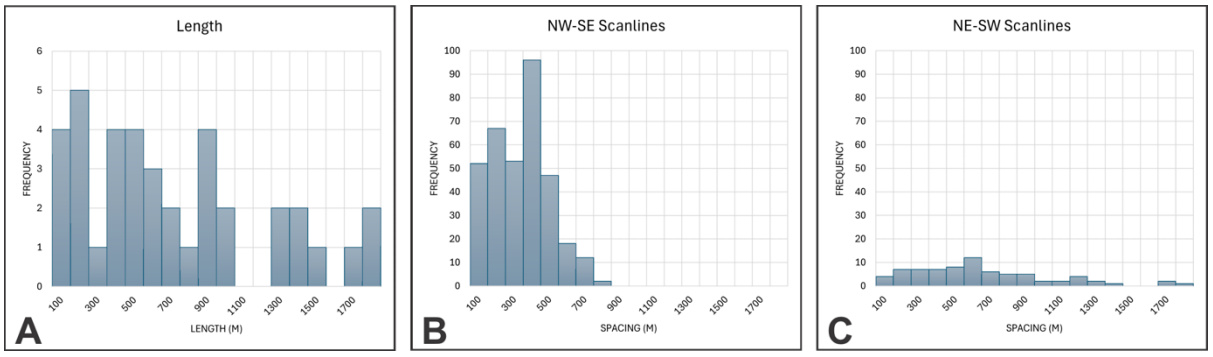

Figure 3.18. Histogram of the fault length (A) and the fault spacings in NW (B) and NE directions (C) of Block B. Fault length varies widely with the maximum length is >1.7km. The fault spacings in NW-SE directions, which almost normal to fault orientation, is mostly less than 500 m and peaks within 300–400 m.

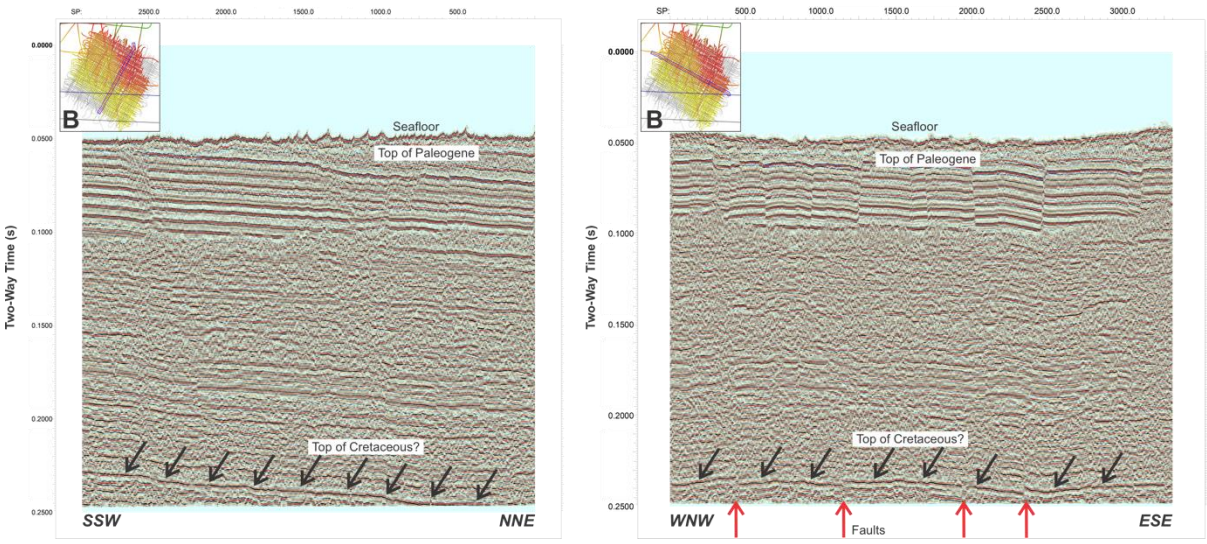

Figure 3.19. Sparker seismic section from Block B in NE-SW (A) and NW-SW (B) directions. The top of Cretaceous appears faulted following the faulting in the shallower depth.

3.4 Block C

Faulting in Block C, as interpreted from seismic profiles (**Figure 3.20**) and fault maps (**Figure 3.21** and **Figure 3.22**), shows moderately wide fault spacing, wider than in Block A but narrower than in Block B. The faults are predominantly oriented in a north-south direction and mostly dip toward the east. Major faulting occurs near the syncline structure, exhibiting displacements of up to 15 m. Fault density increases significantly in regions where the syncline is located. The fold axis are oblique to most fault orientations, indicating a different relationship between folds and faults compared to Block B.

A total of 154 faults have been modelled in Block C. Contour diagram reveals two prominent peaks in fault geometry, with frequencies of 30% and 18% (**Figure 3.23**). A rose diagram indicates that faults from these peaks share a similar north-south orientation (N350°E–N10°E) but exhibit opposing dip directions. A small proportion of faults (<20%) are oriented perpendicular in an east-west direction. For the first peak, faults exhibit a median strike of N1°E, ranging from N0°E to N10°E, with a median dip of 43° and a range between 40° and 55°. The second peak features faults with a median strike of N183°E, ranging from N180°E to N190°E, and a median dip of 54°, ranging between 40° and 55°.

Fault spacing in the northwest direction has a median of 162 m, with a range extending up to 1198 m (**Figure 3.24** and **Figure 3.25**). The histogram peaks at 175 m, with most faults spaced between 50 and 175 m. In the northeast direction, the median spacing is slightly narrower at 156 m, ranging up to 1195 m, with a histogram peak at 100 m and most spacing between 50 and 225 m. Fault lengths are more variable (**Figure 3.25**), with a median length of 223 m, ranging from 20 to 1646 m. The length distribution peaks between 25 and 275 m.

Sparker profiles reveal that deeper layers are also faulted (**Figure 3.26**). This indicates that faults in Block C extend from shallower to deeper layers and further confirm the occurrence of major faulting in this block.

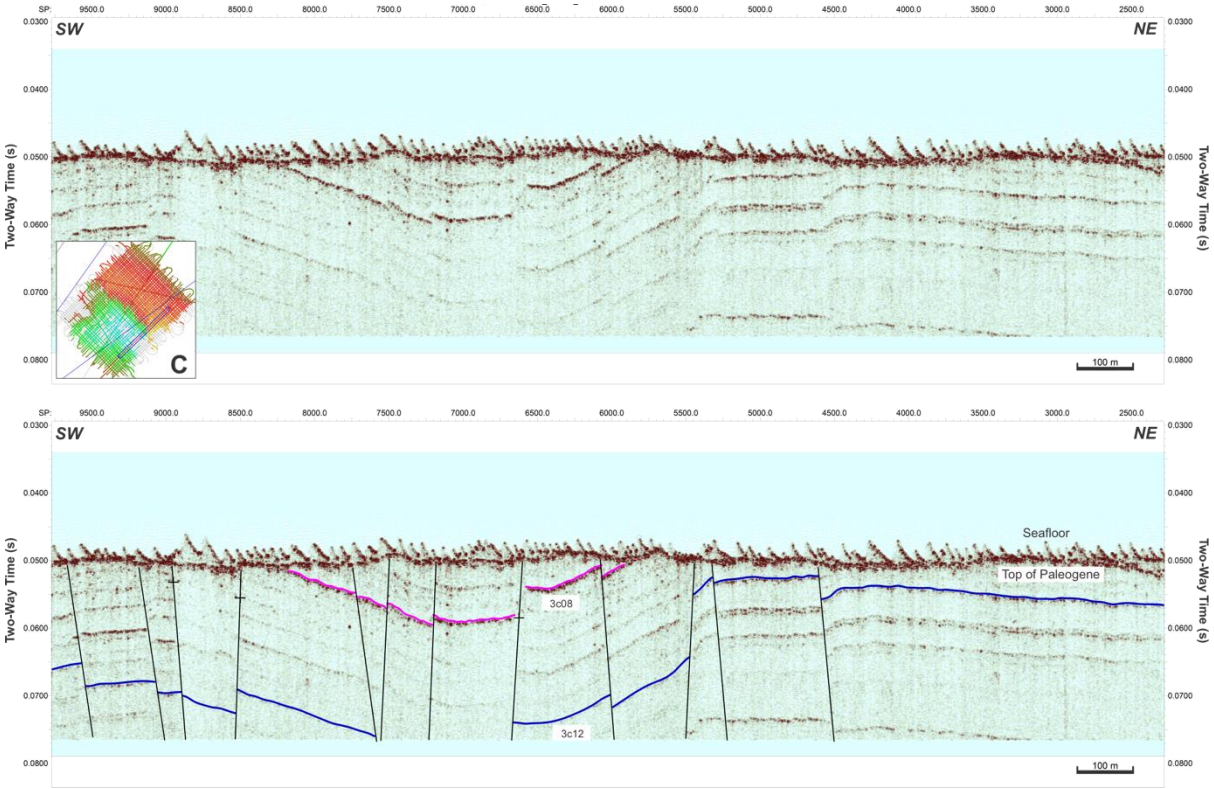

Figure 3.20. Seismic section (top) and seismic interpretation (bottom) from Block C, showing folding structure (anticline and syncline) and a fault with major displacement.

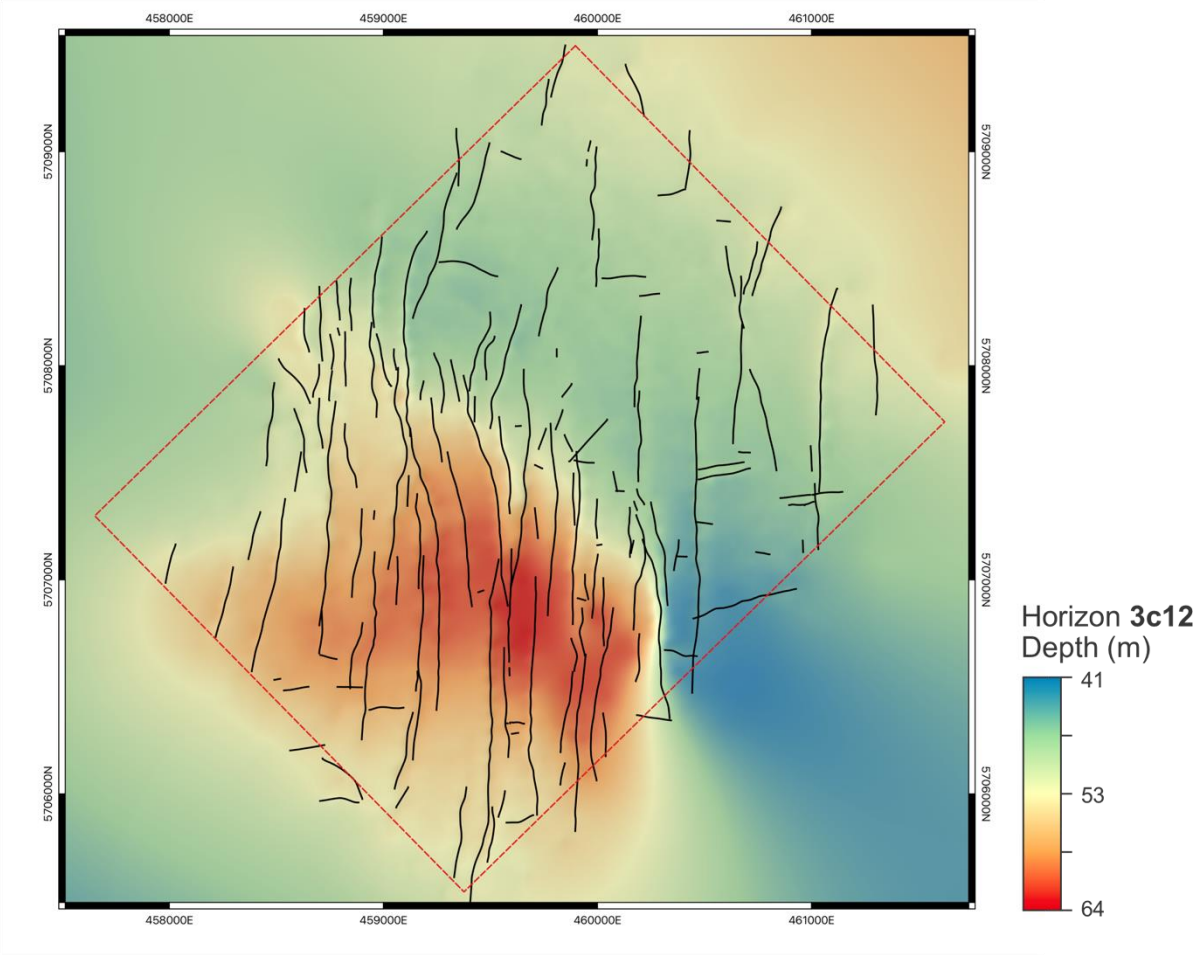

Figure 3.21. Distribution of faults in Block C, featuring the total number of 154 correlated and modelled faults within the block. Faults mainly oriented in N-S direction, narrowly spaced in the region where folding present.

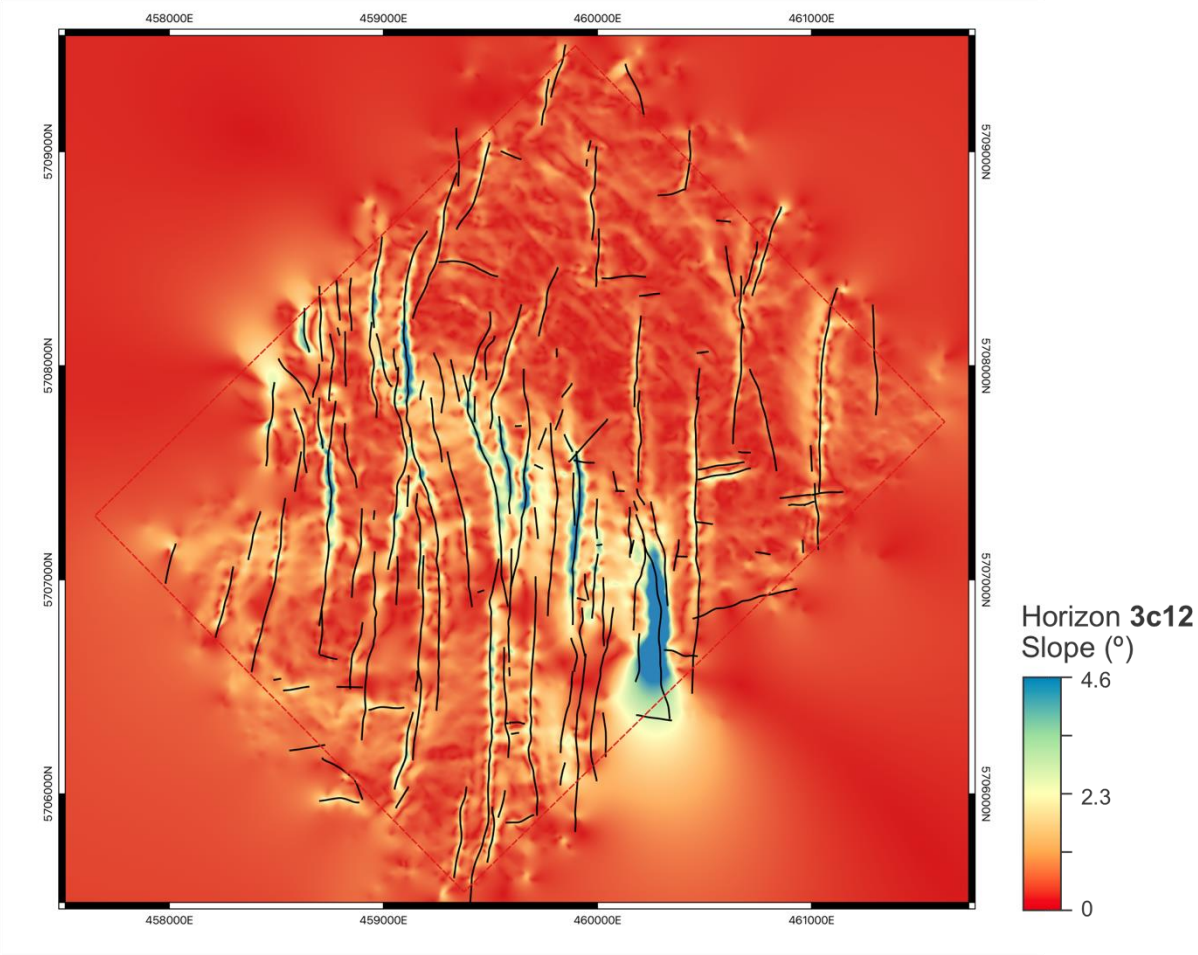

Figure 3.22. Slope map of the gridded Horizon 3c12 to confirm the location of faults in Block C

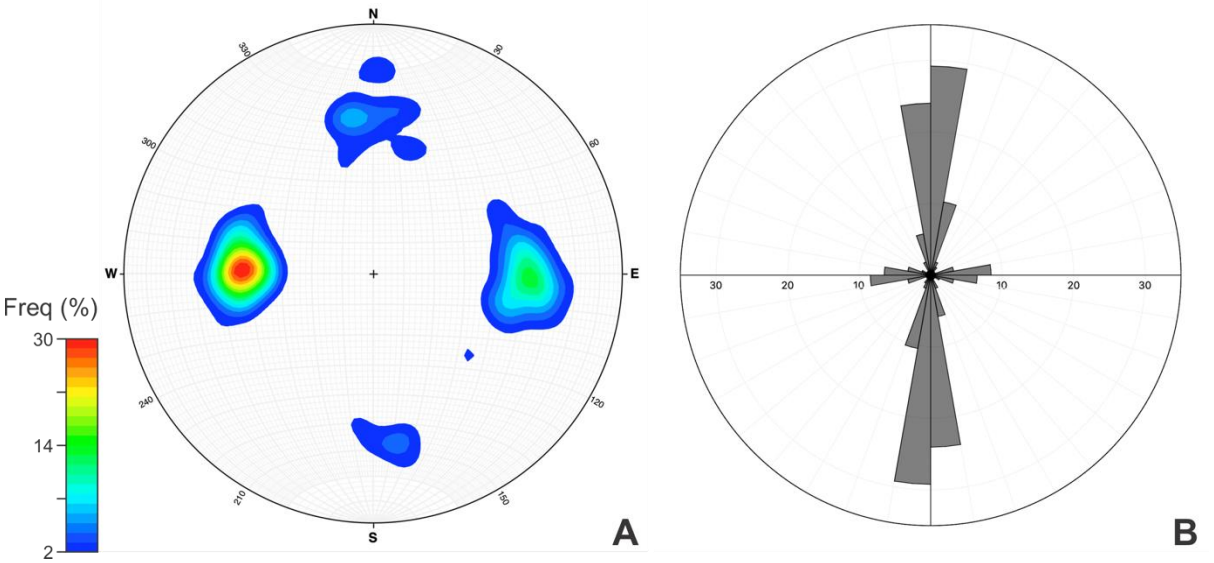

Figure 3.23. Analyses of fault geometry in Block C: (A) Contour diagram suggests that most faults oriented in similar direction but with opposing dip directions (N1°E/43° and N183°E/54°); (B) Rose diagram suggests the main orientations of faults in Block C is within N350°E-N10°E.

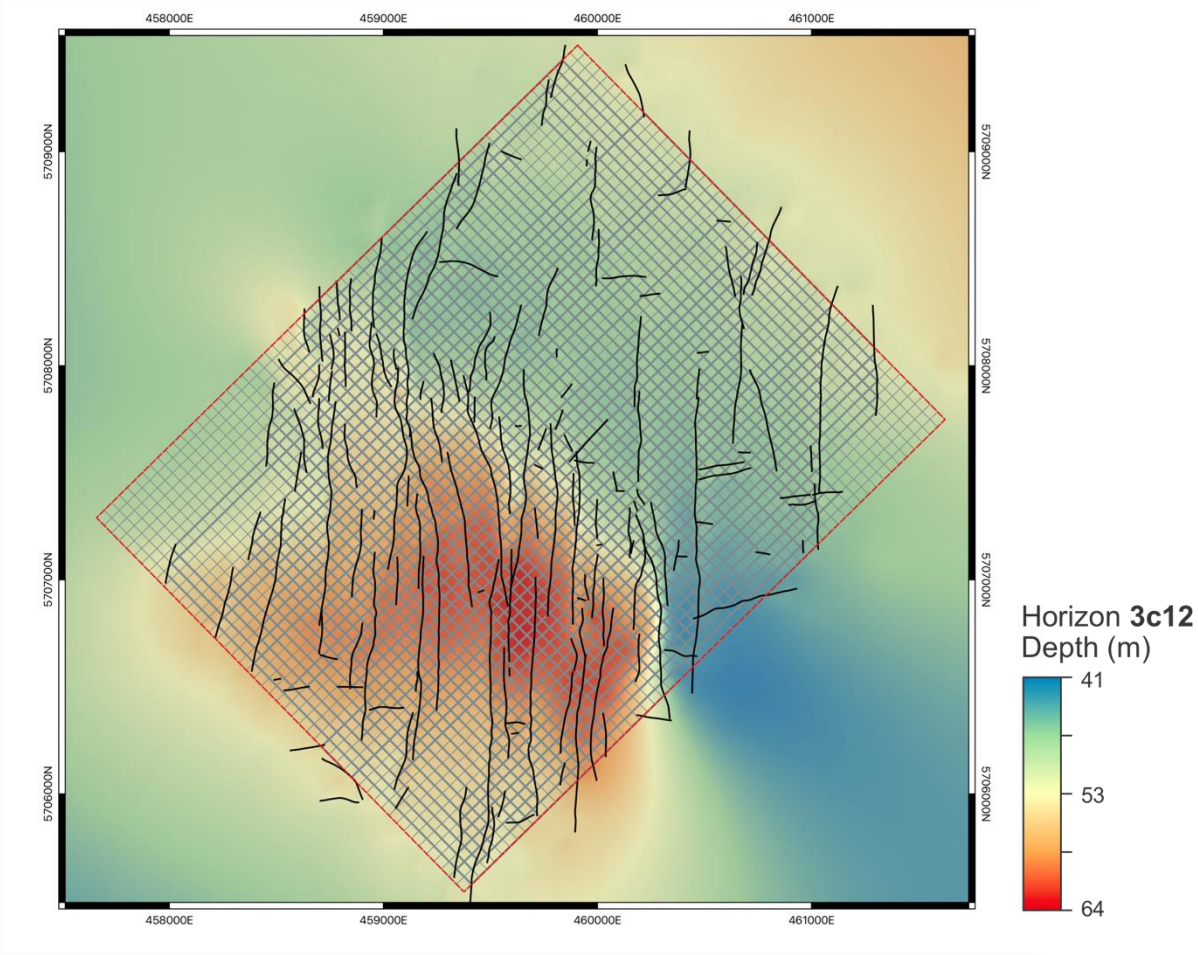

Figure 3.24. Scanlines set in Block C, with 50 m spacing parallel to block boundaries in NE and NW directions, to measure the fault spacing.

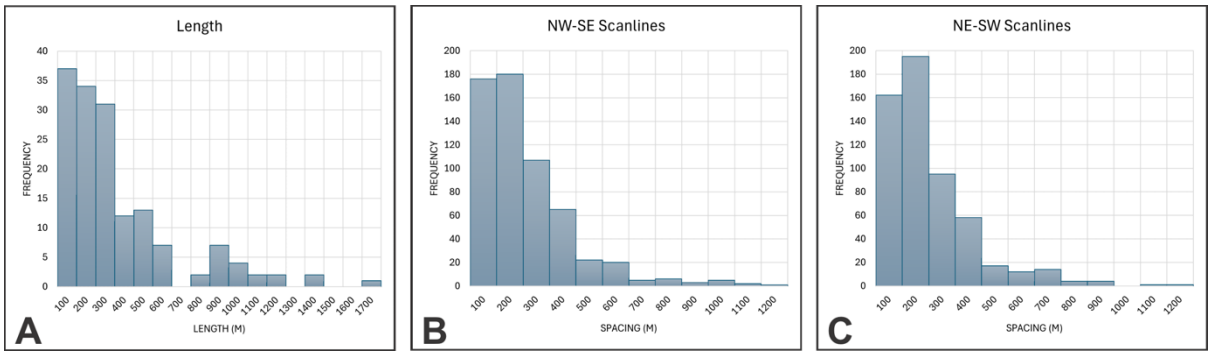

Figure 3.25. Histogram of the fault length (A) and the fault spacings in NW (B) and NE directions (C) of Block C. Fault length varies with the maximum length is >1.6 km. The fault spacings in both directions is generally less than 400m and peaks within 100–200m.

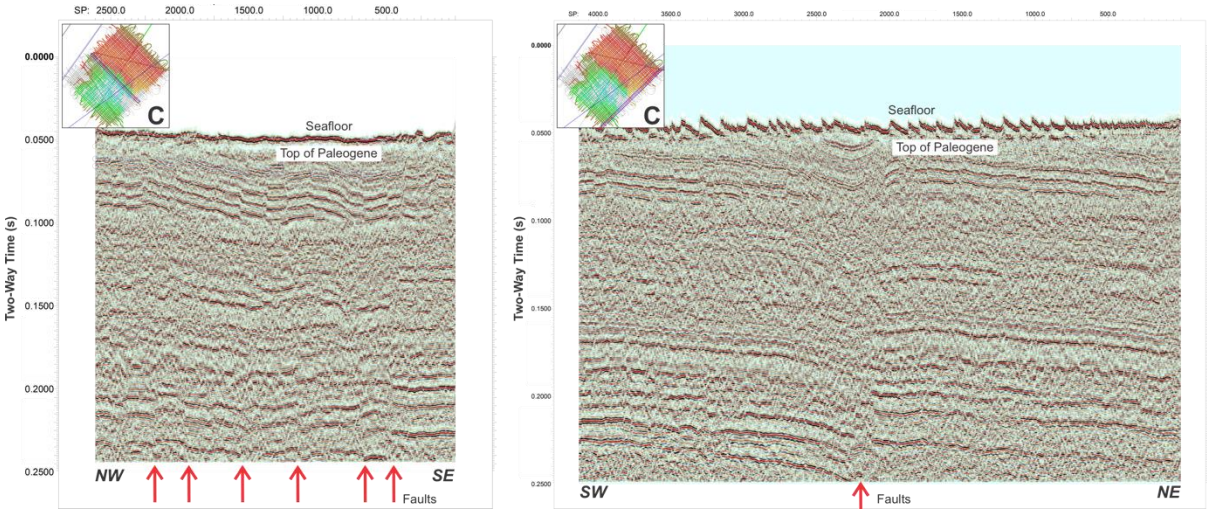

Figure 3.26. Sparker seismic section from Block C in NW-SE (A) and SW-NE (B) directions. Deeper layers appear to be faulted, continuing from the faulting in the shallower parts, especially the fault with major displacement.

3.5 Block D

Faulting in Block D is shown on seismic profiles in **Figure 3.27** and fault maps in **Figure 3.28** and **Figure 3.29**. The Quaternary sand deposit in this block is thicker, compared to other blocks. This thicker deposit makes it challenging to observe subsurface structures in some areas, resulting in a lack of interpreted horizons or faults in certain regions. The southwestern part of Block D features faults resembling those in Block A, with narrow spacing and predominantly south-dipping orientations. These faults feature horizons that are curved toward the fault planes, indicating presence of fault damage zone as also observed in Block A. They are relatively short in length and primarily oriented in an east-west direction. In contrast, the northeastern part of Block D has faults more similar to those in Blocks B and C, with wider spacing that makes general sedimentary structures more observable. Sedimentary layers in this region dip toward the northeast, and the faults here are longer, generally oriented in a northeast-southwest direction. The transition between these two fault groups is abrupt, forming a distinct boundary of strain partitioning between the two fault groups.

A total of 245 faults have been modelled in Block D. Statistical analysis in contour diagram reveals two main peaks in fault geometry, with frequencies of 28% and 12% (**Figure 3.30A**). These peaks share similar strikes but have opposing dip directions. The first peak is characterized by faults with a median strike of N85°E (range: N80°E–N90°E) and a median dip of 64° (range: 60°–70°). The second peak represents faults with a median strike of N262°E (range: N260°E–N270°E) and a median dip of 63° (range: 60°–70°). A rose diagram shows that east-west oriented faults (N80°E–N100°E) dominate at 58%, while NNE-SSW oriented faults (N10°E–N30°E) make up 9% (**Figure 3.30B**).

Fault spacing varies across directions (**Figure 3.31** and **Figure 3.32**). In the northwest direction, the median spacing is 112 m, ranging up to 796 m, with a peak at 75 m and most faults spaced between 25 and 125 m. In the northeast direction, spacing has a median of 119 m, ranging up to 921 m, with a histogram peak at 50 m and a majority spacing between 25 and 100 m. Fault lengths are relatively short, with a median of 96 m, ranging from 12 to 798 m (**Figure 3.32**). The length distribution peaks between 25 and 100 m, similar to Block A. However, longer faults, up to 800 m, are also prevalent. East-west oriented faults are shorter but more prevalent compared to

northeast-southwest faults, making the former group more dominant in both contour and rose diagrams.

When fault geometry was weighted by length, the dominance of fault orientations changed (**Figure 3.33**). In the contour diagram, the proportion of east-west oriented faults (N85°E/64°) increased from 28% to 40%. Additionally, the second peak shifted from faults with a similar strike but opposing dip to another fault set oriented at N301°E and dipping at 44°, with a frequency of 12%. On the rose diagram, east-west faults (N80°E–N110°E) decreased slightly in dominance from 58% to 52%, while northeast-southwest faults (N40°E–N50°E) increased from less than 5% to 9%, overtaking the dominance of NNE-SSW oriented faults. The changes observed in both the contour and rose diagrams after weighting strike and dip by fault length emphasise the importance of incorporating fault length into geometry analysis, particularly in areas where two fault sets coexist. This adjustment reveals the dominance of less prevalent but longer faults, which might otherwise be overshadowed by shorter, more numerous faults in the block.

Deeper Sparker profiles reveal differing fault characteristics in the northeastern and southwestern parts of Block D (**Figure 3.34**). In the northeastern region, where faults resemble those in Blocks B and C, faults propagate to deeper layers, potentially reaching the top of the Cretaceous. Meanwhile, in the southwestern region, where faults share characteristics with Block A, the top of the Cretaceous remains relatively flat. Despite this flatness, the general structures of overlying layers persist, dipping toward the northeast in the northern part of the block.

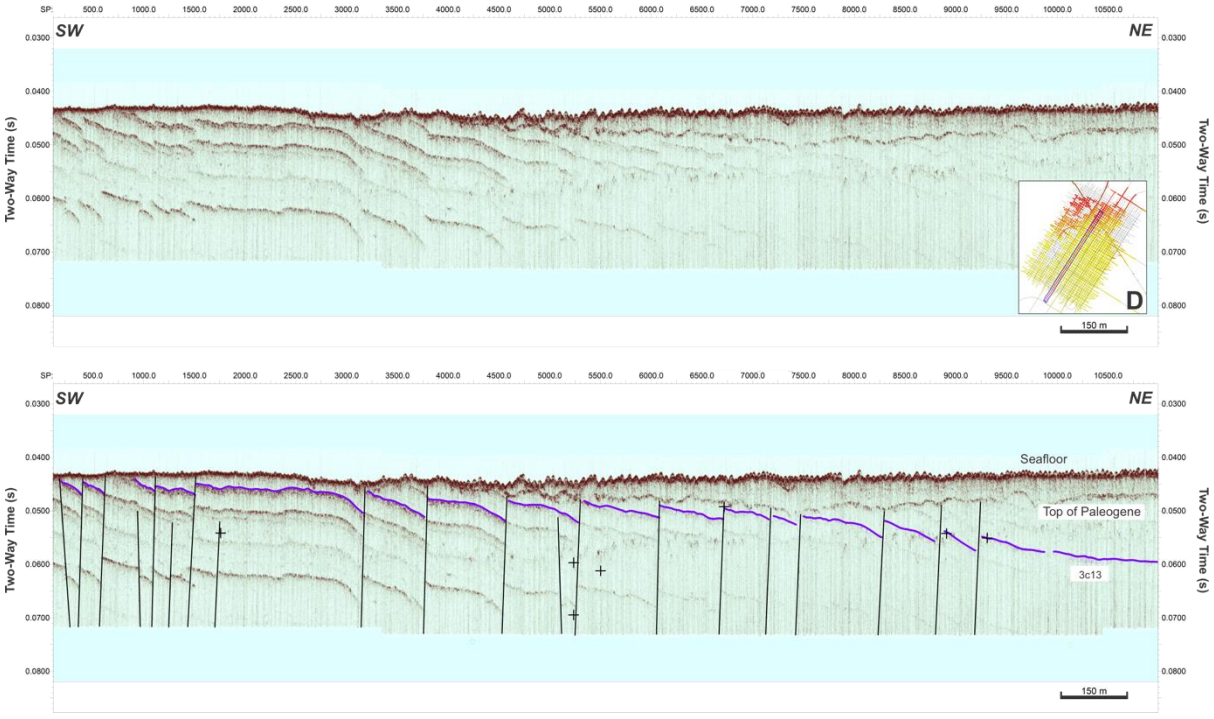

Figure 3.27. Seismic section (top) and seismic interpretation (bottom) from Block D, showing generally north dipping structure of the layers where fault spacing is narrower in the southern part of the block in comparison to its northern part.

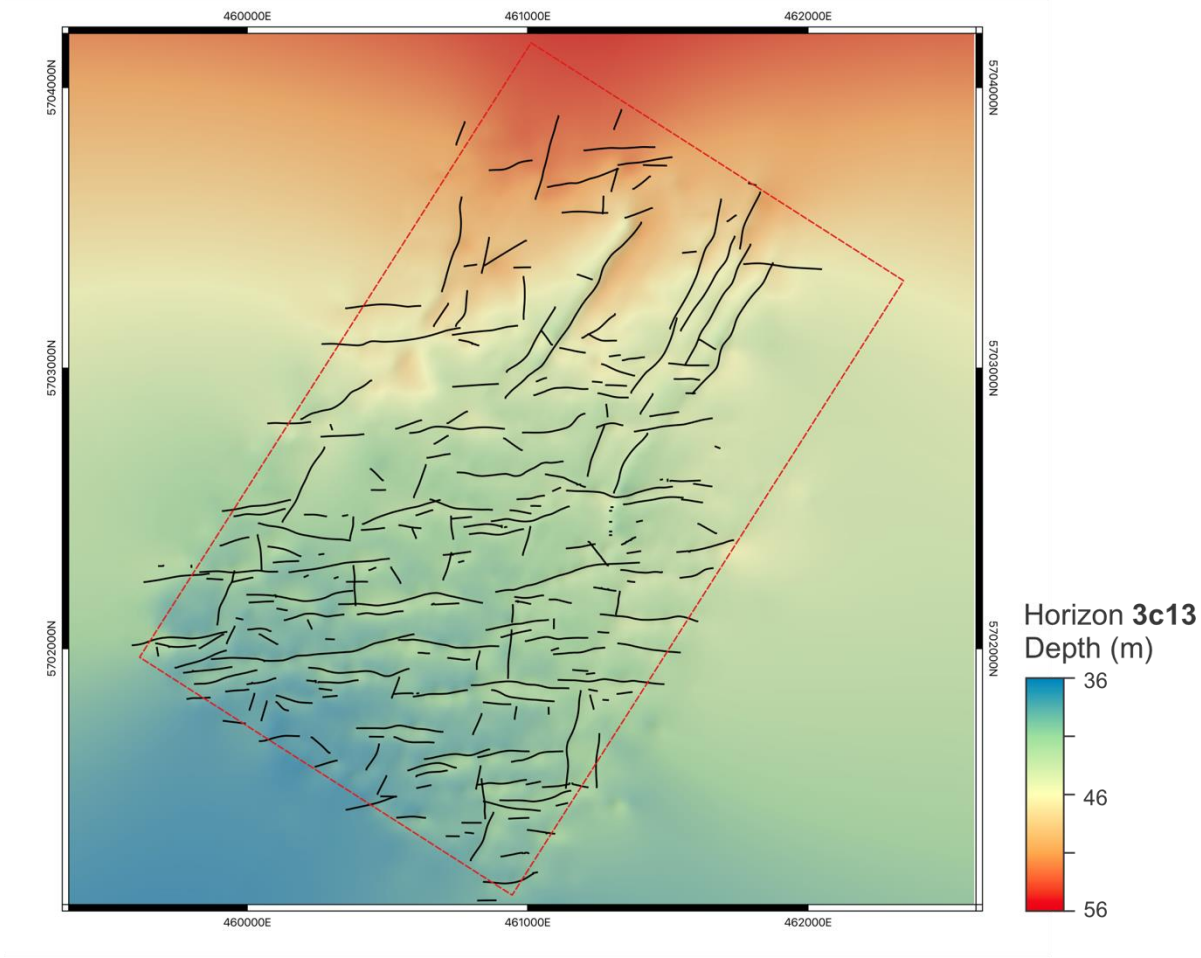

Figure 3.28. Distribution of faults in Block D, featuring the total number of 245 correlated and modelled faults within the block. Faults in the southern part show similarities with faults in Block A while faults in the northern part share similarities with faults in Block B and C.

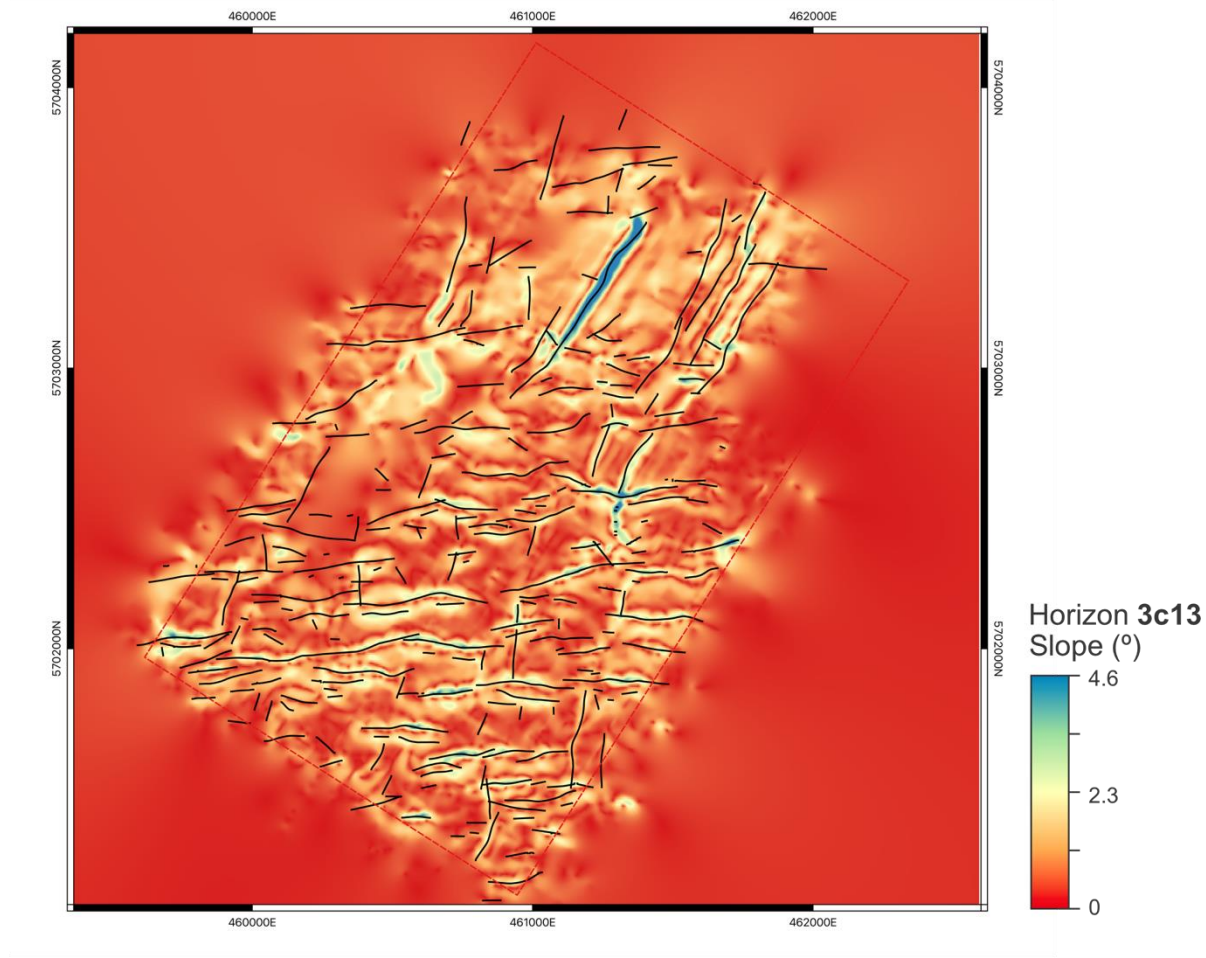

Figure 3.29. Slope map of the gridded Horizon 3c13, same key horizon with Block A, to confirm the location of faults in Block D.

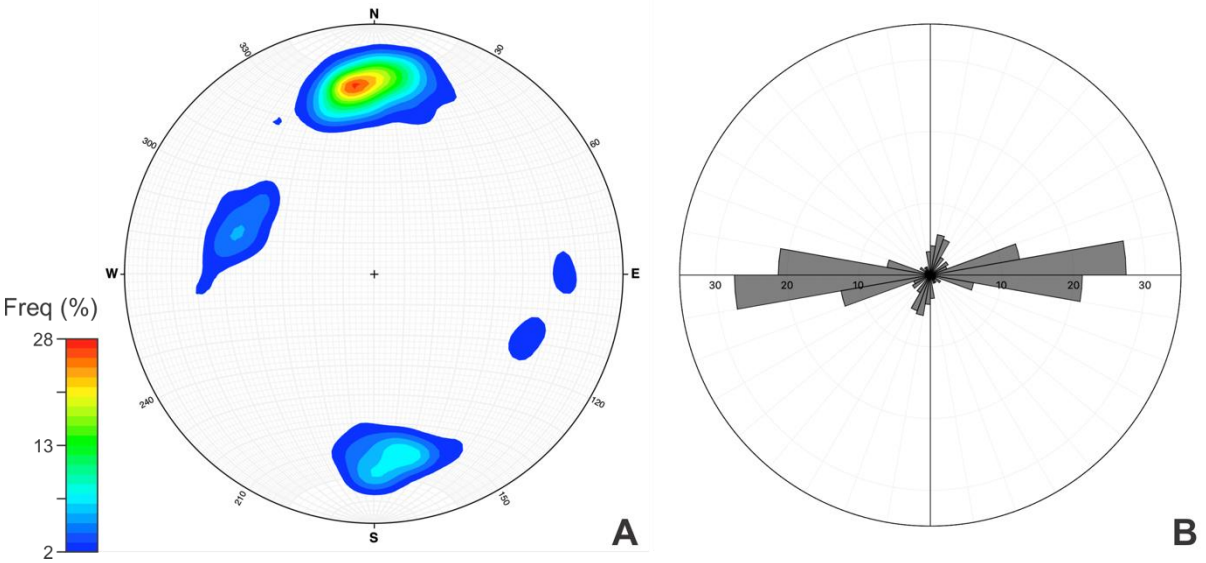

Figure 3.30. Analyses of fault geometry in Block D: (A) Contour diagram suggests that most faults oriented in E-W direction, similar to Block A (N85°E/64° and N262°E/63°); (B) Rose diagram suggests the main orientations of faults in Block D is within N80°E-N90°E.

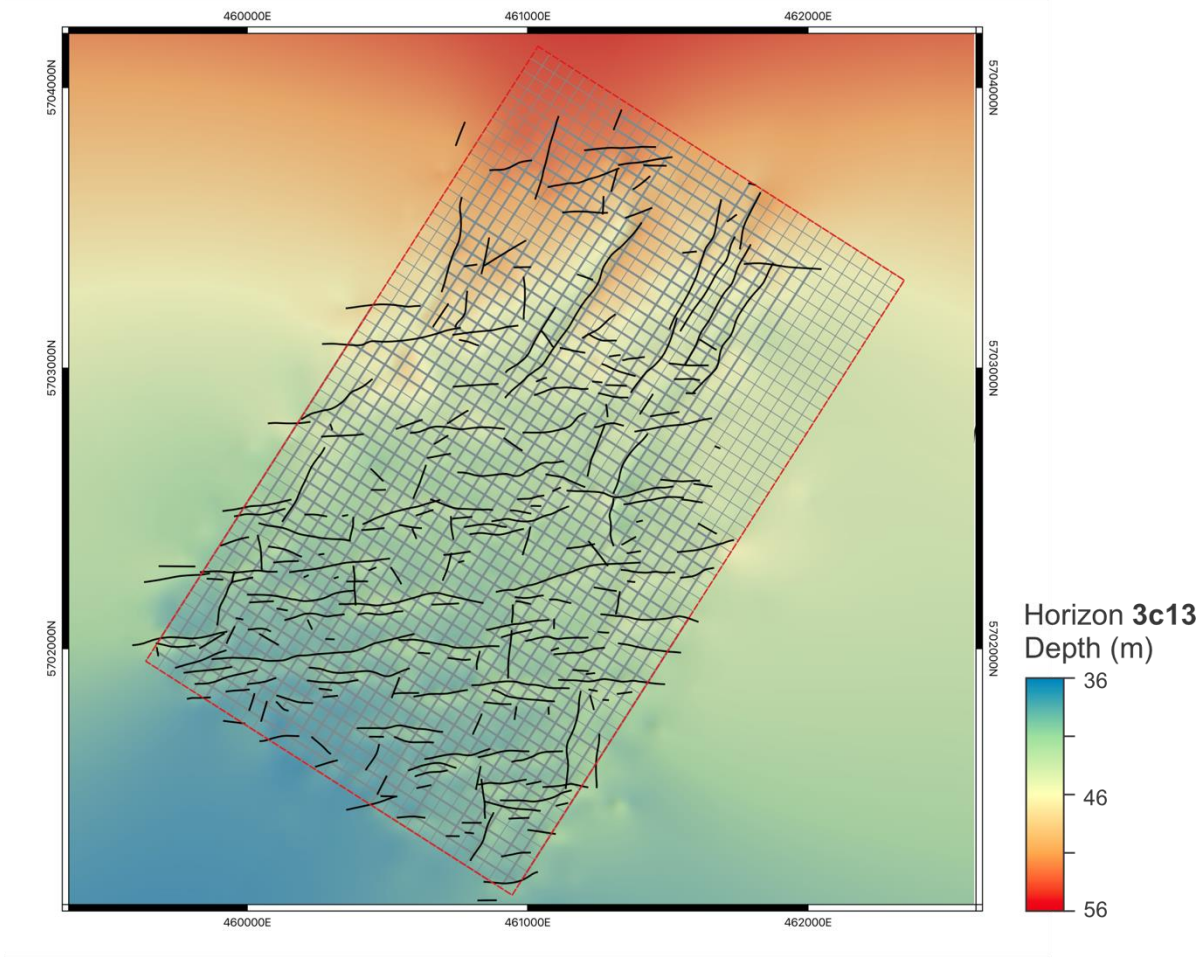

Figure 3.31. Scanlines set in Block D, with 50 m spacing parallel to block boundaries in NE and NW directions, to measure the fault spacing.

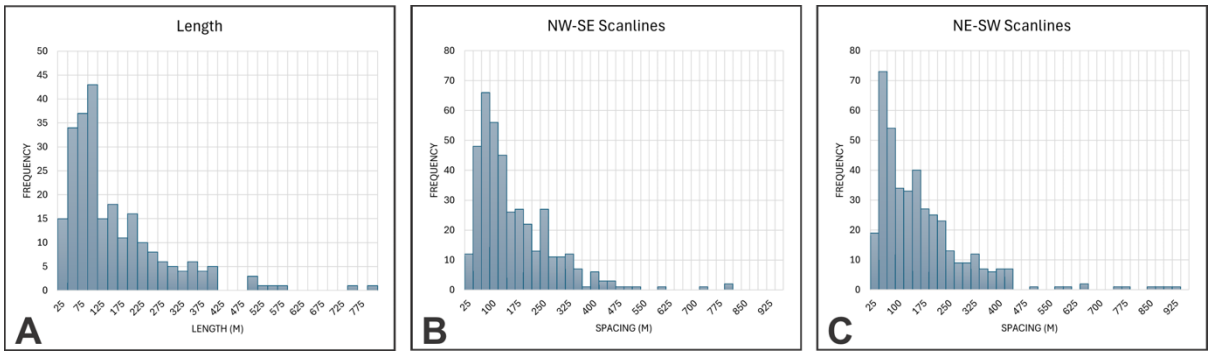

Figure 3.32. Histogram of the fault length (A) and the fault spacings in NW (B) and NE directions (C) of Block D. Fault lengths vary with the majority are less than 400 m, similar to Block A, but the maximum length extends up to 800 m, sharing similarities with Block B and C. Faults spacing are generally less than 150, but it can reach as far as 900 m.

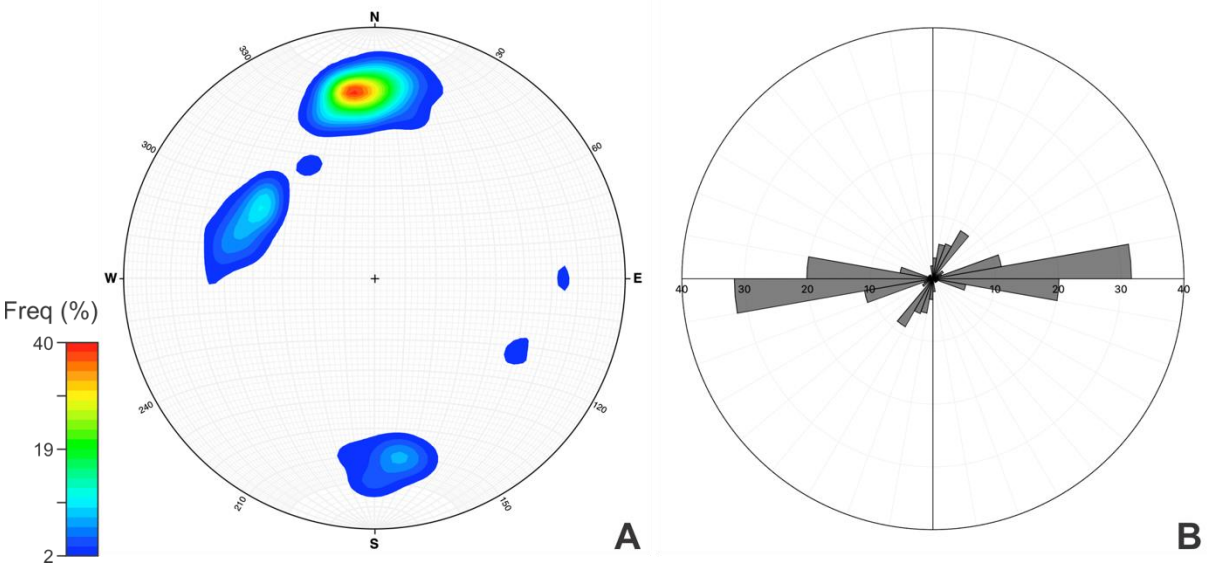

Figure 3.33. Analyses of fault geometry in Block D, weighted by fault length: (A) Contour diagram suggests a more significant percentage of NE-SW faults, similar orientation of faults in Block B and C; (B) Rose diagram also suggests more significant NE-SW faults in this block, although still less than E-W oriented faults.

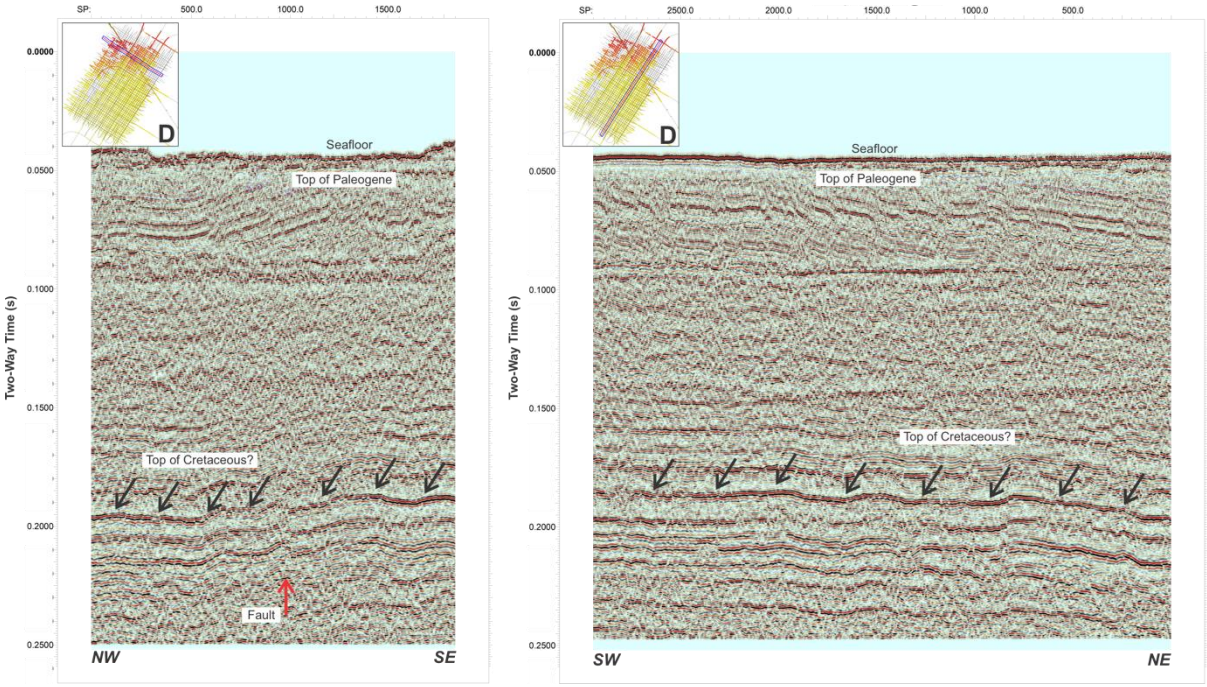

Figure 3.34. Sparker seismic section from Block D in NW-SE (A) and SW-NE (B) directions. Deeper layers appear to follow the general structure of the shallower layers. A major fault in the north cut through the deeper layers in the north while the southern part appears to be relatively flat.

4 Discussion

4.1 Faults

Fault mapping and seismic interpretation across the four Blocks reveal two well-defined fault groups that recur throughout the study area (**Figure 4.1**). One group comprises faults oriented in ENE–WSW, while the other is oriented in NNE–SSW. Although each block shows its

own local variations in fault patterns and deformation styles, these two orientations appear consistently, with distinct differences in dip angles, fault lengths, spacing, and depth of propagation.

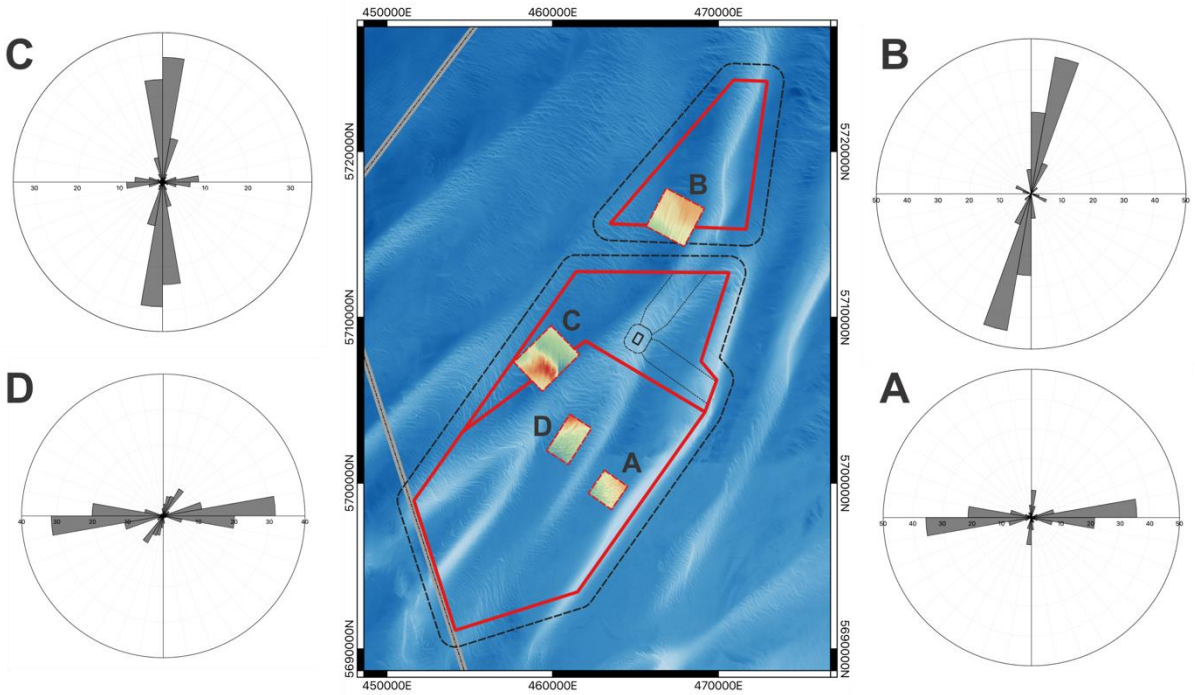

Figure 4.1. Compilation of structural distribution (rose diagrams) of the PEZ. Two main fault groups are identified based on their orientation: fault group 1 (ENE-WSW) prevalent in the northern PEZ while fault group 2 (NNE-SSW) prevalent in the southern PEZ.

The ENE–WSW-oriented group, observed most clearly in Block A and the southwestern portion of Block D, is generally characterised by steeper fault planes with dips commonly ranging between 60° and 70°. In Block A, for example, the median dip is around 64°. Faults in this set often show relatively short lengths, ranging mostly between 25 and 100 m, and are closely spaced. Typical median spacings of 65–79 m appear in Block A, with comparable intervals in the southwestern part of Block D. Seismic data in these areas suggest that ENE–WSW-oriented faults tend to be restricted to shallower horizons, as indicated by relatively flat deeper reflectors such as the top of the Cretaceous. The resulting fault patterns reflect localised deformation within the formation, with frequent minor splays and a high fault density that does not extend deeply into the deeper subsurface.

In contrast, the NNE–SSW oriented fault group, prominent in Blocks B and C as well as in the northeastern part of Block D, typically displays moderate dips of around 35°–55°. These faults can reach significantly greater lengths compared to the first fault set. In Block B, for instance, has a median length of 525 m and the longest fault reach 1.7 km length, while in the northeastern section of Block D, faults can exceed several hundred metres. Spacing is likewise broader, on the order of hundreds of m, as seen in Blocks B and C. Another key feature is that these faults frequently propagate into deeper stratigraphic layers, often reaching as deep as the top of the Cretaceous, as suggested by the Sparker seismic profiles. This deeper penetration, combined with longer fault traces and wider spacing, marks the NNE–SSW group as, perhaps, a more regionally extensive style of faulting.

The comparison between the two fault groups observed within the PEZ and their key characteristics are summarised in **Table 4.1** below.

Table 4.1 Summary of the two main fault groups (ENE–WSW and NNE–SSW) and their key characteristics (orientation, dip, length, spacing, and depth of propagation) within the PEZ.

Attributes	Fault Group 1: ENE-WSW	Fault Group 2: NNE-SSW
Strike	ENE–WSW (e.g., N80°E–N100°E and N260°E–N290°E)	NNE–SSW (e.g., N10°E–N20°E or N350°E–N10°E)
Dip (°)	~60–70°, with medians ~64°	~35–55°, with medians ~40–45°
Length (m)	Relatively short; common peak around 25–100 m; Median often <100–120 m	Relatively onger; can exceed several hundred metres; Medians commonly range from 200–500+ m
Spacing (m)	Narrower spacing (tens of metres); median often 50–100 m	Broader spacing (hundreds of metres); medians can reach 200–300+ m
Depth of Propagation	Often confined to shallower horizons; deeper layers relatively unaffected	Extends to deeper stratigraphic levels, sometimes reaching top of Cretaceous
Locations	Most prominent in Block A and southwestern Block D	Most prominent in Block B, Block C, and northeastern Block D

Across the PEZ, normal faults dominate the deformation style, as evidenced by consistently displaced horizons on seismic profiles and fault maps. In most cases, fault displacement increases with depth, but this observation, perhaps, is affected by the limited depth of the penetration where deeper part of the faults can't be observed. Moreover, distinct variation is also observed in several places. Some faults show a distinct decrease in displacement with depth, ultimately terminating before reaching deeper horizons, leaving intact horizons at those lower levels (**Figure 4.2**). In certain instances, minor faults display maximum displacement at mid-depth, between shallower and deeper fault tips, consistent with the concept of intra-formational faulting. Another observed structural feature in some instances of these normal faults is the presence of fault splays, where secondary faults branch off from a main fault (**Figure 4.3**). These splays terminate on the primary fault plane in an antithetic arrangement, where these secondary faults dipping in the opposite direction to the main fault.

Although most faults display a relatively narrow, well-defined fault plane, Block B stands out for exhibiting wider fault zones with a degree of horizontal separation. Instead of a sharply defined fault plane that cleanly displaces horizons, the deformation is spread across a broader band, creating the appearance of a "fault zone" (**Figure 4.4**). This style may reflect particular variations in this block, for instance, the physical property of the clay or other parameters that may cause strain to be distributed rather than localised on a fault plane.

Collectively, these observations highlight that while normal faulting is the predominant deformation style in the region, specific variations in various scale, such as displacement patterns, the presence of fault splays, and fault zone thickness, demonstrate the diversity of structural and deformation styles.

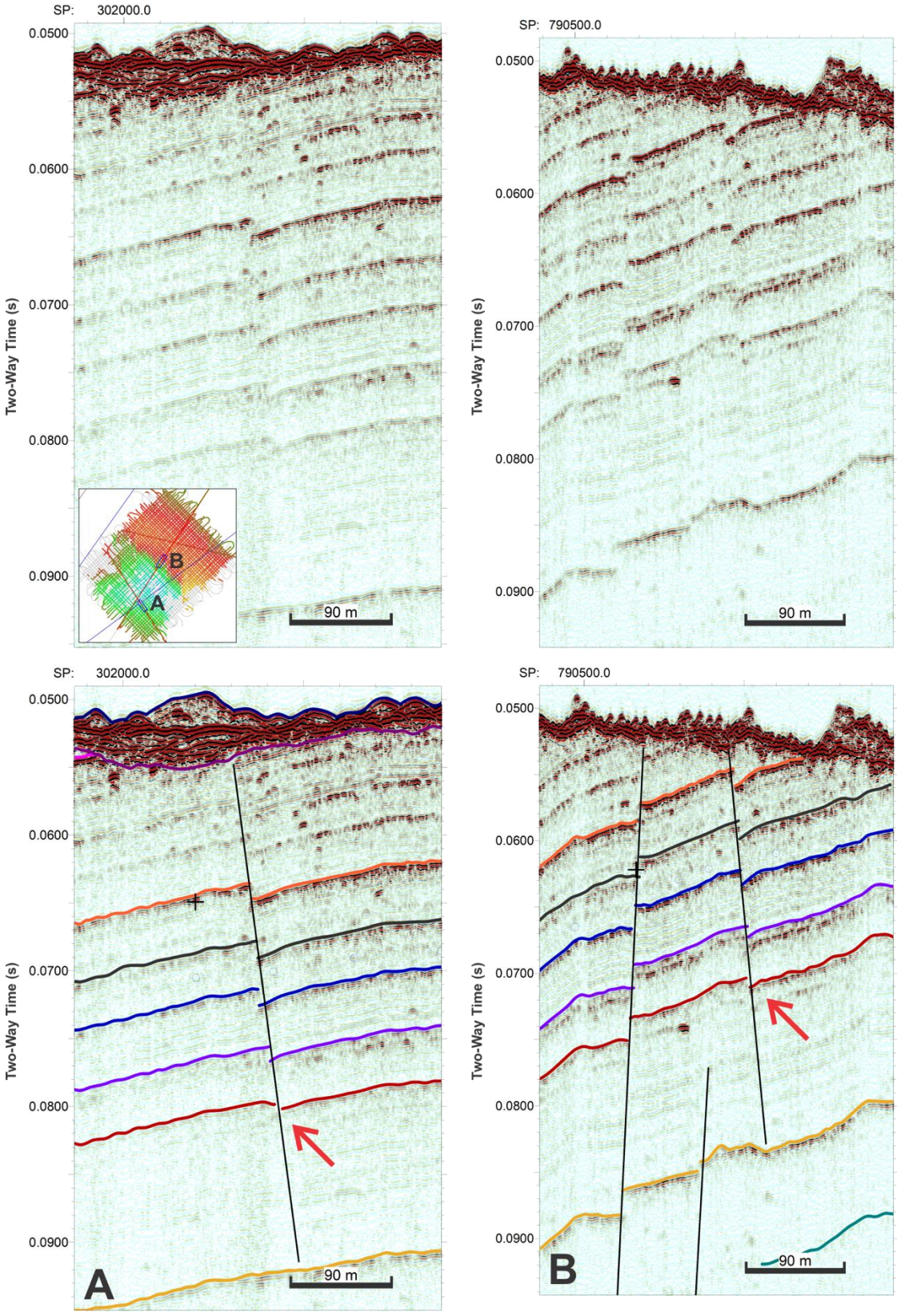

Figure 4.2. Observed fault termination at the deeper part of fault plane with decreasing vertical displacement (throw) along the fault plane.

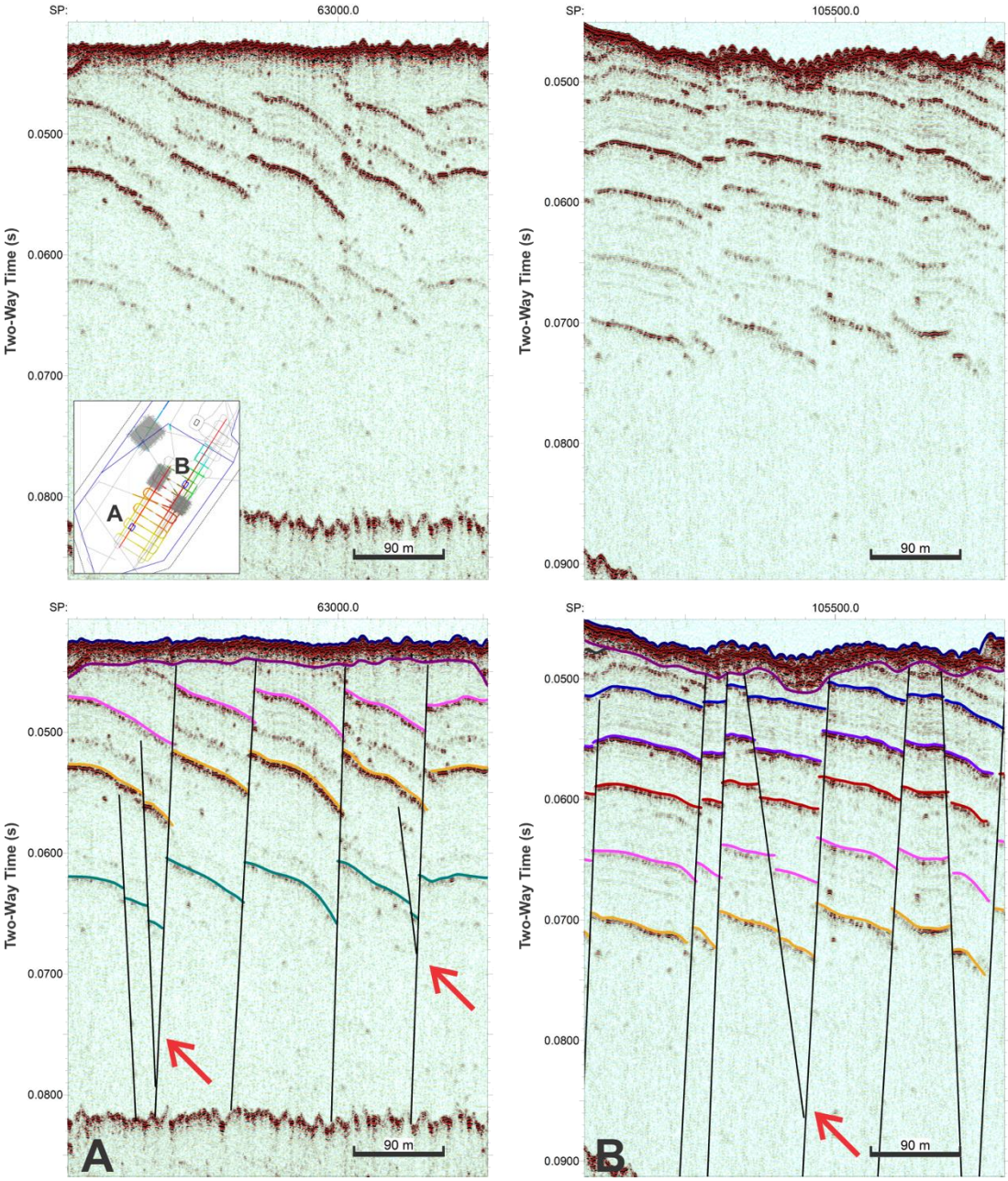

Figure 4.3. Examples of fault splays observed in various locations within the PEZ (pointed by red arrows), showing secondary fault growth from the main fault plane.

4.2 Folds

The wider fault spacing in Blocks B and C allows for clearer observation of folding structures, which often appear as broad, gently dipping limbs on seismic profiles (**Figure 4.4** and **Figure 4.5**). In Block B, for instance, folds generally exhibit gentle geometries with axes closely aligned to the primary NNE–SSW fault orientation, suggesting a possible genetic link between the two. However, in Block C, fold axes are oblique to the major NNE–SSW oriented fault set, creating a more complex relationship between folding and faulting. A pronounced syncline, whose axis is not parallel to the regional fault strike, exhibits an increase in fault density. Nonetheless, the precise mechanism governing how folding and faulting interact remains unclear and requires further investigation.

Additionally, the deeper fault propagation in Blocks B and C where deeper layers also exhibit a general folding structure, perhaps, suggest at a temporal distinction between folding and faulting. The observation that major faults (with displacements reaching ~15 m) cut across pre-existing folds (**Figure 3.20**) supports the idea that folding likely predated the later phase of faulting. Given that Blocks B and C lie relatively close to the Noordhinder Deformation Zone[10] (**Figure 1.2**), it is plausible that the folds in this region could be related to deformation events recorded farther north. In this scenario, regional folding may have occurred first, followed by the faulting episodes responsible for the larger displacements seen in the seismic profiles.

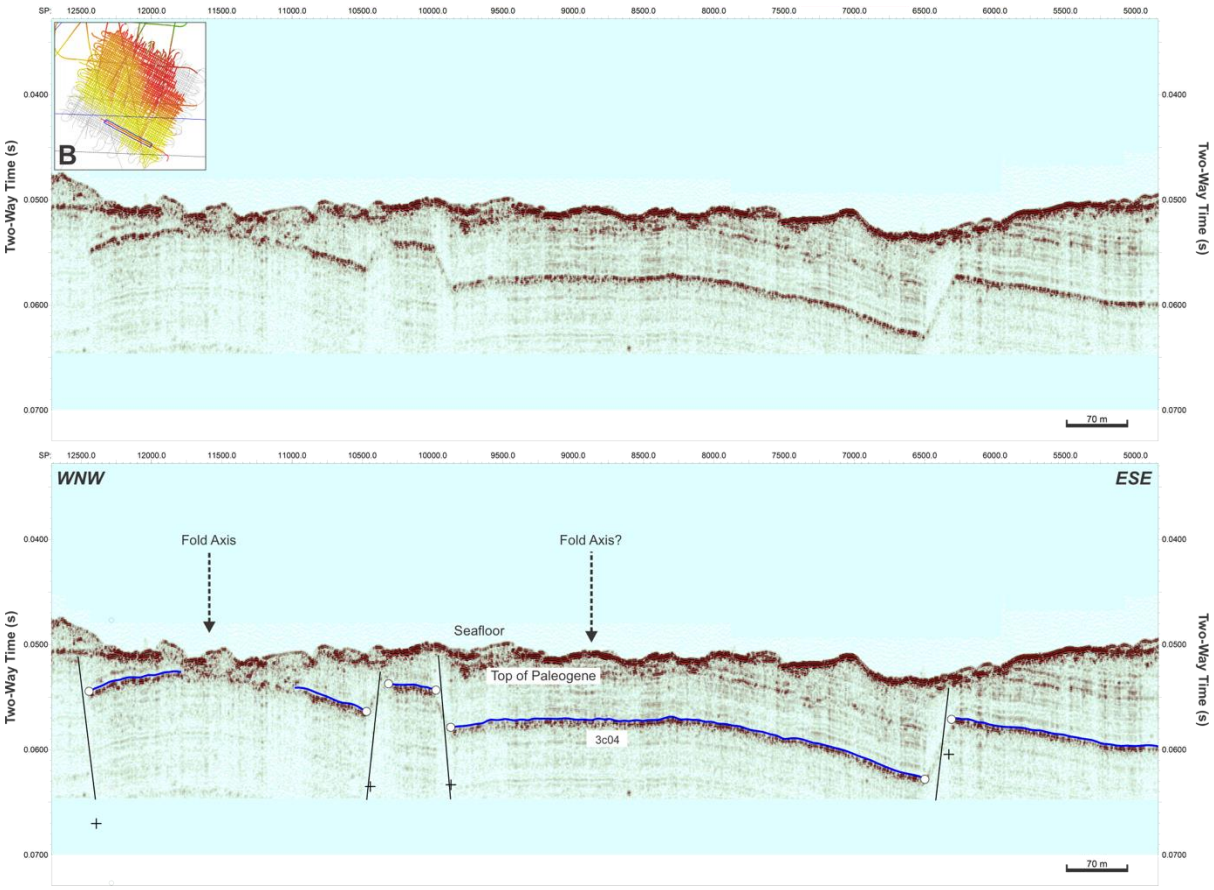

Figure 4.4. Folding in Block B where fold axes are parallel to the orientations of faults. Fault thickness in this block also appears to be wider where horizon tips leave wider gaps away from the fault plane (horizon tips indicated by white circles).

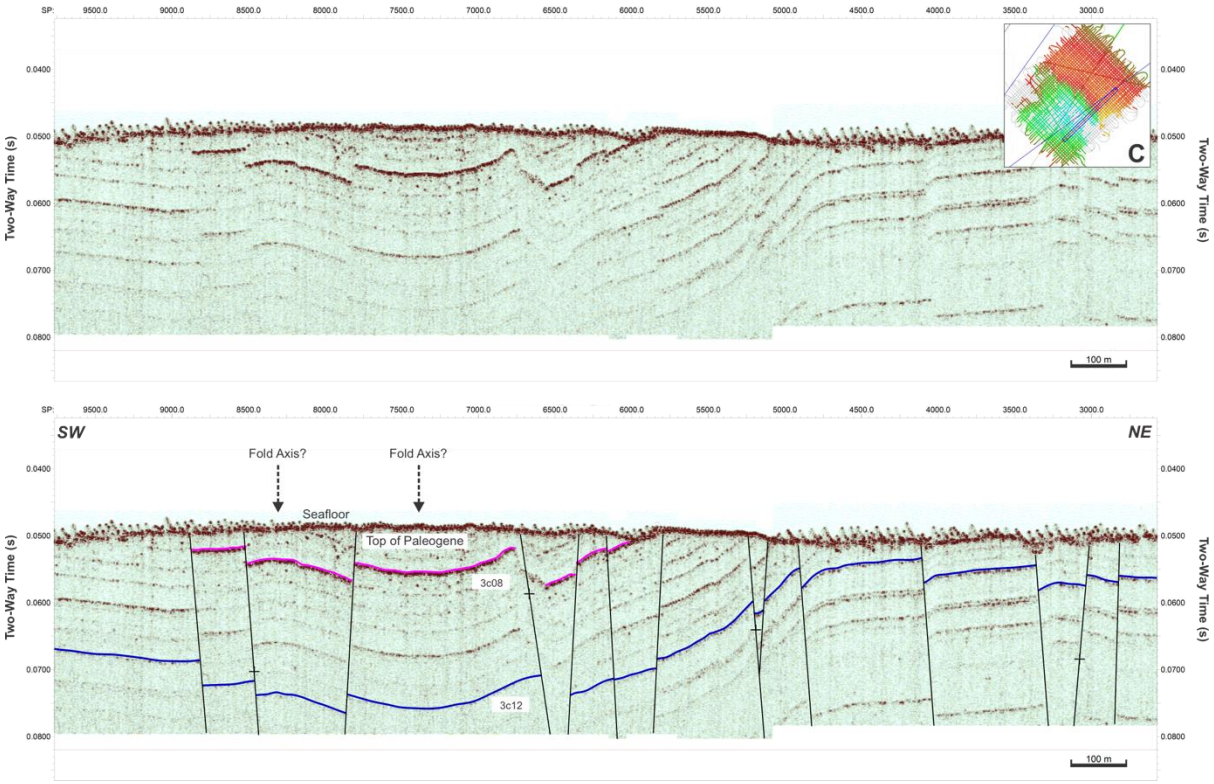

Figure 4.5. Faulted folding structure in Block C where fold axes are oblique to the general orientation of the faults.

4.3 Implications

The observed fault orientations in the Kortrijk Clay Formation present a fascinating contrast to what would be expected from a polygonal fault system. Typically, polygonal faults display a more variable set of orientations, reflecting the diagenetic-related deformation of the fine-grained sediments during compaction. However, in this instance, the faults appear to exhibit predominant orientations, implying that regional tectonics may have exerted a stronger influence on their development and distribution than previously thought. It is possible that externally imposed stress fields, rather than purely local sedimentary processes, drove fault initiation and propagation within this dense clay formation. At the same time, key characteristics of polygonal fault systems, such as the way certain faults terminate with decreasing displacement, suggest that intra-formational deformation processes were still in play. Although only observed in limited number of faults, this decreases in displacement toward deeper fault tip aligns with polygonal fault models.

These observations raise important questions about the timing and mechanics of faulting within the formation. Why do we see distinct fault sets trending ENE–WSW and NNE–SSW? Did they propagate simultaneously or in discrete stages influenced by changing stress fields, if any? And what did control the partitioning and style of faulting in the Kortrijk Clay Formation? Addressing these uncertainties will require further investigation that will be carried on in the next stage of this Clay Tectonics project.

The identification of predominantly oriented faults within the PEZ provides a valuable guidance for wind farm planning and infrastructure development. Rather than having to contend with the highly variable, random orientations typical of a polygonal fault system, developers can focus on a more predictable fault pattern. This increased predictability aids in optimising wind

turbine placement, foundation design, and cable routing by reducing geological uncertainties and enabling more effective risk mitigation measures.

However, the observed fault partitioning between the southern (ENE–WSW oriented faults) and northern (NNE–SSW oriented faults) parts of the PEZ highlights the need for region-specific planning strategies. Varying fault trends can influence the mechanical behaviour of the subsurface, potentially affecting foundation stability and the long-term performance of wind turbines. Interaction between the stress vector coming from the wind in similar direction across the surface and discontinuity orientation from both fault groups in the subsurface should be considered. Understanding these distinctions is crucial for tailoring construction techniques, planning, and development of wind farm to the specific geological conditions for each part of the PEZ.

5 Conclusion

Our study on the subsurface structure within the PEZ has revealed notable changes in structural styles across the area. Two distinct groups of faults have been identified. The first group is oriented in ENE-WSW direction (i.e., N80°E–N100°E and N260°E–N290°E), characterised by relatively short lengths with a common peak between 25–100 m and a median length of less than 100–120 m. These faults exhibit steeper dips, often ranging 60°–70°, and are generally confined to shallower horizons, leaving deeper layers relatively unaffected. In contrast, the second group of faults is oriented in NNE-SSW direction (i.e., N10°E–N20°E or N350°E–N10°E). These faults are significantly longer, often exceeding several hundred metres, with median lengths commonly ranging from 200–500+ m. They typically display shallower dips, often between 35° and 55°, and extend deeper, possibly reaching the top of the Cretaceous. These changes in structural style are particularly evident in Block D, located at the centre of the PEZ, where transition between the fault groups appears abruptly.

These findings carry important implications for both the origin of these faults and practical applications. The presence of predominant fault orientations appears to contradict the concept of random fault orientations expected in polygonal fault systems in clay formations. However, the observed decrease in displacement with depth in some faults still aligns with certain aspects of intra-formational faulting. These findings highlight a need for further investigation into control of fault development in the next stage of this Clay Tectonics project. From a practical standpoint, particularly for wind farm planning and development, this finding in fault orientation underscores a better predictability in fault geometry and distribution and the importance of site-specific design approaches. Clay tectonic features may need to be considered as a factor during the micro-siting of wind turbines. By tailoring projects to the specific structural style, stakeholders can better manage subsurface uncertainties and optimise the planning and efficiency of wind farm development.

Acknowledgements

We are thankful to our collaborators at Flanders Marine Institute (VLIZ) and Vrije Universiteit Brussel (VUB). We are also grateful to the crew of RV Belgica and RV Simon Stevin for their assistance during data acquisition. Clay Tectonics project is funded by the Blue Cluster of the Flanders Innovation and Entrepreneurship (VLAIO).

References

1 Velenturf, A. P. M. *et al*. Geoscience Solutions for Sustainable Offshore Wind Development. *Earth Science, Systems and Society* **1** (2021). https://doi.org/10.3389/esss.2021.10042

2 Lee, K.-H. *et al*. Numerical optimization of site selection for offshore wind turbine installation using genetic algorithm. *Current Applied Physics* **10**, S302-S306 (2010). https://doi.org/10.1016/j.cap.2009.11.031

3 Shankar Verma, A., Jiang, Z., Ren, Z., Hu, W. & Teuwen, J. J. E. Effects of Onshore and Offshore Environmental Parameters on the Leading Edge Erosion of Wind Turbine Blades: A Comparative Study. *Journal of Offshore Mechanics and Arctic Engineering* **143**, 1-31 (2021). https://doi.org/10.1115/1.4049248

4 Nielsen, J. J. & Sørensen, J. D. On risk-based operation and maintenance of offshore wind turbine components. *Reliability Engineering & System Safety* **96**, 218-229 (2011). https://doi.org/10.1016/j.ress.2010.07.007

5 Martin, R., Lazakis, I., Barbouchi, S. & Johanning, L. Sensitivity analysis of offshore wind farm operation and maintenance cost and availability. *Renewable Energy* **85**, 1226-1236 (2016). https://doi.org/10.1016/j.renene.2015.07.078

6 Jensen, P. D., Purnell, P. & Velenturf, A. P. M. Highlighting the need to embed circular economy in low carbon infrastructure decommissioning: The case of offshore wind. *Sustainable Production and Consumption* **24**, 266-280 (2020). https://doi.org/10.1016/j.spc.2020.07.012

7 Monrigal, O., De Jong, I. & Duarte, H. An ultra-high-resolution 3D marine seismic system for detailed site investigation. *Near Surface Geophysics* **15**, 335-345 (2017). https://doi.org/10.3997/1873-0604.2017025

8 Vardy, M. E. *et al*. State-of-the-art remote characterization of shallow marine sediments: the road to a fully integrated solution. *Near Surface Geophysics* **15**, 387-402 (2017). https://doi.org/10.3997/1873-0604.2017024

9 Prins, L. T. & Andresen, K. J. A geotechnical stratigraphy for the shallow subsurface in the Southern Central Graben, North Sea. *Engineering Geology* **286**, 106089 (2021). https://doi.org/10.1016/j.enggeo.2021.106089

10 Bot, S. L. *et al*. Geological characteristics and geotechnical properties of Eocene and Quaternary deposits on the Belgian continental shelf: synthesis in the context of offshore wind farming. *Netherlands Journal of Geosciences* **84**, 147-160 (2005). https://doi.org/10.1017/s0016774600023027

11 Henriet, J. P., de Batist, M. & Verschuren, M. in *Generation, accumulation, and production of Europe's hydrocarbons* (ed A. M. Spencer) 217-227 (Oxford University Press, 1991).

12 Clerq, M. d. *Drowned landscapes of the Belgian Continental Shelf: Implications for northwest European landscape evolution and preservation potential for submerged heritage* PhD thesis, Ghent University, (2018).

13 Steurbaut, E. & King, C. The composite Kortrijk section (W Belgium): a key reference for mid-Ypresian (Early Eocene) stratigraphy in the southern North Sea Basin. *Geologica Belgica* **20**, 125-159 (2017). https://doi.org/10.20341/gb.2017.008

14 Lonergan, L., Cartwright, J. & Jolly, R. The geometry of polygonal fault systems in Tertiary mudrocks of the North Sea. *Journal of Structural Geology* **20**, 529-548 (1998). https://doi.org/10.1016/s0191-8141(97)00113-2

15 De Batist, M., De Bruyne, H., Henriet, J. P. & Mostaert, F. in *The quaternary and tertiary geology of the southern Bight, North Sea* (eds J. P. Henriet & G. De Moor) Ch. 8, 75-88 (Ministry of Economic Affairs, Belgian Geological Survey, 1989).

16 Cartwright, J. Diagenetically induced shear failure of fine-grained sediments and the development of polygonal fault systems. *Marine and Petroleum Geology* **28**, 1593-1610 (2011). https://doi.org/10.1016/j.marpetgeo.2011.06.004

17 Moore, J. C., Taira, A., Klaus, A., Becker, L. & Boeckel, B. Proceedings of the Ocean Drilling Programme, Initial Reports, 190. (College Station, Texas, 2001).

18 Berndt, C., Bünz, S. & Mienert, J. Polygonal fault systems on the mid-Norwegian margin: a long-term source for fluid flow. *Geological Society, London, Special Publications* **216**, 283-290 (2003). https://doi.org/10.1144/gsl.sp.2003.216.01.18

19 Stuevold, L. M., Faerseth, R. B., Arnesen, L., Cartwright, J. & Möller, N. Polygonal faults in the Ormen Lange Field, Møre Basin, offshore Mid Norway. *Geological Society, London, Special Publications* **216**, 263-281 (2003). https://doi.org/10.1144/gsl.sp.2003.216.01.17

20 Shin, H., Santamarina, J. C. & Cartwright, J. A. Contraction-driven shear failure in compacting uncemented sediments. *Geology* **36**, 931 (2008). https://doi.org/10.1130/g24951a.1

21 Goulty, N. R. Geomechanics of polygonal fault systems: a review. *Petroleum Geoscience* **14**, 389-397 (2008). https://doi.org/10.1144/1354-079308-781

22 Henriet, J. P., de Batist, M., Vaerenbergh, W. & Verschuren, M. Seismic facies and clay tectonic features of the Ypresian clac in the southern North Sea. *Bulletin van de Belgische Vereniging voor Geologie* **97**, 457-472 (1988).

23 Verschuren, M. Outcrop evidence of polygonal faulting in Ypresian marine clays (Southern North Sea Basin) leads to a new synthesis. *Marine Geology* **413**, 85-98 (2019). https://doi.org/10.1016/j.margeo.2019.04.002

24 Mestdagh, T. *et al.* Report on the acquisition and processing of geophysical data for the detection and characterisation of clay tectonic features in the Princess Elisabeth Zone (Belgian Continental Shelf). (Flanders Marine Institute (VLIZ), Ostend, Belgium, 2024).

25 Mestdagh, T., Plets, R., Missiaen, T. & Pirlet, H. Report on the selection of study areas based on available geophysical datasets and literatures. (Flanders Marine Institute (VLIZ), Ostend, Belgium, 2023).

Appendix

Block A

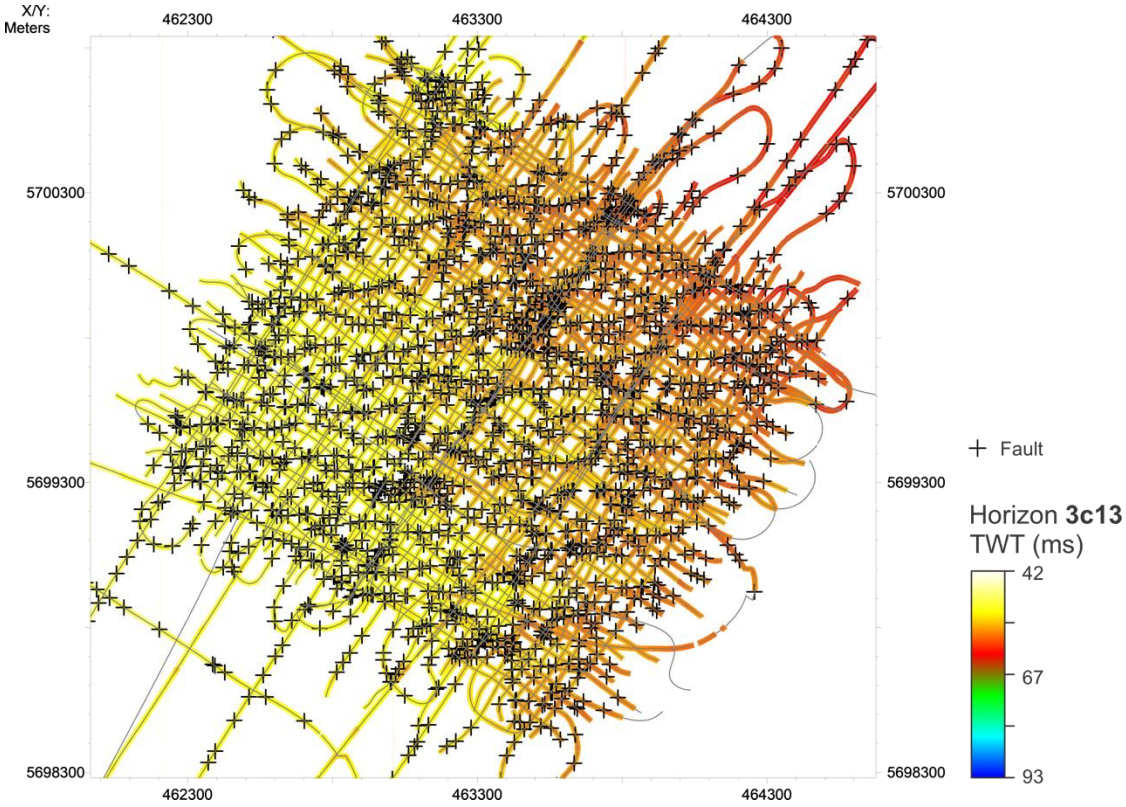

Figure A.1. Mapping of the key horizon (3c13) and faults in Block A (S&P Kingdom Suite)

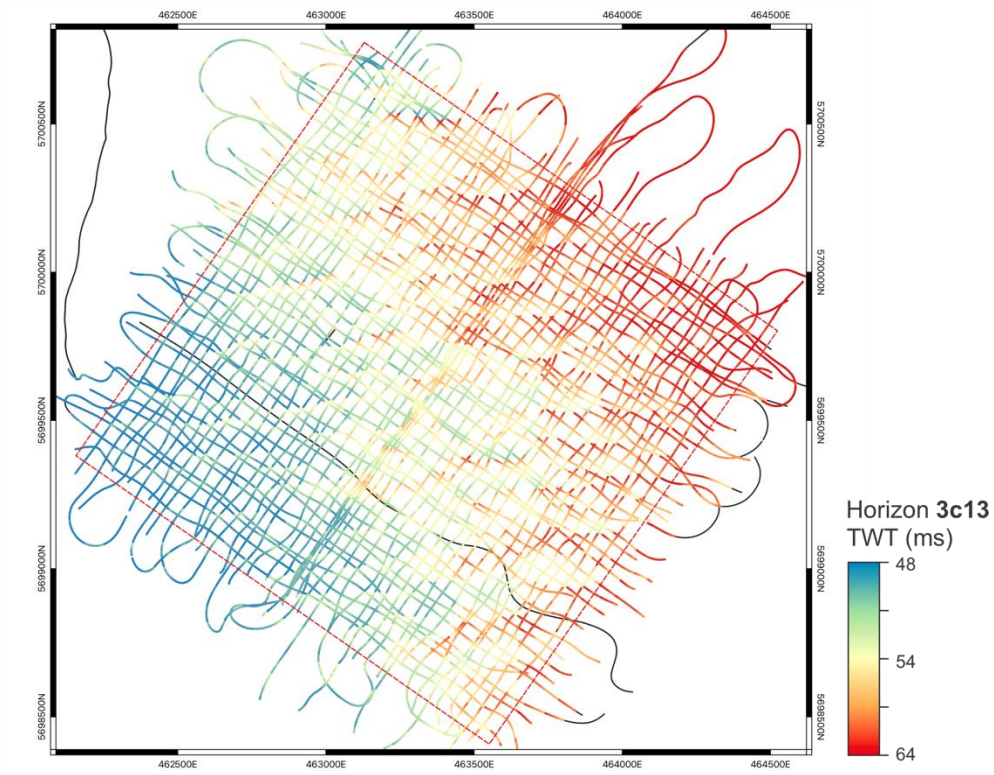

Figure A.2. Key horizon of Block A (QGIS)

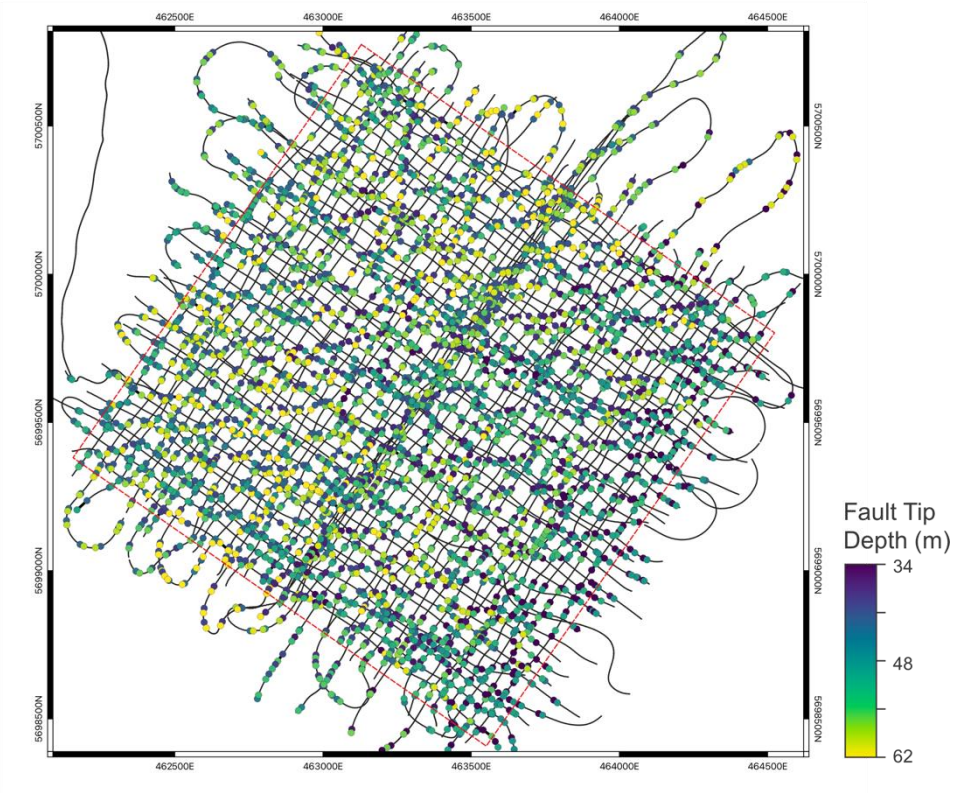

Figure A.3. Distribution of fault tip depths in Block A for fault correlation (QGIS)

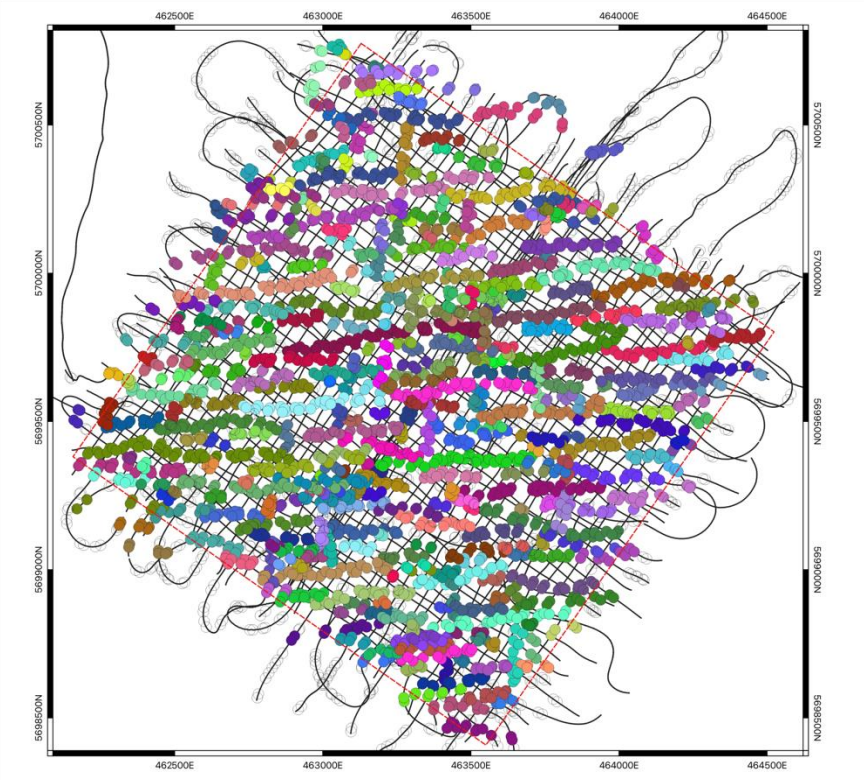

Figure A.4. Correlated faults in Block A for fault modelling (QGIS)

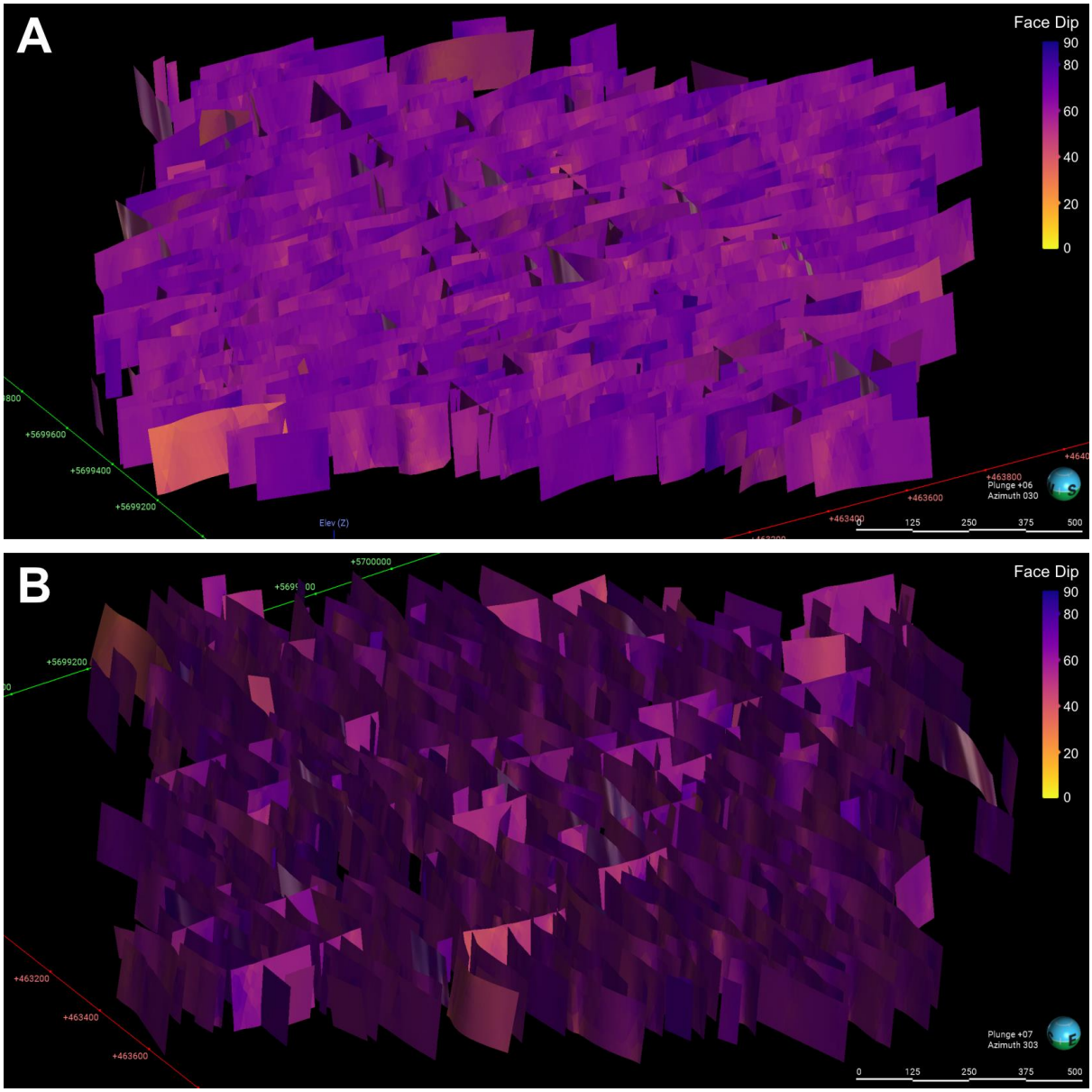

Figure A.5. 3D fault models of Block A in (A) northeast facing view and (B) northwest facing view (Leapfrog Geo)

Block B

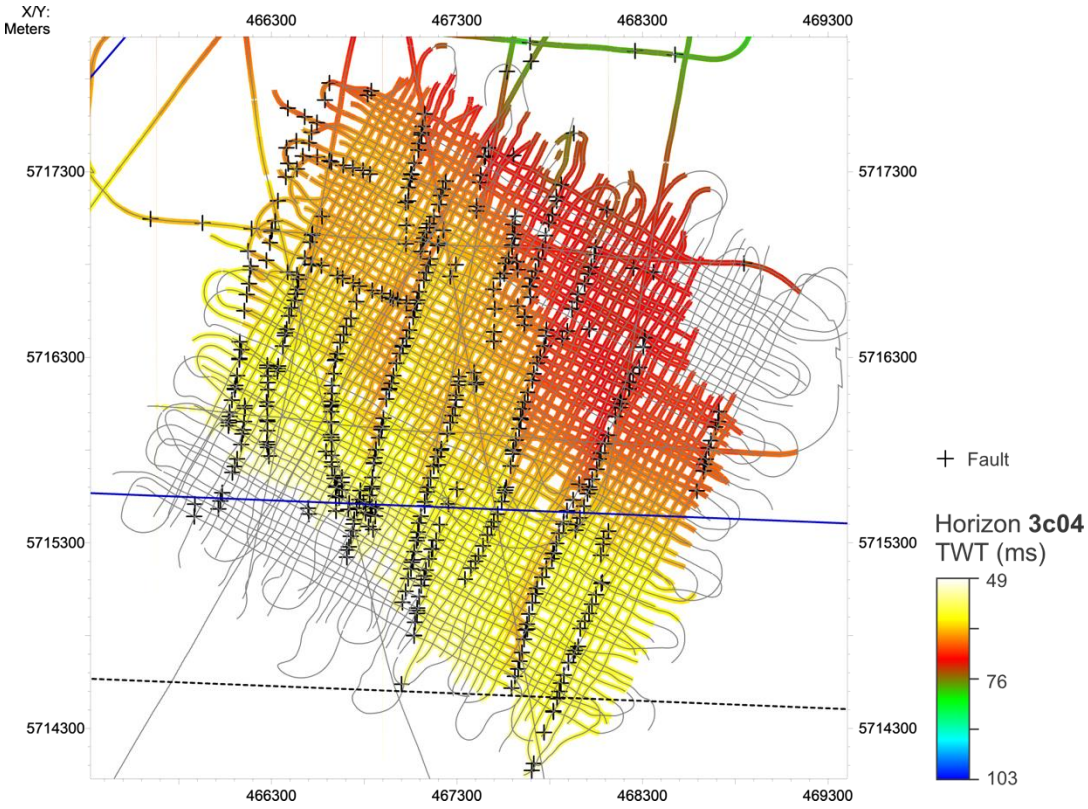

Figure A.6. Mapping of the key horizon (3c04) and faults in Block B (S&P Kingdom Suite)

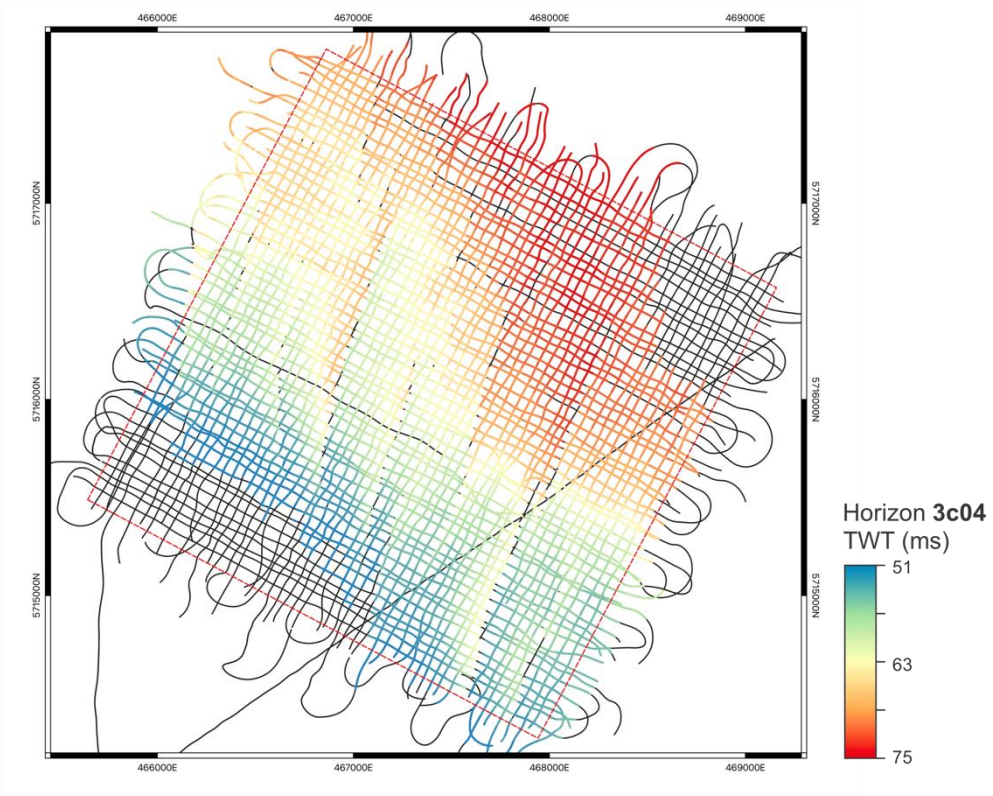

Figure A.7. Key horizon of Block B (QGIS)

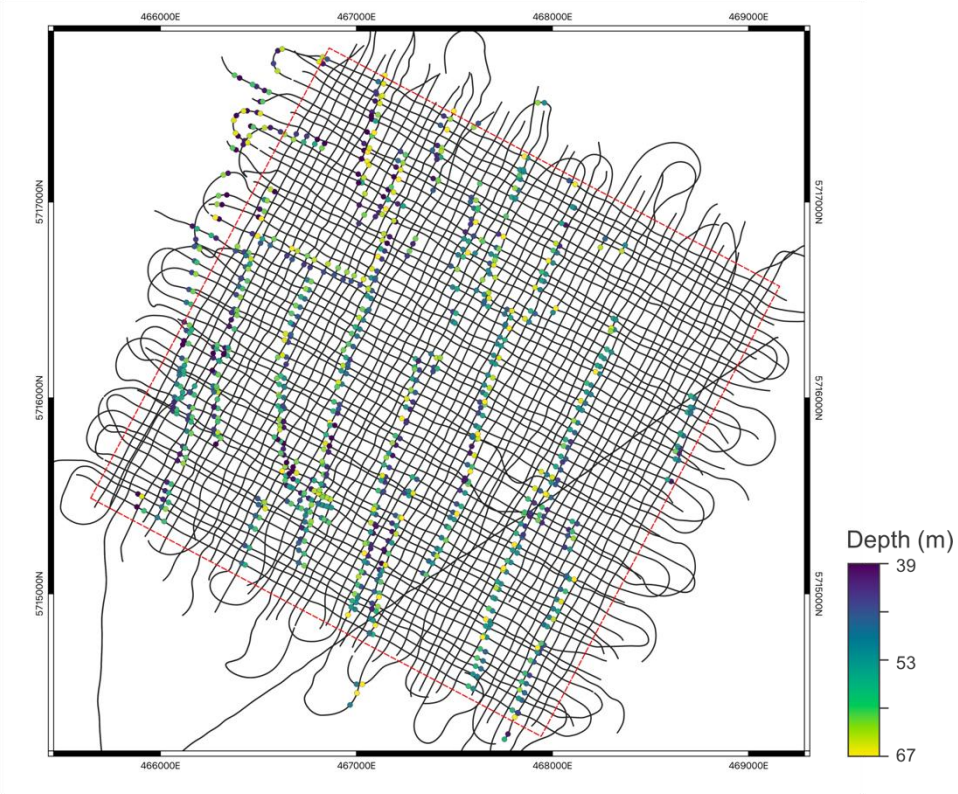

Figure A.8. Distribution of fault tip depths in Block B for fault correlation (QGIS)

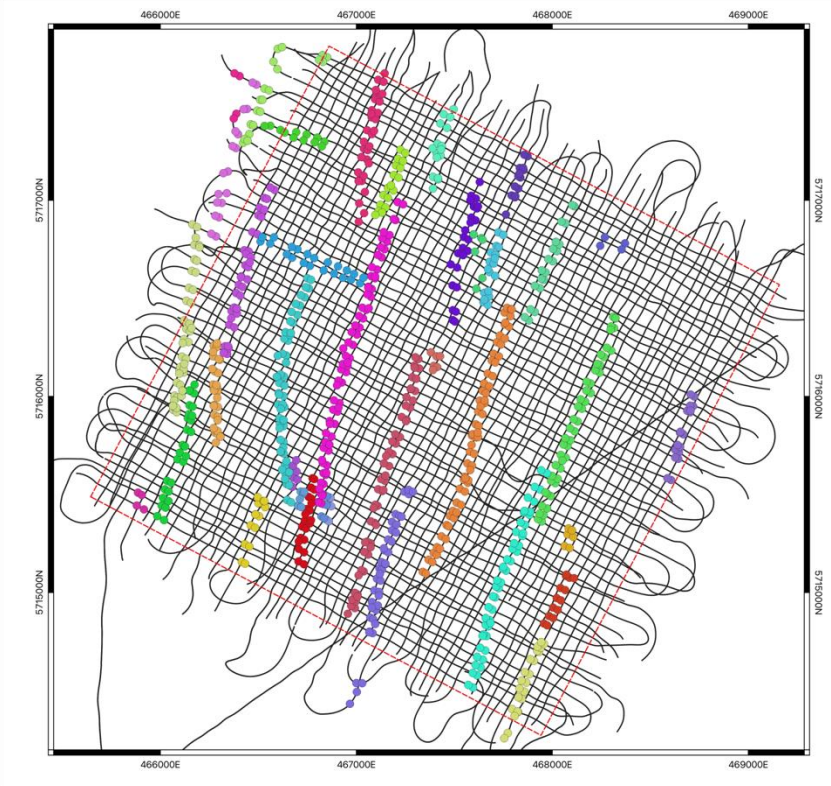

Figure A.9. Correlated faults in Block B for fault modelling (QGIS)

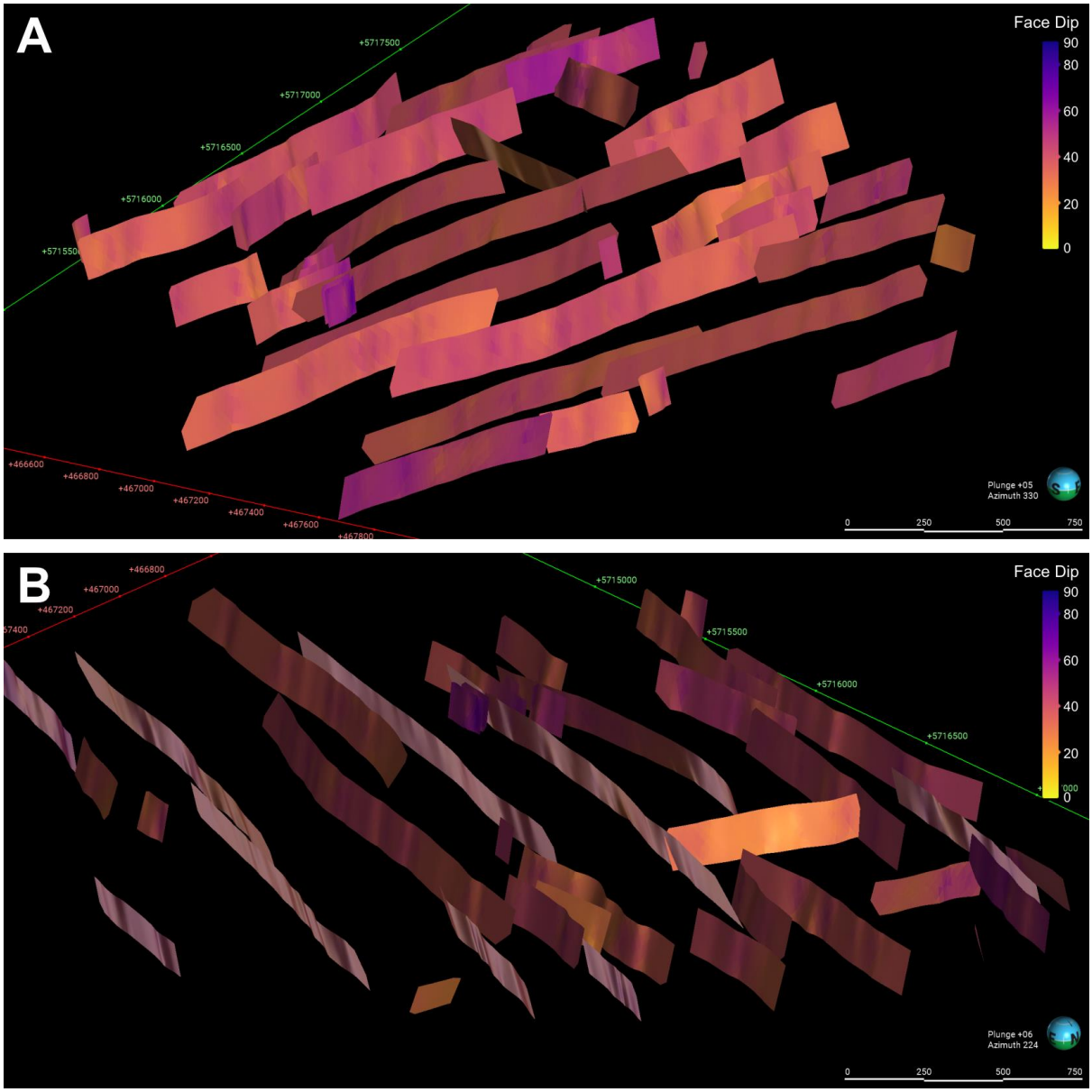

Figure A.10. 3D fault models of Block B in (A) northwest facing view and (B) southwest facing view (Leapfrog Geo)

Block C

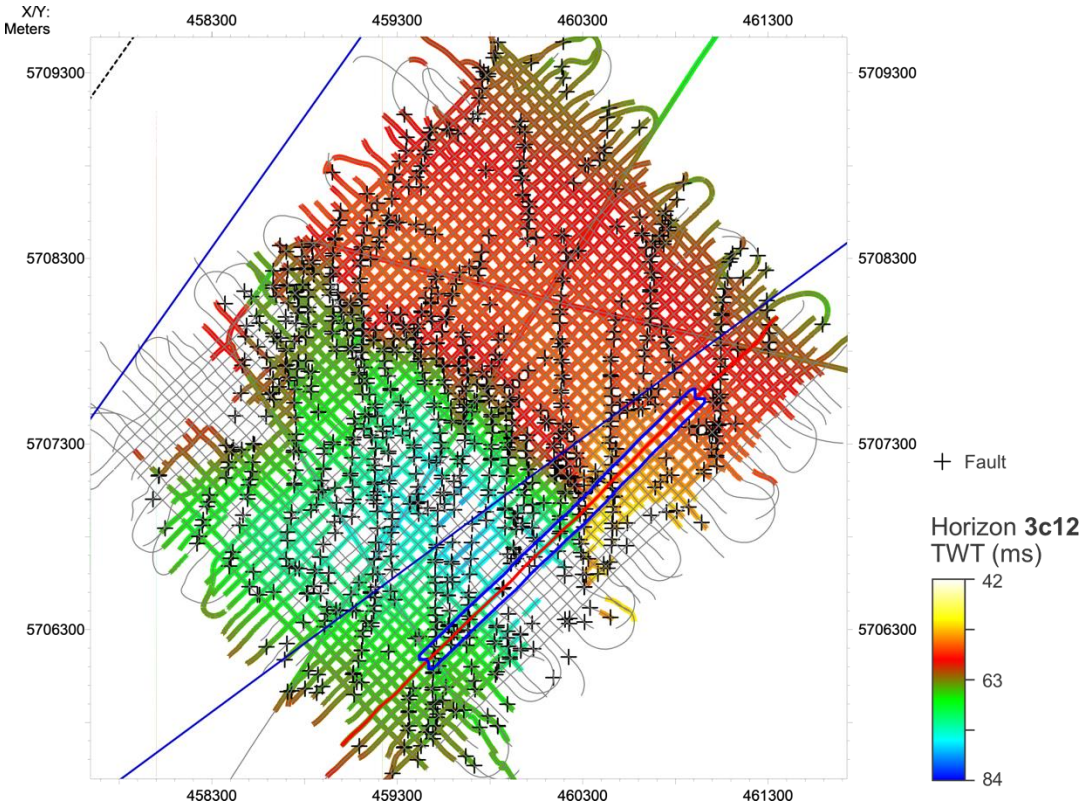

Figure A.11. Mapping of the key horizon (3c12) and faults in Block C (S&P Kingdom Suite)

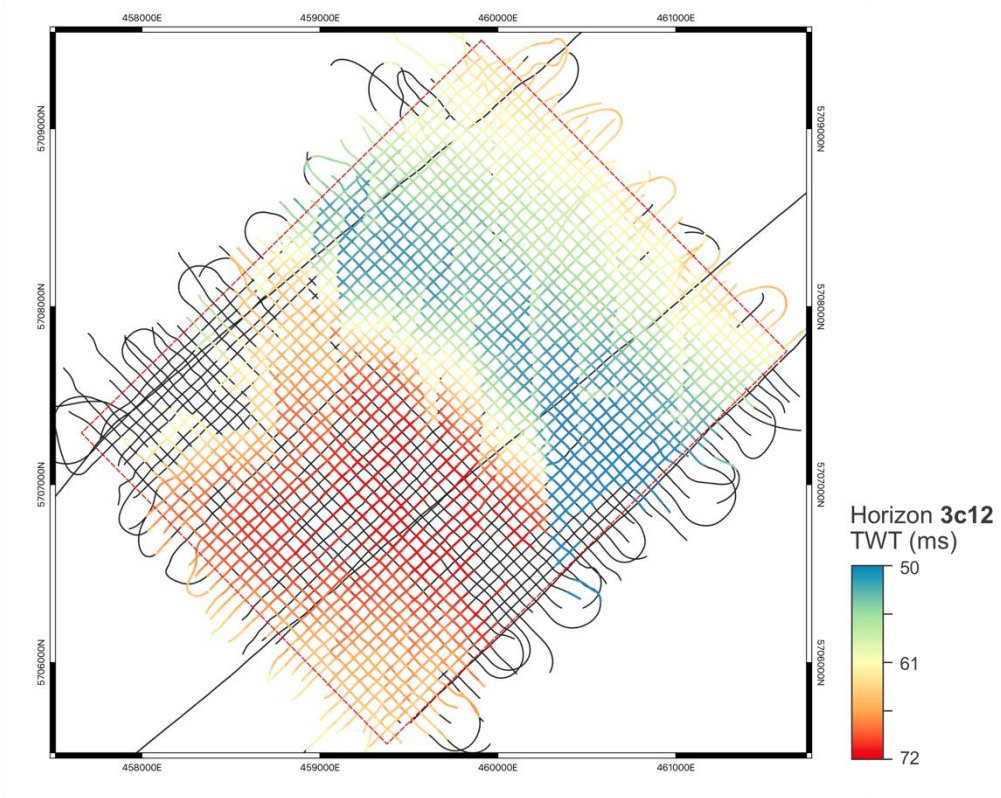

Figure A.12. Key horizon of Block C (QGIS)

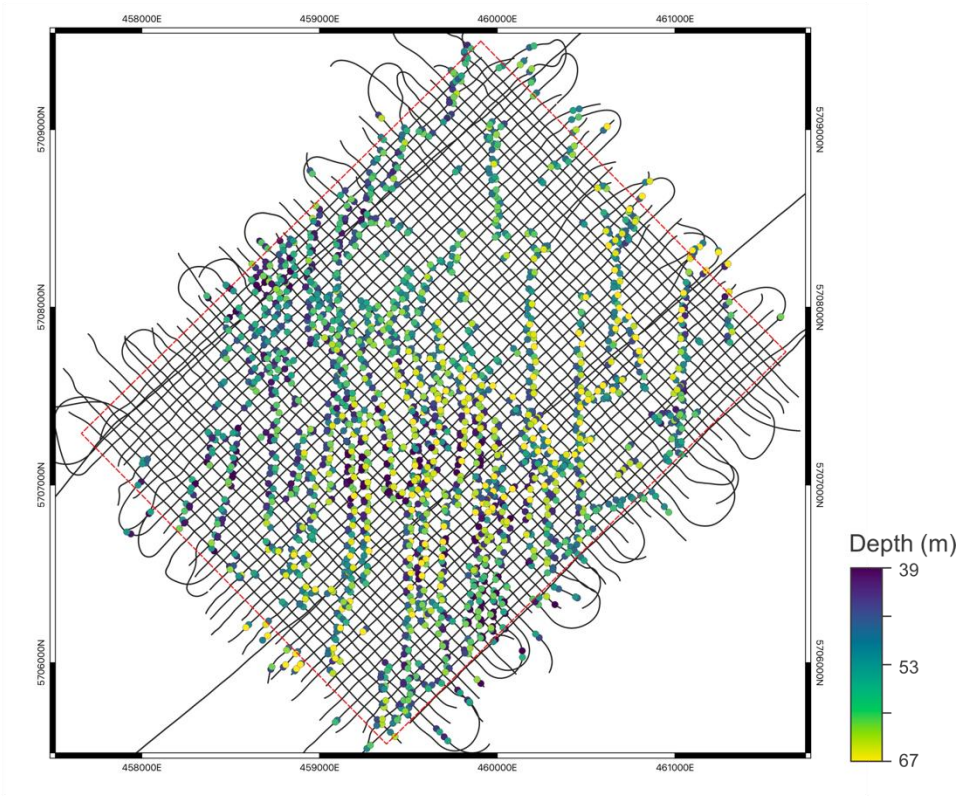

Figure A.13. Distribution of fault tip depths in Block C for fault correlation (QGIS)

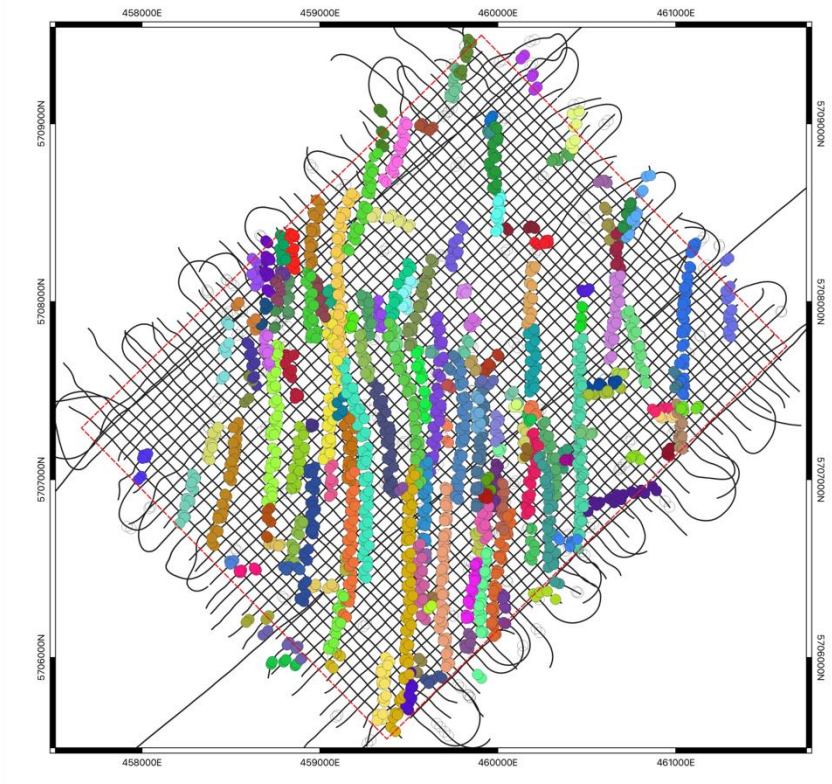

Figure A.14. Correlated faults in Block C for fault modelling (QGIS)

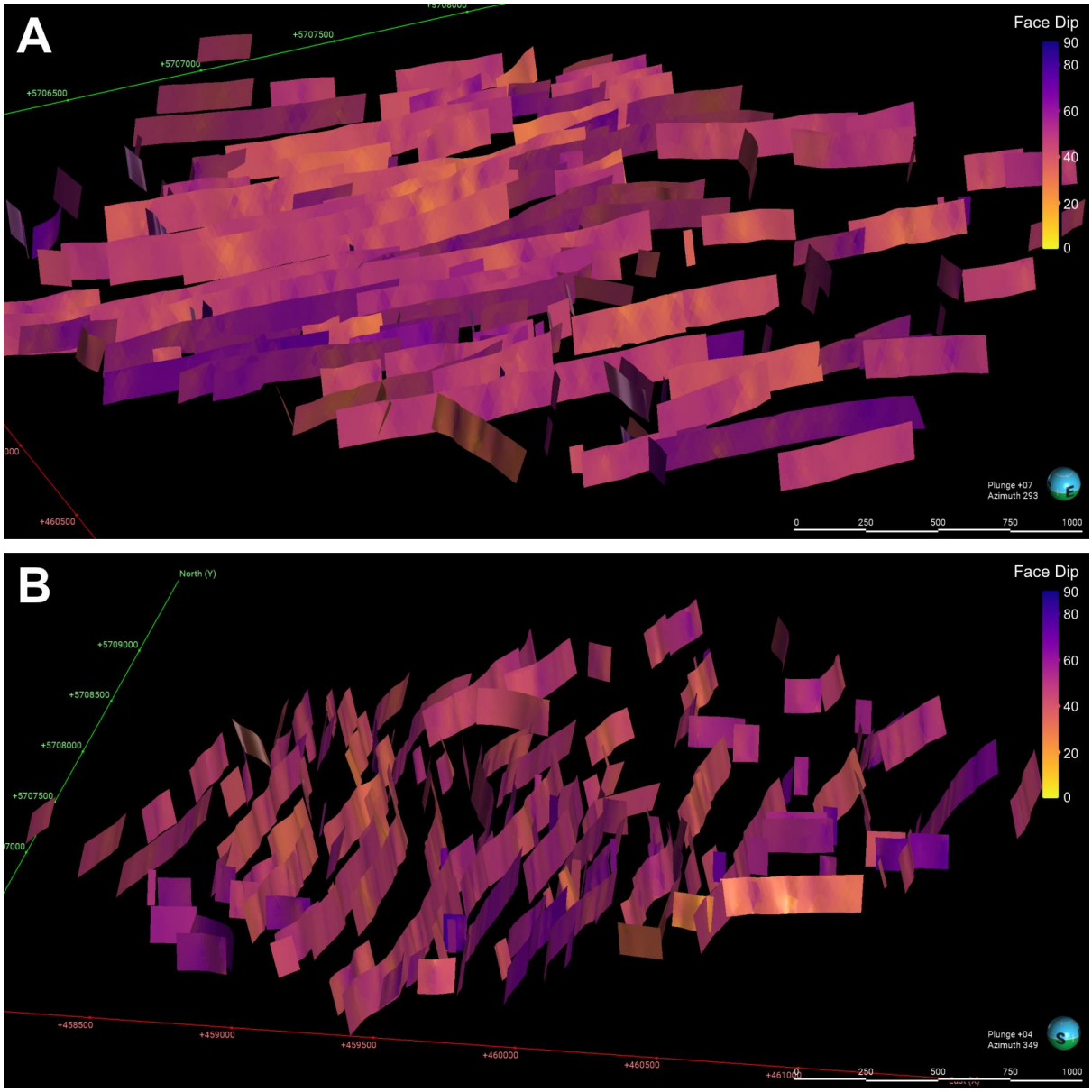

Figure A.15. 3D fault models of Block C in (A) west facing view and (B) north facing view (Leapfrog Geo)

Block D

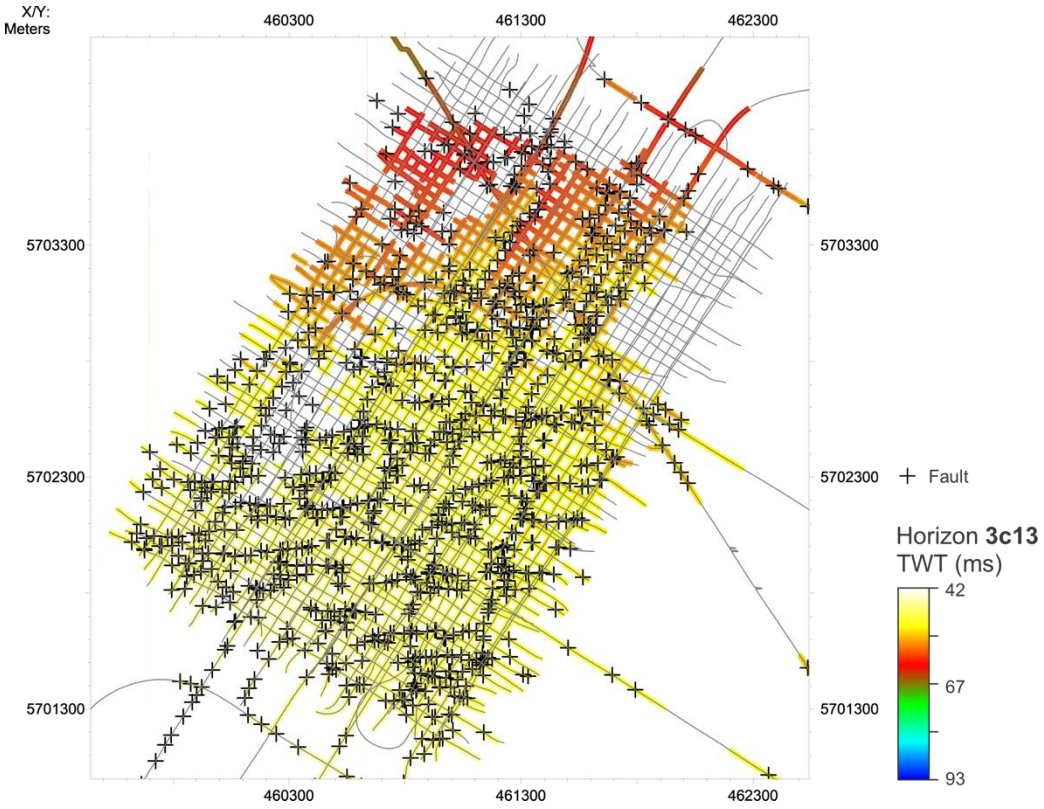

Figure A.16. Mapping of the key horizon (3c13) and faults in Block D (S&P Kingdom Suite)

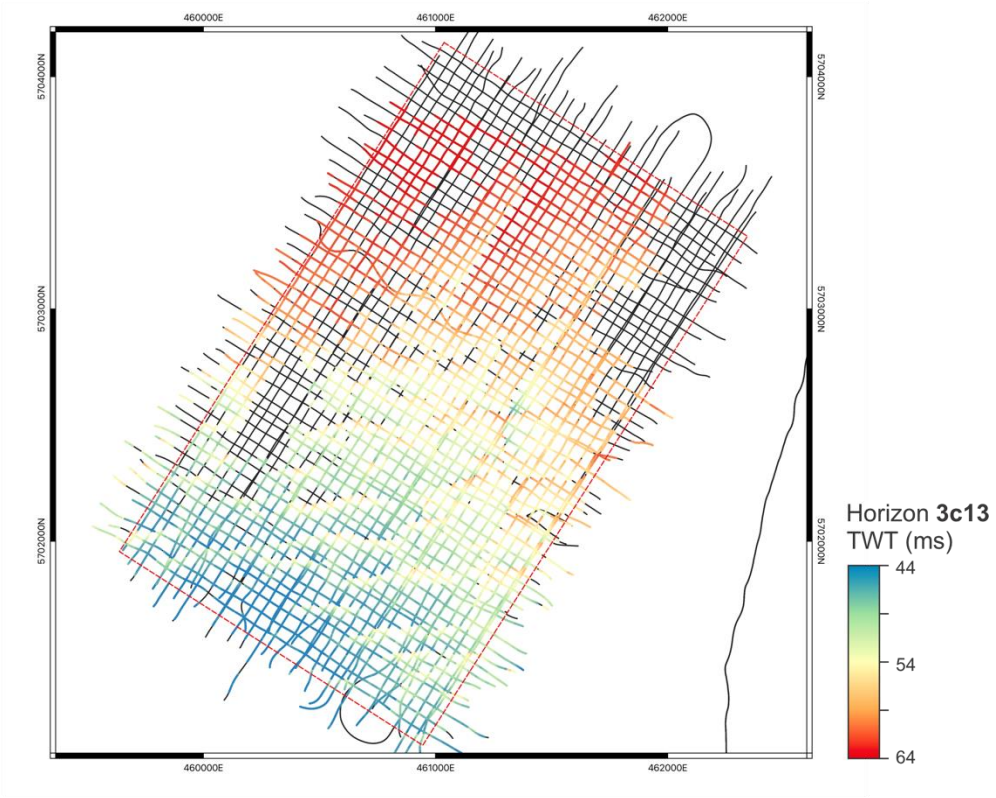

Figure A.17. Key horizon of Block D (QGIS)

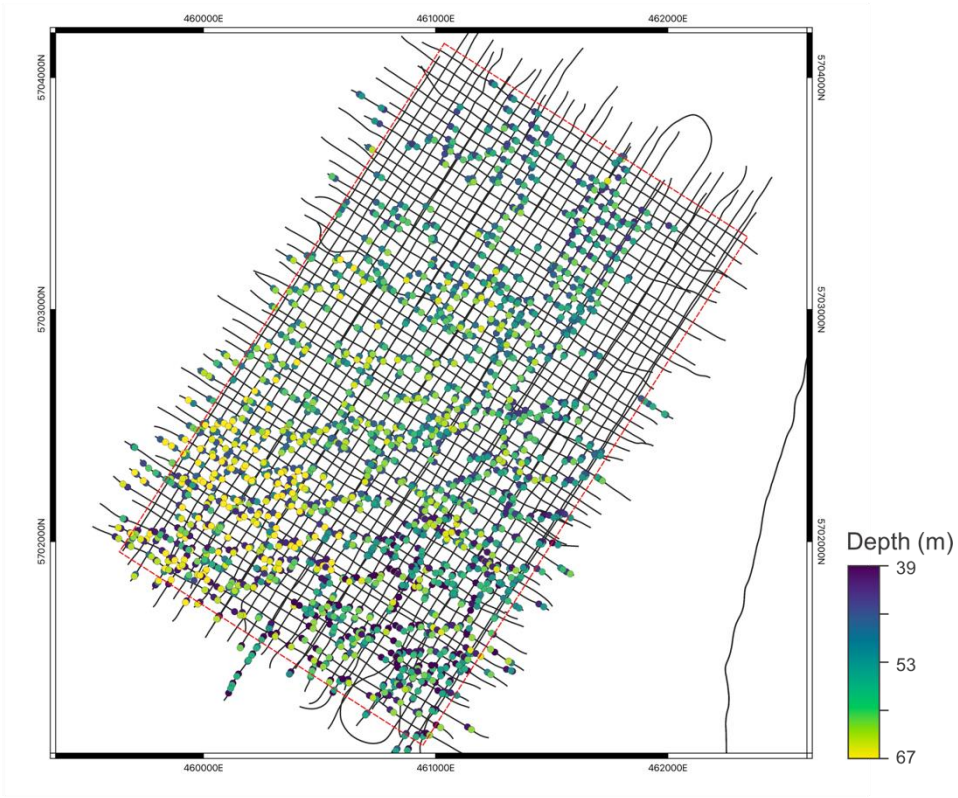

Figure A.18. Distribution of fault tip depths in Block D for fault correlation (QGIS)

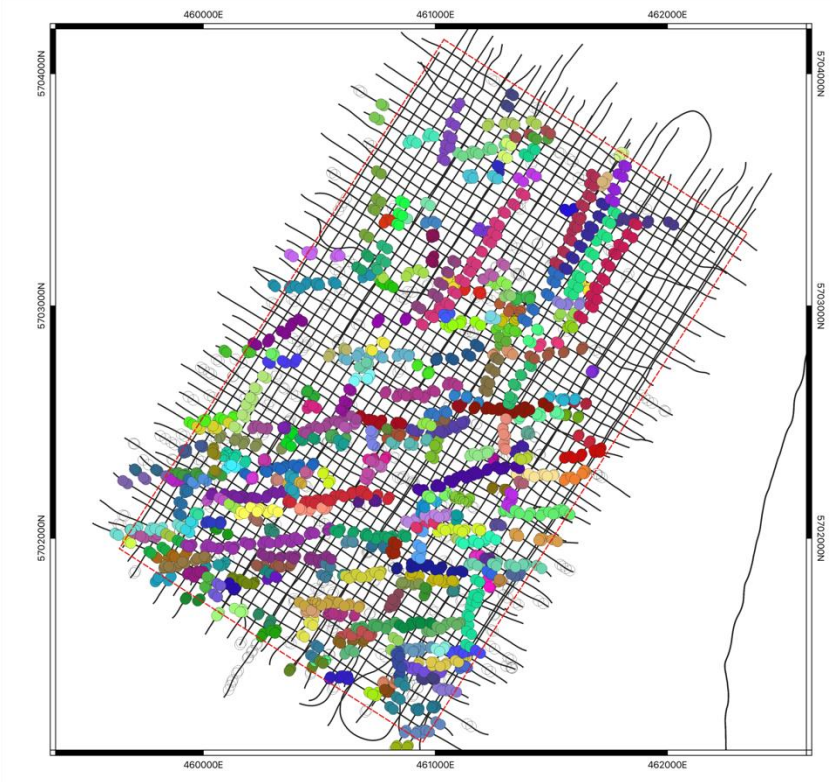

Figure A.19. Correlated faults in Block D for fault modelling (QGIS)

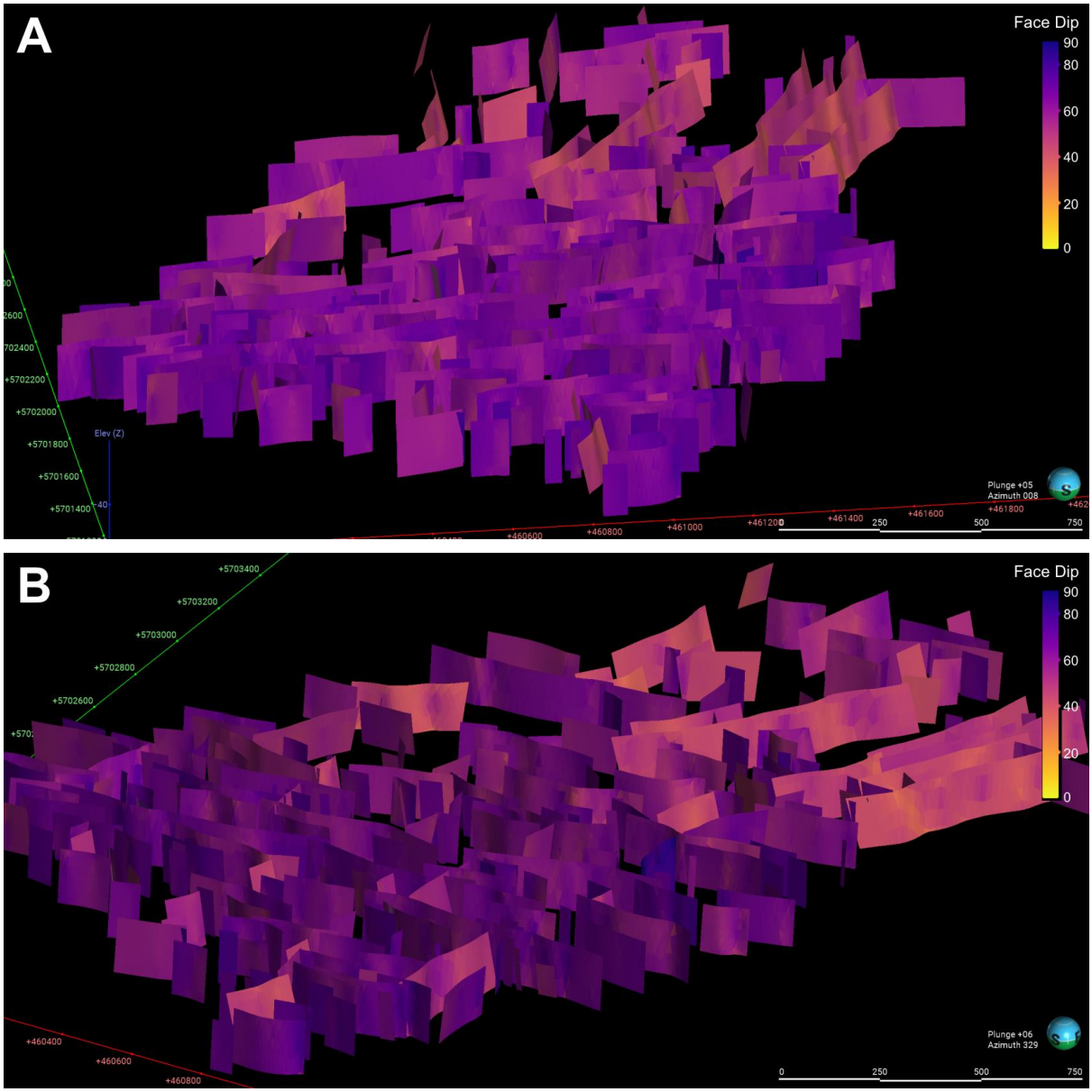

Figure A.20. 3D fault models of Block D in (A) north facing view and (B) northwest facing view (Leapfrog Geo)